Dynamics of Lipid Membrane Tubes

by

Sami Cameron Al-Izzi

Thesis

Submitted to the University of Warwick

& Sorbonne Université

for the degree of

Doctor of Philosophy

MathSys CDT & UMR168 Physico-Chimie Curie

September 2019

Contents

List of Figures

Acknowledgments

First and foremost I would like to thank my supervisors Matthew Turner and Pierre Sens for their guidance over the past 3 years and for being fantastic people to work with. I'm deeply grateful to have had them as supervisors. Thanks to George Rowlands for the many interesting discussions about non-linear dynamics, advice and encouragement, and coffee and biscuits. I would also like to thank Shigeyuki Komura for hosting me at Tokyo Metropolitan University for 6 weeks in winter 2019, I had a great time working in Tokyo and Chapter 4 of this thesis came out of this collaboration. This visit was supported by Tokyo Metropolitan University under the Graduate Short-term Inbound and Outbound Program. Thanks to Robert Gowers for helpful comments on the draft of this thesis. I would also like to thank Ana-Suncana Smith and Halim Kusumaatmaja for agreeing to act as rapporteurs/external examiners and Gareth Alexander and Jacques Prost for agreeing to act as examiners for Warwick and Sorbonne respectively.

I was lucky enough to live with awesome people throughout my time at Warwick; thank you Chris, Sophie, Cameron, Aurelija, Clare and Andrea for putting up with me as a housemate! Thanks to everyone in MathSys/Complexity and beyond who made my time here really special. In particular the occupants of D2.05; Ayman, Iliana, Roger, Joe, Ellen, Jack; the climbing/bouldering crew; Jon, Laura, Jim; and also Jason, Rob, Aditi, Michael, Susie, Edu, Paul and Emma; thanks for making my time at Warwick really memorable. To everyone in UMR168-PCC; you made my time in Paris truly amazing! Jean-Patrick, Mathieu, Niladri and Remy; thank you for making me feel a part of "Team Sens". Also thanks to Akifumi and all the Bio-Soft Matter Theory group at TMU for making my brief time in Tokyo

so much fun!

Finally, I would not be where I am now without the constant support of my family. They have always been there for me and have tolerated my overzealous enthusiasm for physics and maths for too many years. Mum, Dad, Hana: thank you.

Declarations

This thesis is submitted to the University of Warwick and Sorbonne Université in support of my application for the degree of Doctor of Philosophy. It has been composed by myself and has not been submitted in any previous application for any degree. Parts of the material in this thesis have been published as follows:

- Chapter 2 has been published as Hydro-osmotic Instabilities in Active Membrane Tubes - Sami C. Al-Izzi, George Rowlands, Pierre Sens & Matthew S. Turner - Phys. Rev. Lett. 120, 138102 (2018)

- Chapter 3 is currently under review as Shear-driven Instabilities in Membrane Tubes and Dyanmin-induced Scission - Sami C. Al-Izzi, Pierre Sens & Matthew S. Turner

- Chapter 4 is currently in preparation as Dynamics of Passive and Active Membrane Tubes - Sami C. Al-Izzi, Pierre Sens, Matthew S. Turner & Shigeyuki Komura

Abstract

Membrane tubes are structures ubiquitous in cells, and understanding their dynamics and morphology is of vital importance for cellular biophysics. This thesis will discuss several aspects of the dynamics of membrane tubes in situations where they are driven out of equilibrium by various biologically inspired processes. We analyse the inflation of membrane tubes and their subsequent instability due to ion pumps driving an osmotic pressure difference. This is inspired by the structure of an organelle called the contractile vacuole complex, and leads to a new instability with a much longer natural wavelength than a typical pearling instability. The stability of membrane tubes with a shear in the membrane flow is analysed and a novel helical instability which acts to amplify the fluctuations is found. We discuss the relevance of this instability in the process of dynamin-mediated tube scission. Finally we consider the dynamics and fluctuations of a membrane tube with active forces acting on it.

Abbreviations

$\mathbb{Z}$ - Set of integers $\mathbb{Z} = \{\ldots, -2, -1, 0, 1, 2, \ldots\}$

$\mathbb{R}^n$ - n-dimensional space of real numbers

$\mathcal{M}$ - Two dimensional differentiable manifold embedded in $\mathbb{R}^3$

$\mathcal{S}$ - Manifold denoting the neutral plane of a lipid bilayer

$\vec{X}$ - A vector living in $\mathbb{R}^3$

$\boldsymbol{x}$ - A vector field living in the tangent bundle to a two dimensional (2D) manifold embedded in $\mathbb{R}^3$

H - Mean curvature

K - Gaussian curvature

σ - Surface tension

κ - Splay modulus

$\bar{\kappa}$ - Saddle splay modulus

ΔP - Pressure jump or Laplace pressure across membrane

ATP - Adenosine triphosphate

ADP - Adenosine diphosphate

GTP - Guanosine triphosphate

GDP - Guanosine diphosphate

ER - Endoplasmic reticulum

CVC - Contractile vacuole complex

Chapter 1

Introduction

From the perspective of a physicist, biology is difficult. Living systems are driven far out of equilibrium by the energy consumed in the chemical reactions necessary to sustain life, meaning these systems are well beyond the paradigm of classical statistical physics which assumes equilibrium or close to equilibrium systems [Landau and Lifshitz, 1951; Onsager, 1931a,b]. Molecular specificity is also of vital importance in many biological systems, so coarse graining systems is incredibly challenging [Alon, 2019]. Further to this, biological systems are rarely specified simply in terms of their present form and function, but often depend on the system's entire evolutionary history.

Despite this physics has made significant contributions to biology in recent years, firstly from the transfer of experimental techniques, such as optical and magnetic tweezers [Ashkin, 1970; Crick and Hughes, 1950] and protein crystallography [Alberts et al., 2002], and secondly by the successful use of theoretical ideas from soft matter, statistical mechanics and information theory to analyse problems arising in biological systems [Bialek, 2018; Goldstein, 2018]. Such problems include chemical pattern formation [Turing, 1952; Hoyle, 2006], morphogenesis [Odell et al., 1981; Gross et al., 2017; Lecuit and Mahadevan, 2017; Goriely, 2017], the dynamics of DNA and other bio-polymers [Boal, 2002; Marenduzzo et al., 2006], dynamics and control in gene regulation [Alon, 2019; Petkova et al., 2019] and, of central importance to this thesis, the mechanics and dynamics of lipid membranes [Helfrich, 1973; Powers, 2010; Seifert, 1997; Safran, 1994; Lipowsky and Sackmann, 1995; Bassereau and Sens, 2018]. From a more abstract, and controversial, perspective there has even been the suggestion that evolution itself can be viewed as an emergent physical phenomenon [Goldenfeld and Woese, 2011].

The success of soft matter physics based approaches comes largely from the fact that both fields share similar energy scales (such that deformations can occur due to thermal fluctuations), length and time-scales, along with biological materials having similar mechanical properties to many substances found in equilibrium soft matter physics [Doi, 2013]. This thesis will make use of ideas from soft matter physics to understand the dynamics of lipid membrane tubes. These are structures found in a variety of contexts inside the cell, and can be formed by the exertion of a localised force on a flat membrane [Derényi et al., 2002]. We will examine a variety of situations designed to capture important features of different cellular processes, typically driven by energy consuming active processes.

1.1 A short history of mechanics in cell biology

Compared with classical physics and chemistry, the study of mechano-biology is a relatively recent one. The first major attempt to describe the form and morphogenesis of living organisms using mathematics and the laws of physics was made by D'Arcy Thompson in his book "On Growth and Form" published in 1917 (and a second edition in 1942) [Thompson, 1917]. Although many of the mechanisms proposed for different morphologies have since been proven wrong, the central idea that all organisms must obey the laws of physics is quite an attractive one (particularly in light of the development of modern genetic and cell biology and the difficulties relating genotype to phenotype [Lecuit and Mahadevan, 2017]). As Thompson put it:

> *Cell and tissue, shell and bone, leaf and flower, are so many portions of matter, and it is in obedience to the laws of physics that their particles have been moved, moulded and confirmed. They are no exception to the rule that God always geometrizes. Their problems of form are in the first instance mathematical problems, their problems of growth are essentially physical problems, and the morphologist is, ipso facto, a student of physical science.*

A particularly famous idea from Thompson comes from the final chapter called "Theory of Transformations or the comparison of related forms" which discusses how mathematical transformations can be used to compare seemingly distinct morphological aspects of animals, Fig. 1.1a. Although many of Thompson's conjectures about how this could be used to find relations between species have been proven false (a point which may seem obvious to a modern reader when viewed from the paradigm of evolution by natural selection), the chapter is almost solely respons-

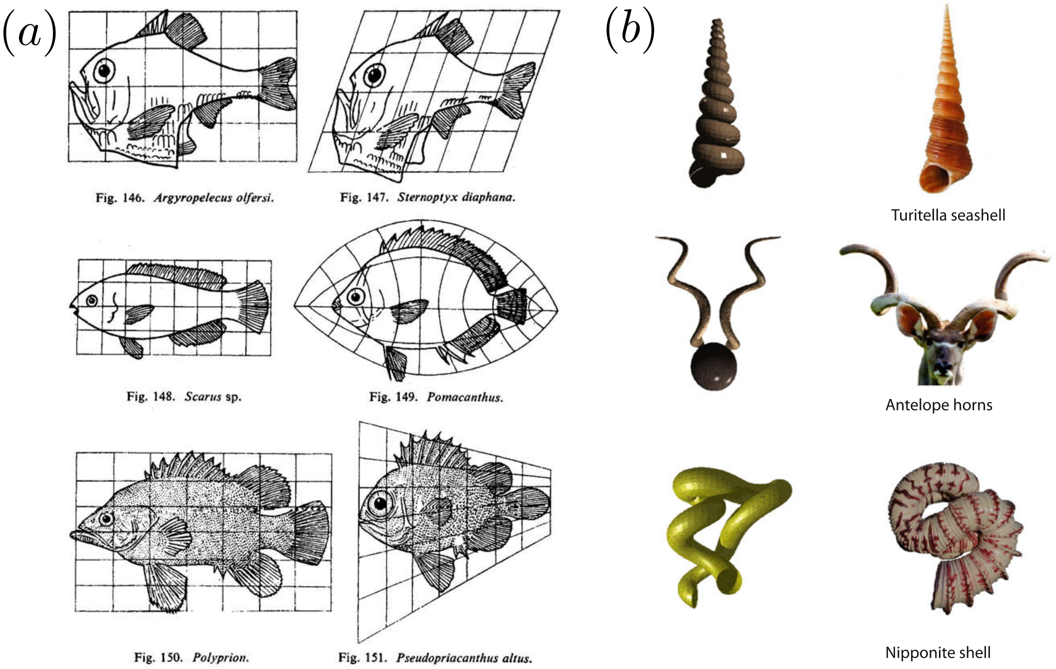

Figure 1.1: Mechanics and morphology in biology: (*a*) figure adapted from [Thompson, 1917], from the chapter on the “Theory of Transformations” between different forms, in this case various fish. (*b*) figure adapted from [Moulton and Goriely, 2014], showing different solutions to simple surface accumulative growth equations (starting from the same initial conditions but with a different “growth vector”) as compared to real biological forms.

ible for the foundation of the field of morphometrics and the development of pattern theory and statistical shape analysis [Lecuit and Mahadevan, 2017]. Moreover, more general geometric ideas similar to those used by Thompson have become more popular in recent years particularly when describing the growth of elastic sheets and rods in biological morphology [Moulton and Goriely, 2014; Goriely, 2017; Wong et al., 2017], Fig. 1.1b.

On the scale of cells, mechanical theories really began to take off in the 1970s with the pioneering work of Helfrich, Canham and Evans providing an elastic model of the cell membrane based on curvature energies [Helfrich, 1973; Canham, 1970; Evans, 1973a; Safran, 1994; Seifert, 1997]. The simplest form of this curvature energy is given by

$$\mathcal{F} = \int_{\mathcal{S}} \frac{\kappa}{2} \left(2H\right)^2 \mathrm{d}A_{\mathcal{S}} \tag{1.1}$$

where H is the mean curvature and κ the bending modulus of the lipid membrane. This energy could not only explain basic morphology, such as the bi-concave shape of a red blood cell [Canham, 1970; Seifert, 1997], but also more complex phenomena such as red blood cell flicker [Brochard and Lennon, 1975]. It will be this energy, and its dynamical variants that will be the main subject of this thesis.

A further development in theoretical mechanics in cell biology is that of the viscous dynamics of rods and filaments, particularly in the context of flagella and bacteria with solenoidal and super-coiled morphologies [Goldstein et al., 1998, 2000; Audoly and Pomeau, 2010; Boal, 2002]. There as also been a significant amount of research on the dynamics and thermodynamics of molecular motors and their interplay with the filaments that make up the cytoskeleton [Peskin et al., 1993; Jülicher and Prost, 1995; Mofrad and Kamm, 2006], whilst at a larger length-scale there is the paradigm for viewing the actomyosin cytoskeleton as an "active" liquid crystalline gel where detailed balance breaking stresses act along the direction of the nematic director [Kruse et al., 2005; Prost et al., 2015; Mofrad and Kamm, 2006].

Recently there has been a focus on active interfaces which couple the ideas of geometry and elasticity with active forces. These have been studied in the context of general formulations coupling chemical reactions to stresses and torques [Salbreux and Jülicher, 2017], more specific models for processes in morphogenesis [Morris and Rao, 2017; Haas and Goldstein, 2015; Höhn et al., 2015; Gross et al., 2017] and in terms of practical numerical methods for solving the full non-linear equations [Torres-Sánchez et al., 2019]. It is hoped that such models may provide insight into the detailed mechanisms behind force generation and shine a light on the interplay between signalling, geometry and mechanics in biology.

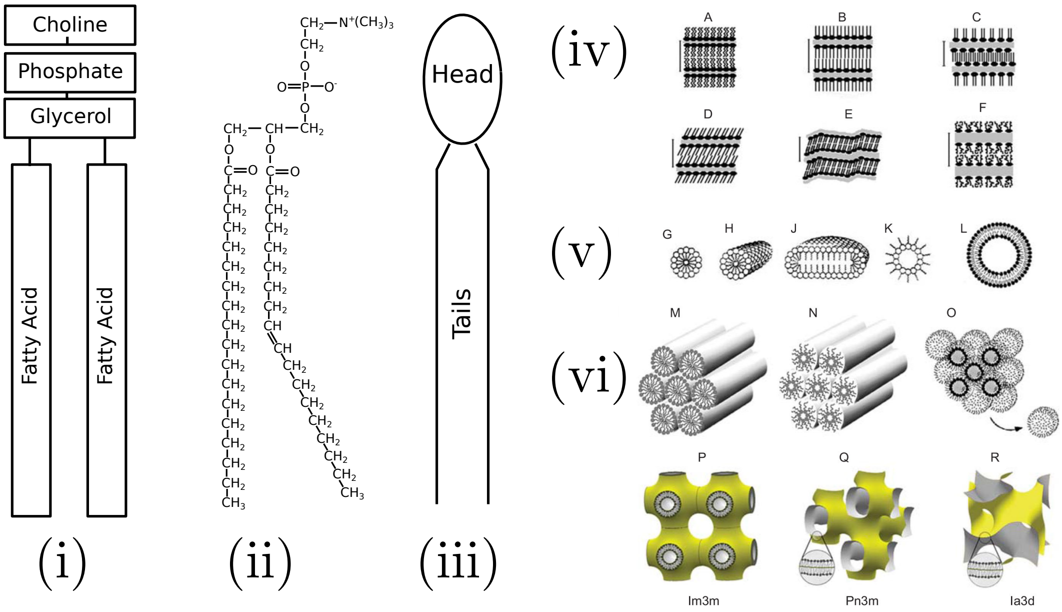

Figure 1.2: (i) Shows the general structure of a lipid molecule, (ii) Specific chemical structure of Phosphatidylcholine, (iii) Hydrophilic head and hydrophobic tail representation. Figure is a reproduction of a similar figure in [Alberts et al., 2002]. Figure taken from [Koynova and Tenchov, 2013] showing the vast phase space lipid membranes can occupy; (iv) Lamelar phases, (v) Micelles and Lipsomes & (vi) Non-lamellar liquid-crystalline phases.

1.2 Lipid molecules and their self-assembly

Living cells are complex heterogeneous structures which have evolved over millions of years to perform an enormous range of complex tasks. In order to segregate parts of the cell and compartmentalize different bio-chemical reactions, cells make use of organic molecules called lipids [Alberts et al., 2002; Phillips et al., 2010]. Lipids are thin organic molecules consisting of a head group that is hydrophilic and tail groups that are hydrophobic and hence such molecules are often called amphiphilic. By far the most common type of lipid molecules are Phospholipids consisting of a head group made of Choline, Phosphate and Glycerol, and two tail groups comprised of fatty acids (often one of the tails contains a double bond making it unsaturated), see Fig. 1.2 (ii). The amphiphilic property enables lipids to self assemble into a complex array of phases depending on temperature, chemical composition, density and the solvent they are in, see Fig. 1.2 (iv,v,vi) [Koynova and Tenchov, 2013]. The self assembly into these phases is driven by the minimisation of the thermodynamic free energy of the combined water-lipid system [Safran, 1994].

A particularly important phase for cells is that of the bilayer, which in water

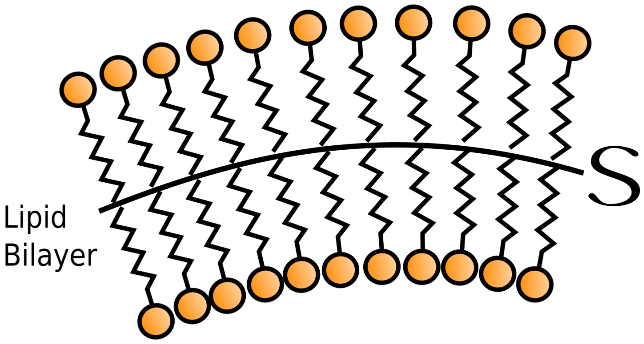

Figure 1.3: Schematic of a symmetric lipid bilayer in the fluid phase. $\mathcal{S}$ denotes the mid-plane of the bilayer.

consists of two layers of lipids with heads facing outwards and tails inwards, Fig. 1.2 (iv,v). Below a critical temperature, T_m, these bilayers can be found in the gel phase (L_β, Fig. 1.2 (v)D) and above this temperature in the fluid phase (L_α, Fig. 1.2 (iv) F, (v) L) [Kranenburg and Smit, 2005]. For most biologically relevant scenarios we will assume we are above the critical temperature and in the fluid phase [Simons and Vaz, 2004]. This phase has been shown to behave laterally as a two dimensional (2D) fluid at physiological temperatures allowing for the free diffusion of lipids [Phillips et al., 2010; Simons and Vaz, 2004].

These fluid bilayers are the membranes which bound most of the cell's internal compartments, called organelles. In eukaryotic cells most of the lipids are produced in a large membrane bound organelle called the endoplasmic reticulum (ER) [Alberts et al., 2002; Nixon-Abell et al., 2016]. The ER is made up of two main sections; the rough ER is a high surface area region consisting of many folds surrounding the nucleus and the peripheral ER is a dense tubular network which is spread throughout the cell [Nixon-Abell et al., 2016]. From the ER, membrane and proteins are fissioned off in vesicles and transported to the Golgi (an organelle consisting of layers of dynamic cisternae) which, through complex interactions, sorts the composition of membranes and proteins [Mironov and Pavelka, 2009]. From here vesicular transport takes the sorted membrane/proteins to various organelles, often called post-Golgi compartments [Alberts et al., 2002; Mullins, 2005]. These processes are illustrated in Fig. 1.4.

Of course real cell membranes are made up of many more components than just pure lipids (of which there are hundreds of species), most notably trans-membrane proteins which are vital to many cellular functions. The idea of the 2D fluid acting as a matrix in which proteins can freely diffuse was first formalised in the description of the "fluid mosaic" model of cell membranes [Singer and Nicolson, 1972; Alberts

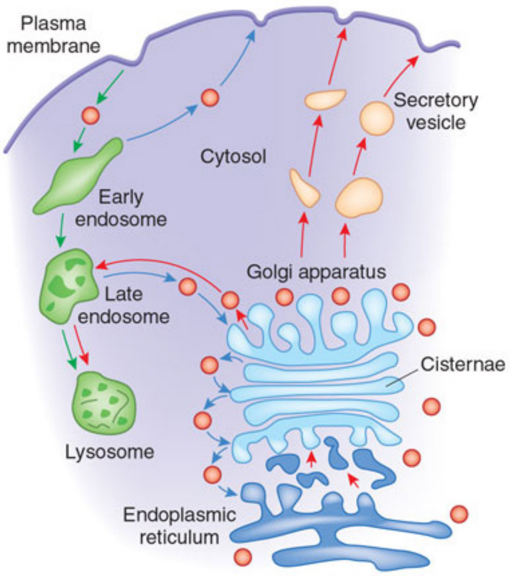

Figure 1.4: Schematic the endomembrane system in a eukaryotic cell (trans-Golgi network and endosomal network) showing membrane transport from the endoplasmic reticulum (ER) to the plasma membrane (and vice versa). Image from [Xu and Esko, 2009]

et al., 2002]. This is still a significant simplification of the real picture though. In reality proteins do not simply freely diffuse in the bilayer, but in many cases actively consume energy via the hydrolysis of Adenosine triphosphate or Guanosine triphosphate to undergo mechanical/conformational changes [Phillips et al., 2010]. This activity is believed to play a key role in cell membrane organisation, in particular forming domains needed in a huge variety of biological processes. This heterogeneous picture of the cell membrane developed mainly due to the advancement of single molecule tracking techniques, and such ideas were formalised in what is called the “pickets and fences” model where the cytoskeleton and trans-membrane proteins actively interplay with the membrane to organise domains [Kusumi et al., 2005].

In-vitro systems

In recent years many techniques have been developed to probe the physical properties of lipids in simplified biomimetic systems. Such systems have the benefit of containing only a few components, removing much of the added complexity of real biological membranes. These systems have allowed detailed measurements to be made of many specific physical properties of lipids and their associated trans-membrane protein complexes. These properties include, but are not limited to,

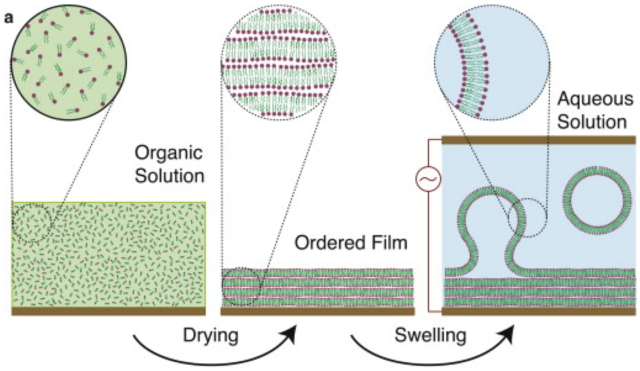

Figure 1.5: Formation of Giant Unilamellar Vesicles (GUV) by electro-formation, figure adapted from [Mertins et al., 2009].

diffusion of proteins [Quemeneur et al., 2014], membrane viscosity [Hormel et al., 2014], shape fluctuations [Girard et al., 2005] and phase separation/domain formation [Sackmann and Feder, 1995].

One such system which we will regularly refer to in this thesis is that of Giant Unilamellar Vesicles or GUVs. These are large bilayer vesicles often formed by electro-formation whose composition and size can be well controlled [Angelova et al., 1992; Mathivet et al., 1996]. A schematic of this process is shown in Fig. 1.5. Another *in-vitro* system often used to measure physical properties of lipids and trans-membrane proteins is is that of a supported lipid bilayer, which we will not discuss in detail here [Richter et al., 2006].

1.3 Geometry of surfaces

For the remainder of this thesis we will exploit the fact that lipid membranes self assemble into large-scale structures whose thickness, typically $4 - 5$nm, is much smaller than the lateral size of the membrane, typically $\sim 1\mu$m, and that the radii of curvature of the membrane are large with respect to the thickness [Phillips et al., 2010; Safran, 1994; Boal, 2002]. As such it will be convenient to treat the membrane as a smooth 2D surface which can deform due to the exertion of forces and torques, in more mathematical language we call this surface a manifold. In order to describe such a manifold one can make use of the extensive formalism that has been developed by mathematicians in the field of differential geometry. Differential geometry is a branch of mathematics that extends the notion of calculus in n-dimensional real space ($\mathbb{R}^n$) to more general curved spaces [Willmore, 2012; Frankel, 2011].

For simplicity we will restrict ourselves to discussing 2D surfaces embedded in $\mathbb{R}^3$ as this will be sufficient for the topics discussed in this thesis, for a detailed mathematical exposition of these ideas for n-dimensional surfaces see [Lee, 1997]. We will assume a basic knowledge of differential geometry and tensor calculus throughout (*e.g.* Einstein summation convention and how to raise and lower indices with the metric) but more advanced ideas such as exterior calculus will be introduced as needed.

Each point on the manifold, $p \in \mathcal{M}$, is labelled by a vector in the ambient space ($\mathbb{R}^3$) which we denote $\vec{X}_p \in \mathbb{R}^3$. Locally we can write $\vec{X}$ as a function of two coordinates which we denote x^i where $i = 1, 2$. We can use this to define some basis vectors to the tangent space, $\mathcal{T}(\mathcal{M})$ of the manifold

$$\vec{e}_i = \frac{\partial \vec{X}}{\partial x^i} \quad \text{for} \quad i = 1, 2 \tag{1.2}$$

from here we can define a bilinear form called the metric which enables us to ascribe a distance between points on the manifold. The metric is given by

$$\mathrm{d}S^2 = \langle \vec{e}_i, \vec{e}_j \rangle \mathrm{d}x^i \otimes \mathrm{d}x^j = g_{ij} \mathrm{d}x^i \otimes \mathrm{d}x^j \tag{1.3}$$

where $\langle \cdot, \cdot \rangle$ is the inner product in $\mathbb{R}^3$, $\mathrm{d}x^i$ are a basis of the cotangent space $\mathcal{T}^*(\mathcal{M})$ and $\otimes$ is a tensor product.

The unit normal vector to the surface is given by $\vec{n} = \frac{\vec{e}_1 \times \vec{e}_2}{|\vec{e}_1 \times \vec{e}_2|}$. The way the normal changes along a particular direction on the manifold gives a measure of the extrinsic curvature and can be quantified in the bilinear form given by

$$b = \langle \vec{n}, \partial_j \vec{e}_i \rangle \mathrm{d}x^i \otimes \mathrm{d}x^j = b_{ij} \mathrm{d}x^i \otimes \mathrm{d}x^j \tag{1.4}$$

which is often called the second fundamental form. Because b is a self adjoint operator, we can diagonalise it along the two axes of principal normal curvature and raise one index with the metric to give

$$[b]_i{}^j = \begin{pmatrix} \frac{1}{R_1} & 0 \\ 0 & \frac{1}{R_2} \end{pmatrix} \tag{1.5}$$

where R_1 and R_2 are the principal radii of curvature (and eigenvalues of b) [Frankel, 2011].

The trace and determinant of b are given by the sum and product of these eigenvalues and define the mean curvature, H, and Gaussian curvature, K, in the

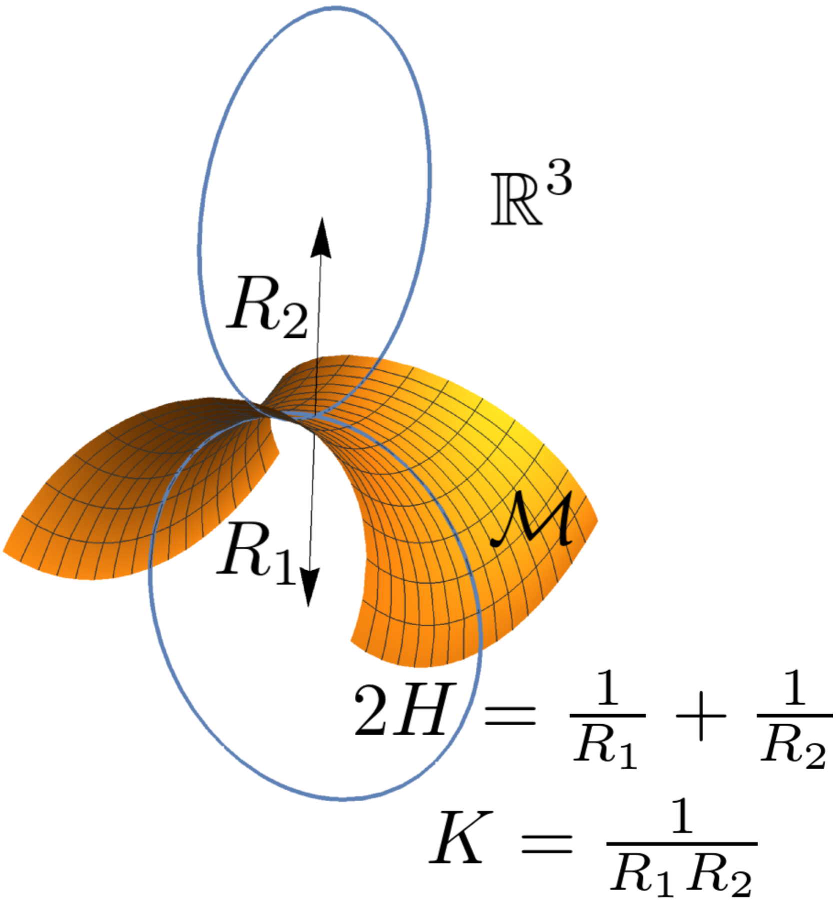

Figure 1.6: Schematic of principal radii of curvature, R_1 and R_2, on a 2D manifold $\mathcal{M}$ embedded in $\mathbb{R}^3$. The expressions for mean curvature, H, and Gaussian curvature, K, are also given.

following way

$$\begin{aligned} 2H &= \operatorname{tr}(b) = b_i{}^i = \frac{1}{R_1} + \frac{1}{R_2} \\ K &= \det b = \det b_i{}^j = \frac{1}{R_1 R_2}. \end{aligned} \tag{1.6}$$

A schematic of these curvatures is shown in Fig. 1.6.

The mean curvature is a purely extrinsic quantity, in that it describes how the 2D surface curves in $\mathbb{R}^3$. The Gaussian curvature, perhaps surprisingly, is purely intrinsic, in that it can be completely specified by just the metric and its derivatives (specifically the Riemann curvature tensor, R_{ijkl}, by the equation $K = R^{12}{}_{12}$). The relationship between intrinsic and extrinsic curvature is summarised by a set of equations called the Gauss-Codazzi-Mainardi equations which are a major result from differential geometry [Frankel, 2011] and have found applications recently in soft matter physics in the metric formulation of elasticity theory [Efrati et al., 2013].

1.4 The Helfrich-Canham energy

For a thin elastic medium there are two contributions to the elastic energy of the material; stretching and bending [Landau et al., 1986]. Since the compressional modulus for lipid bilayers is very large it is sufficient to consider the mechanics purely in terms of bending energy [Boal, 2002].

One way to derive the bending energy of a fluid membrane would be to do a formal thin film expansion of the 3D free energy, however the correct functional form can be inferred from simple arguments which we will describe here. This form of the free energy is an expansion in curvature to lowest order and was first proposed by [Helfrich, 1973; Canham, 1970; Evans, 1973b] in order to explain the shapes of red blood cells and artificial vesicles.

We know that the bending energy should depend on the curvature of the membrane, so must couple to the second fundamental form b, and should also be independent of local coordinate parameterizations. This means it should only depend on the trace and determinant of b, *i.e.* the mean and Gaussian curvature, H and K. If the bilayer is symmetric the energy should be symmetric on sending the normal $\vec{n} \to -\vec{n}$ so it can only depend on H^2 not H. This leads us to write the following energy for the membrane

$$\mathcal{F} = \int_{\mathcal{S}} \left[\frac{\kappa}{2} (2H)^2 + \bar{\kappa} K \right] \mathrm{d}A_{\mathcal{S}} \tag{1.7}$$

where κ and $\bar{\kappa}$ are the splay and saddle-splay moduli respectively. This can be generalised to include an asymmetry between the leaflets of the bilayer by introducing some spontaneous curvature C_0

$$\mathcal{F} = \int_{\mathcal{S}} \left[\frac{\kappa}{2} (2H - C_0)^2 + \bar{\kappa} K \right] \mathrm{d}A_{\mathcal{S}}. \tag{1.8}$$

This spontaneous curvature allows for energy minimising configurations which have some extrinsic curvature, *e.g.* due to differences in lipid species between the bilayers or the presence of proteins coating the membrane [Helfrich, 1973; Seifert, 1997]. We will refer to this energy as the Helfrich-Canham energy (or sometimes just Helfrich for conciseness).

Other contributions to the energy can also be considered, for example surface tension, σ and, if the membrane is closed, a Laplace pressure across the membrane,

ΔP. Including both of these contributions, the full free energy reads

$$\mathcal{F} = \int_{\mathcal{S}} \left[\frac{\kappa}{2} \left(2H - C_0\right)^2 + \bar{\kappa} K + \sigma \right] \mathrm{d}A_{\mathcal{S}} - \int \Delta P \mathrm{d}V \tag{1.9}$$

where $\mathcal{S} = \partial V$.

We can make use of a theorem from differential geometry, called the Gauss-Bonnet theorem, to simplify the energy further in some cases [Frankel, 2011]. The Gauss-Bonnet theorem states that for a 2D differentiable manifold $\mathcal{M}$ with boundary $\partial\mathcal{M}$

$$\int_{\mathcal{M}} K \mathrm{d}A = 2\pi\chi\left(\mathcal{M}\right) - \int_{\partial\mathcal{M}} k_g \mathrm{d}s \tag{1.10}$$

where $\chi\left(\mathcal{M}\right)$ is the Euler characteristic of the manifold and k_g is the geodesic curvature at the boundary. This result is surprising as it states that, for a closed manifold, the integral of the Gaussian curvature over the manifold is a constant that only depends on topology. This means that for cell membranes the saddle-splay modulus only enters the energy at the boundary, and that if we consider a closed membrane or membranes of infinite extent then we can neglect the contribution of Gaussian curvature to the free energy (as long as we have no changes in topology).

The Helfrich-Canham energy is closely related to the Willmore functional, $W[\mathcal{M}] = \int_{\mathcal{M}} H^2 \mathrm{d}A_{\mathcal{M}}$, which is of significant interest in pure differential geometry [Willmore, 1965]. There is a significant body of work on studying the properties of this functional with the related Willmore conjecture (the integral of the mean curvature squared of a torus immersed in $\mathbb{R}^3$ is at least $2\pi^2$) being proved recently [Marques and Neves, 2014].

1.4.1 Some simple minimisers

To gain help gain an understanding of the Helfrich Energy we will consider some simple geometrically constrained minimisers (the simplest example of which is a flat membrane).

The first non-trivial surface we will consider is that of a sphere of radius R. The free energy for this is given by

$$\mathcal{F}_{\text{sphere}} = 2\pi\kappa \left(\frac{2}{R} - C_0\right)^2 R^2 + 4\pi\sigma R^2 - \frac{4}{3}\pi\Delta P R^3 \tag{1.11}$$

which when minimised for variations in R gives the following relation

$$\frac{\kappa C_0^2 + 2\sigma}{R} = \Delta P + \frac{2\kappa C_0}{R^2} \tag{1.12}$$

which reduces to

$$\Delta P = \frac{2\sigma}{R} \tag{1.13}$$

when $C_0 = 0$, which is just the Laplace law for a spherical soap film. This tells us something quite remarkable, the bending energy of the membrane does not give any contribution to the optimal radius of a sphere. The radius here is just set by the length-scale given by $\frac{\sigma}{\Delta P}$, the only length-scale in the Helfrich Energy which does not involve the bending rigidity, κ. This result is an illustration of the conformal invariance of the Willmore functional [Seifert, 1997].

The second case we will consider, and which is highly relevant for the rest of this thesis, is that of a tube of radius, R, and length, L. The free energy is given by

$$\mathcal{F}_{\text{tube}} = 2\pi RL \left[\frac{\kappa}{2} \left(\frac{1}{R} - C_0 \right)^2 + \sigma \right] - \pi R^2 L \Delta P. \tag{1.14}$$

Minimising with respect to variations in R leads to the relation

$$-\frac{\kappa}{2R^2} + \frac{\kappa C_0^2}{2} + \sigma - \Delta P R = 0 \tag{1.15}$$

which reduces to

$$R = \sqrt{\frac{\kappa}{2\sigma}} \tag{1.16}$$

when $C_0 = 0$ and $\Delta P = 0$. This means that the natural size of a tube is set by the natural length-scale of the membrane $\epsilon = \sqrt{\frac{\kappa}{\sigma}}$. ϵ is the scale over which deformations persist in a close to flat membrane. This scale is set due to the balance between forces from the bending energy wanting to expand the radius of the tube and those from surface tension which attempt to minimise the surface area of the membrane.

1.4.2 Shape equation for a general surface

In the previous section we made use of geometric simplifications to gain some intuition about the forces which govern membrane shape. Here we consider the more general problem of the shape equation for an arbitrary surface. The partial differential equation whose solutions describe the minimisers of the Helfrich energy can be found by setting the first variation of the energy with respect to perturbations in the shape to zero. To derive this rigorously, one must make use of some rather

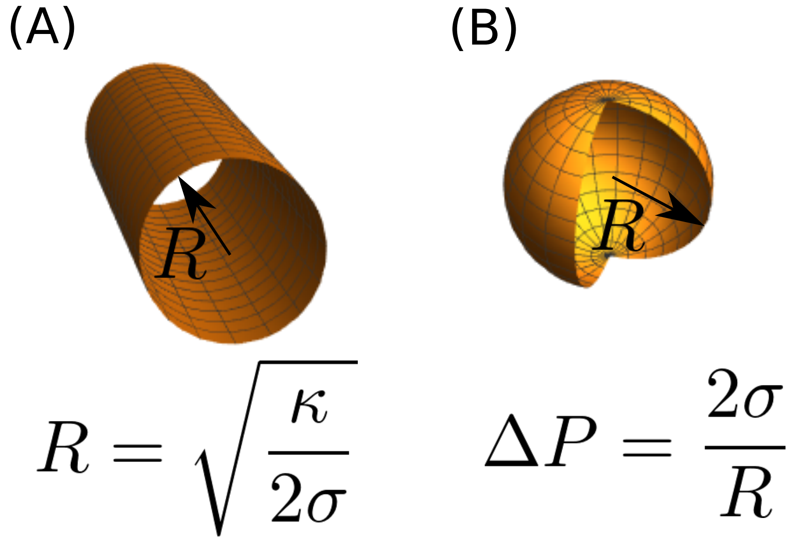

Figure 1.7: Simple surfaces that minimise the Helfrich energy, (A) a tube of radius $R = \sqrt{\frac{\kappa}{2\sigma}}$ (with no pressure jump or spontaneous curvature) and (B) a sphere of radius $R = \frac{2\sigma}{\Delta P}$ (with no spontaneous curvature).

messy differential geometry to account for the variations in the metric *etc.*. For simplicity we will only state the results here, but details of the full calculation can be found in Ref. [Zhong-Can and Helfrich, 1989]. For a rigorous pure mathematics derivation see Ref. [Simons, 1968].

The full shape equation for a membrane which minimises the Helfrich energy is given by

$$\kappa\left[2\Delta_{\mathrm{LB}}H - (4H + C_0)\left(H^2 - K - \frac{C_0}{2}H\right)\right] + 2H\sigma = \Delta P \tag{1.17}$$

where $\Delta_{\mathrm{LB}} = -\frac{1}{\sqrt{|g|}}\partial_i\left(\sqrt{|g|}g^{ij}\partial_j(\cdot)\right)$ is the Laplace-Beltrami operator for a scalar field on the manifold (defined with the same sign convention as in Ref. [Arroyo and DeSimone, 2009]). This is a 4^{th}-order non-linear PDE in the “height” of the membrane and in general there are no analytical solutions to the full equation, except in some simplified cases, for example [Rautu, 2018] and references therein.

Full solutions to the general problem are usually found via either gradient descent methods, *e.g.* Surface Evolver [Brakke, 1992], or using more sophisticated finite element methods to solve the shape equation via Willmore flow [Elliott and Stinner, 2010; Barrett et al., 2016]. We will not present a full account of these methods here as they will not be used in this thesis.

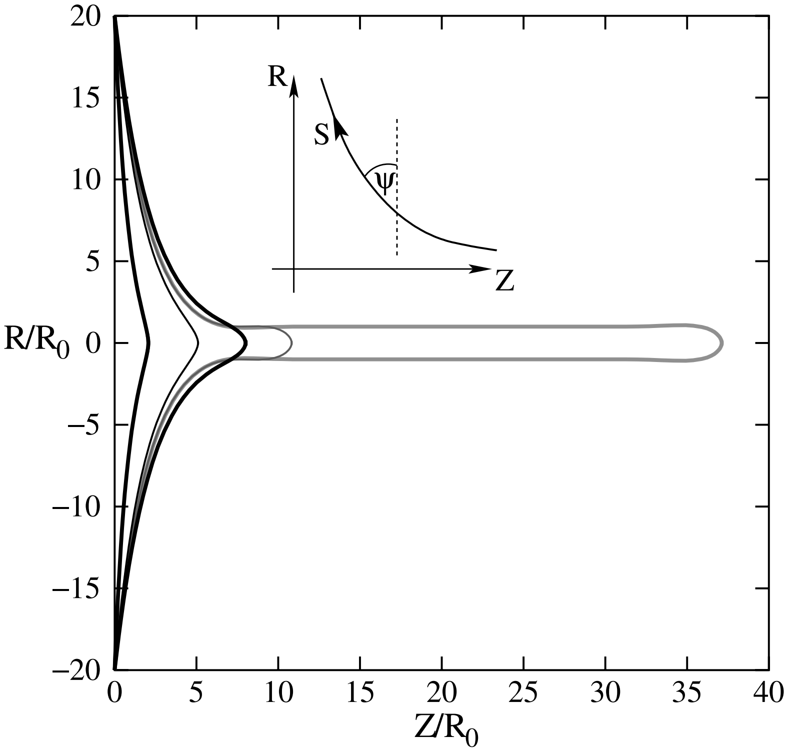

Figure 1.8: Figure showing the numerical solutions to the axisymmetric shape equations for a tube pulled from a ring with hinge boundary conditions. Details of the boundary conditions and method are given in the main text. Inset showing the angle, ψ, arclength, S, parametrization of surfaces axisymmetric about the Z axis. Figure adapted from [Derényi et al., 2002].

1.4.3 Shape equation for axisymmetric surfaces and formation of membrane tubes

A simplified case that is useful to consider is that of axisymmetric surfaces as, not only does the shape equation reduce to a boundary value ODE problem, but it turns out that many membrane shapes found in nature are approximately axisymmetric (for example red blood cells) [Jülicher and Seifert, 1994; Seifert, 1997]. Here we will label the axis of symmetry Z and parametrize the surface in terms of angle from the normal, $\psi(S)$, where S is the arclength, see Fig. 1.8 inset.

The radial and and symmetry axis coordinates are given by

$$\partial_S R = \cos\psi; \quad \partial_S Z = -\sin\psi, \tag{1.18}$$

and the shape equation becomes [Jülicher and Seifert, 1994; Derényi et al., 2002]

$$\begin{aligned}\partial_S^3\psi = &-\frac{1}{2}\left(\partial_S\psi\right)^3 - \frac{2\cos\psi}{R}\partial_S^2\psi + \frac{3\sin\psi}{2R}\left(\partial_S\psi\right)^2 + \frac{3\cos^2\psi - 1}{2R^2}\partial_S\psi \\ &+ \frac{\sigma}{\kappa}\partial_S\psi - \frac{\cos^2\psi + 1}{2R^3}\sin\psi + \frac{\sigma}{\kappa R}\sin\psi - \frac{\Delta P}{\kappa}.\end{aligned} \tag{1.19}$$

In practice this equation is difficult to integrate numerically due to being very unstable and computationally intensive semi-implicit methods are often required [Rahimi and Arroyo, 2012]. It is often easier to solve the first integral of this equation numerically [Derényi et al., 2002], which is given by

$$\begin{aligned}\partial_S^2\psi\cos\psi = &-\frac{1}{2}\left(\partial_S\psi\right)^2\sin\psi - \frac{\cos^2\psi}{R}\partial_S\psi + \frac{\cos^2\psi + 1}{2R^2}\sin\psi \\ &+ \frac{\sigma}{\kappa}\sin\psi - \frac{\Delta P}{2\kappa}R - \frac{f}{2\pi\kappa R}\end{aligned} \tag{1.20}$$

where f is a constant of integration that can be associated with a point force acting along the Z axis at $R = 0$. An alternative way of deriving this equation is to use a Hamiltonian field theory formulation of the Helfrich energy by introducing conjugate momenta. In that case the first integral of the shape equation is found as one of Hamilton's field equations [Jülicher and Seifert, 1994].

Solving Eq. (1.20) for a close to flat membrane ($\psi \ll 1$) gives the Green's function for the shape at linear order in the shape perturbation

$$Z_{\text{lin}}\left(R\right) = Z_0 - \frac{2f}{2\pi\sqrt{2\sigma\kappa}}\sqrt{\frac{\kappa}{2\sigma}}\left[\log\left(\frac{R}{\sqrt{2}R}\right) + K_0\left(\frac{R}{\sqrt{2}R}\right)\right] - \frac{\Delta P R^2}{2\sigma}. \tag{1.21}$$

Note that, for large distances away from the point force, the shape depends logarithmically on R [Derényi et al., 2002].

The full non-linear equation can be solved numerically, either with a shooting method [Derényi et al., 2002] or a relaxation scheme [Powers et al., 2002]. In the case of the shooting method with boundary conditions at zeros given by a ring ($R = R_{\text{ring}}$) and zero curvature ($\partial_S\psi = -\sin\psi/R$), the shape is found by shooting in ψ (essentially shooting for the value of the force) and setting the $\partial_{SS}\psi$ just using Eq. (1.20), then finding the curve that crosses the Z axis. The solutions to this are shown in Fig. 1.8.

Using these numerics it is possible to find the force needed to pull a tube and even study the equilibrium interaction between two tubes [Derényi et al., 2002]. To understand the force needed to pull a tube we will use a simpler model which, neglects the energy of the neck and cap of the tube, which gives the correct result for long tubes (as the energy of the base and cap are negligible as $L \to \infty$). The free energy of a membrane tube of length L is given by

$$F_{\text{tube}} = \mathcal{F}_{\text{tube}} L = \left(\frac{\pi\kappa}{R} + 2\pi\sigma R\right) L - fL, \tag{1.22}$$

taking the derivative with respect to the tube length, L, setting to zero and making use of the expression for the equilibrium radius of a pressure-less tube (Eq. (1.16)), gives the force needed to hold a tube at length L

$$f = \frac{2\pi\kappa}{R} = 2\pi\sqrt{2\sigma\kappa}, \tag{1.23}$$

which agrees with numerical solutions for long tubes found in [Derényi et al., 2002; Powers et al., 2002]. This corresponds to the interesting fact that, beyond some critical threshold in the small deformation regime, the force required to pull a tube is independent of its length.

1.4.4 Shape instability of a membrane tube

An interesting question to ask is the following; for what values of bending energy, κ, and surface tension, σ, is a tube of radius, R, stable to small undulations in its shape.

If we parametrize the radius of a tube as $r(\theta, z) = R + u(\theta, z)$ we can write the free energy as an expansion in u and its derivatives. We can choose to write u in terms of its Fourier modes as follows

$$u(\theta, z) = \sum_{q,m} \bar{u}_{q,m} e^{iqz + im\theta}, \tag{1.24}$$

where $q = \frac{2\pi n}{L}$ (where $n \in \mathbb{Z}$) and m are the Fourier variables conjugate to z and θ respectively.

If we assume all undulations preserve the volume of the tube we can show that $\bar{u}_{0,0} = -\frac{1}{2R}\sum_{q,m} |\bar{u}_{q,m}|^2$, and the free energy of the membrane tube can be written in the following way [Gurin et al., 1996; Komura and Lipowsky, 1992]

$$\mathcal{F} = \mathcal{F}_{\text{tube}} + \mathcal{F}^{(2)}, \tag{1.25}$$

where

$$\mathcal{F}^{(2)} = \sum_{q,m} |\bar{u}_{q,m}|^2 \frac{\kappa}{2R^2} \left(\left(\tilde{q}^2 + m^2\right)^2 - \frac{1}{2}\tilde{q}^2 - \frac{5}{2}m^2 + \frac{3}{2} - \frac{R^2\sigma}{\kappa}\left(1 - \tilde{q}^2 - m^2\right) \right) \tag{1.26}$$

where $\tilde{q} = qR$.

For $m \geq 1$ this is always stable, however for the $m = 0$ modes there is a possible instability. For zero bending energy this instability would simply correspond to the classical Rayleigh-Plateau instability [Rayleigh, 1892; Tomotika, 1935], and the second variation in the free energy would be negative for all $\tilde{q} = qR < 1$ and for any a value surface tension. In the case of a membrane tube with bending rigidity the criterion for this instability becomes

$$\sigma > \sigma_c = \frac{3\kappa}{2R^2} \tag{1.27}$$

which we will generally refer to as the criterion for a Pearling instability on a membrane tube throughout this thesis [Bar-Ziv and Moses, 1994; Nelson et al., 1995; Gurin et al., 1996]. When the full fluid dynamical problem is treated it can be shown that the fastest growing wavelength of the instability has the universal behaviour of $\tilde{q}_{\max} \sim 0.6$ for any surface tension sufficiently past the instability threshold ($\sigma \gtrsim \sigma_c$) [Nelson et al., 1995] (although the exact number does depend on the relative viscosity between inside and outside [Boedec et al., 2014]).

1.4.5 Shape fluctuations of membrane tubes

The bending energy for a lipid bilayer has a rigidity comparable to the energy scale of thermal fluctuations, typically $\kappa \sim 10k_BT$ where k_B is Boltzmann's constant and T is temperature [Boal, 2002]. Because of this the bilayer is highly susceptible to thermal fluctuations. As the free energy expansion in the previous section is Gaussian, we can compute the fluctuation spectrum in Fourier space exactly by making use of the equipartition result from statistical mechanics [Landau and Lifshitz, 1951; Safran, 1994]

$$\langle|\bar{u}_{q,m}|^2\rangle = \frac{1}{\mathcal{Z}} \int \mathcal{D}\bar{u}_{q,m} \bar{u}_{q,m} \bar{u}^*_{q,m} e^{-\mathcal{F}^{(2)}/(k_BT)} \tag{1.28}$$

where $\mathcal{D}\bar{u}_{q,m} = \prod_{q,m} \mathrm{d}\bar{u}_{q,m}$ and $\mathcal{Z}$ is the partition function given by

$$\mathcal{Z} = \int \mathcal{D}\bar{u}_{q,m} e^{-\mathcal{F}^{(2)}/(k_BT)} \tag{1.29}$$

which gives the result

$$\langle|\bar{u}_{q,m}|^2\rangle = \frac{k_B T R^2}{\kappa\left(\left(\tilde{q}^2+m^2\right)^2-\frac{1}{2}\tilde{q}^2-\frac{5}{2}m^2+\frac{3}{2}\right)-R^2\sigma\left(1-\tilde{q}^2-m^2\right)}. \tag{1.30}$$

It is interesting to note that the $m = 1$ modes diverge in the small $\tilde{q}$ limit as in this limit the fluctuations are essentially just a local translation of the cross section, thus the energy they cost tends to zero as $\tilde{q}$ goes to zero. An in depth discussion of the critical fluctuations of membrane tubes can be found in Ref. [Fournier and Galatola, 2007].

1.5 Fluid dynamics at cellular scales

Here we will present a brief discussion of fluid dynamics at the scale of cell biology, this subject is vast so we will not attempt to discuss many of the subtleties in depth, but refer the reader to other resources *e.g.* [Happel and Brenner, 1983; Purcell, 1977].

The equations of fluid dynamics are generally specified in terms of a continuity equation and momentum rate equation [Landau and Lifshitz, 1959]. The continuity equation is given in terms of the velocity, $\vec{v}$, and density, ρ, of a fluid

$$\partial_t \rho + \vec{\nabla}\cdot(\rho\vec{v}) = J \tag{1.31}$$

where J is a source/sink of mass in the fluid. In the case where the fluid is incompressible $\rho = \text{Const.}$, and has no sources or sinks, this reduces to the incompressibility condition

$$\vec{\nabla}\cdot\vec{v} = 0. \tag{1.32}$$

The rate of change of momentum is given in terms of velocity $\vec{v}$, density ρ, fluid stress tensor $T = T^{ij}\vec{e}_i \otimes \vec{e}_j$ and external force per unit volume $\vec{f}$ which are related by the Navier-Stokes equation

$$\rho\left(\partial_t\vec{v} + \vec{v}\cdot\vec{\nabla}\vec{v}\right) = \vec{\nabla}\cdot T + \vec{f}. \tag{1.33}$$

In the case of an incompressible Newtonian fluid the stress tensor is given by

$$T^{ij} = \eta\left(\nabla^i v^j + \nabla^j v^i\right) - P g^{ij} \tag{1.34}$$

where η is the viscosity, and P the pressure. We can write the equation in dimensionless form by making use of the viscosity and density along with some characteristic length-scale L and velocity v_0,

$$\partial_{\tilde{t}}\vec{u} + \vec{u}\cdot\vec{\nabla}\vec{u} = \frac{\eta}{Lv_0\rho}\left(\vec{\nabla}\cdot\tilde{T} + \vec{f}\right) = \frac{1}{\mathrm{Re}}\left(\vec{\nabla}\cdot\tilde{T} + \vec{f}\right) \tag{1.35}$$

where $\vec{u}$ is dimensionless velocity, $\tilde{t}$ dimensionless time, $\tilde{T}$ dimensionless stress and $\mathrm{Re} = \rho v_0 L/\eta$ is the Reynolds number of the flow. The Reynolds number is a dimensionless number which can be viewed as the ratio of viscous to inertial forces in the fluid; for large Reynolds number inertial forces dominate and the fluid is often in a highly non-linear regime. For small Reynolds numbers viscous forces dominate and the system can be viewed as over-damped. If we consider some estimates of these parameters at the scale of cells we might choose the following [Purcell, 1977; Milo and Phillips, 2015]

$$\begin{aligned}
&\eta \sim 10^{-3}\mathrm{Pa\ s}\\
&\rho \sim 10^{3}\mathrm{Pa\ s^2\ m^{-2}}\\
&L \sim 10^{-6}\mathrm{m}\\
&v_0 \sim 10^{-6}\mathrm{m\ s^{-1}}\\
&\implies \mathrm{Re} \sim 10^{-6}.
\end{aligned} \tag{1.36}$$

In this limit the equations of motion reduce to the Steady Stokes equations along with incompressibility

$$\eta\nabla^2\vec{v} = \vec{\nabla}P - \vec{f}; \quad \vec{\nabla}\cdot\vec{v} = 0 \tag{1.37}$$

which will be used throughout the rest of this thesis.

1.6 Overview of thesis

In this thesis we will aim to examine the dynamics of membrane tubes driven by various out of equilibrium processes designed to mimic situations in cell biology. The goal is to understand the physics underlying cellular processes with minimal models that capture the important biology and mechanics.

Chapter 2 deals with the shape instability of membrane tubes due to an osmotic pressure difference driven by ion pumps. These ion pumps consume ATP to actively move ions across the membrane against their concentration gradient. When oriented inwards we show that the increase in osmotic pressure causes the tube to swell, eventually leading to a Pearling-like instability, but with a much longer wavelength. This problem is inspired by the Contractile Vacuole Complex found in many single-celled freshwater organisms [Allen, 2000]. This organelle is responsible for regulating the osmotic pressure inside the cell by acting as a pump to remove excess water, and thus maintain cell volume. This tubular instability forms a vital part of the pumping cycle as the bulges collect water to be emptied into the main vesicle of the pump.

Chapter 3 focuses on the dynamics of membrane tubes where there is a shear gradient in the azimuthal fluid flow of the membrane, in part inspired by the action of Dynamin in fissioning membrane tubes and necks of vesicles [Roux et al., 2006; Roux, 2014]. By employing the methods of covariant hydrodynamics we analyse the stability of perturbations to the membrane tube's shape under this shear rate. We find a helical instability in the membrane tube shape whose handedness is set by the shear rate. Because of advection with the ground-state flow, the pitch length of the instability decreases until the shape eventually becomes stable, however we show that this instability provides significant amplification to the fluctuation spectra of the tube. This amplification gives rise to large non-equilibrium fluctuations of the tube that may play an important role in the, as yet, ill understood process of Dynamin mediated scission (perhaps via friction mediated scission similar to Ref. [Simunovic et al., 2017]).

The final section, Chapter 4, considers the full relaxation dynamics of membrane tubes (with variable surface tension) and their statistical mechanics under passive and active fluctuations. Here we consider a simple model of generic active fluctuations which break detailed balance in the system [Gov, 2004]. We compute the fluctuation spectra for these stochastic processes acting on the tube and the "effective temperature" of the Fourier modes of the tube shape. We discuss possible experiments to measure these fluctuations and how varying the viscosity could be used to quantify the activity in the system.

Chapter 2

Hydro-osmotic Instabilities in Active Membrane Tubes

In this chapter we study a membrane tube with unidirectional ion pumps driving an osmotic pressure difference. A pressure driven peristaltic instability is identified, qualitatively distinct from similar tension-driven Rayleigh type instabilities on membrane tubes. We discuss how this instability could be related to the function and biogenesis of membrane bound organelles, in particular the contractile vacuole complex. The unusually long natural wavelength of this instability is in agreement with that observed in cells. The analysis also provides a more general framework with which to approach hydrodynamic instabilities where slow driving is dominant.

2.1 Introduction

A key contemporary challenge in cellular biophysics is to understand the physical self-organization and regulation of organelles [Mullins, 2005; Chan and Marshall, 2012]. Eukaryotic organelles bound by lipid membranes perform a variety of mechanical and chemical functions inside the cell, and range in size, construction, and complexity [Alberts et al., 2002]. A quantitative understanding of how such membrane bound organelles function has applications in bioengineering, synthetic biology and medicine. Most models of the shape regulation of membrane bound organelles invoke local driving forces, e.g. membrane proteins that alter the morphology (often curvature) [Heald and Cohen-Fix, 2014; Shibata et al., 2009; Jelerčič and Gov, 2015]. However other mechanisms, such as osmotic pressure, could play an important role [Gonzalez-Rodriguez et al., 2015].

Membrane tubes are ubiquitous in cells, being found in organelles such as the endoplasmic reticulum and various post-Golgi compartments [Alberts et al., 2002]. Models for their formation typically involve the spontaneous curvature of membrane proteins [Shibata et al., 2009] or forces arising from molecular motors attached to the membrane that pull tubular tethers as they move along microtubules [Yamada et al., 2014]. Many of these tubules may contain trans-membrane proteins that can alter the osmotic pressure by active transport of ions. Most work on the biogenesis of cellular organelles has focused on their static morphology and generally not on their non-equilibrium dynamics. In what follows we consider an example in which the out-of-equilibrium dynamics drives the morphology, Fig. 2.1. Our study is inspired by the biophysics of an organelle called the contractile vacuole complex but additionally reveals a new class of instabilities not previously studied that are of broad, perhaps even universal, physiological relevance.

The contractile vacuole complex (CVC) is an organelle found in most freshwater protists and algae that regulates osmotic pressure by expelling excess water [Komsic-Buchmann et al., 2014; Stock et al., 2002; Allen, 2000; Naitoh et al., 1997; Docampo et al., 2013]. Its primary features are a main vesicle (CV) that is inflated by osmosis and periodically expels its contents through the opening of a large pore - probably in response to membrane tension - connecting it to the extracellular environment, thereby regulating cell volume [Patterson, 1980; Docampo et al., 2013]. Water influx into the CVC is due to an osmotic gradient generated by ATP-hydrolysing proton pumps in the membrane that move protons into the CVC [Stock et al., 2002; Heuser et al., 1993; Nishi and Forgac, 2002; Fok et al., 1995]. In many organisms such as *Paramecium multimicronucleatum*, the CVC includes several membrane tubular arms connected to the main vesicles, which are thought to be associated with the primary sites of proton pumping and water influx activity [Tominaga et al., 1998]. The tubular arms do not swell homogeneously in response to water influx, but rather show large undulatory bulges with a size comparable to the size of the main CV, leading us to speculate that this might even play a role in CV formation *de novo*. These tubular arms appear to be undergoing a process similar to the pearling or Rayleigh instability of a membrane tube under high tension [Rayleigh, 1892; Tomotika, 1935; Powers and Goldstein, 1997; Bar-Ziv and Moses, 1994; Bar-Ziv et al., 1997; Gurin et al., 1996; Nelson et al., 1995; Boedec et al., 2014] or an axon under osmotic shock [Pullarkat et al., 2006], but with a much longer natural wavelength: Rayleigh instabilities have a natural wave length $\lambda \sim R$ where R is the tube radius. Here we derive the dynamical evolution of a membrane tube driven out-of-equilibrium by osmotic pumping, which results in a much longer natural wavelength for the instability.

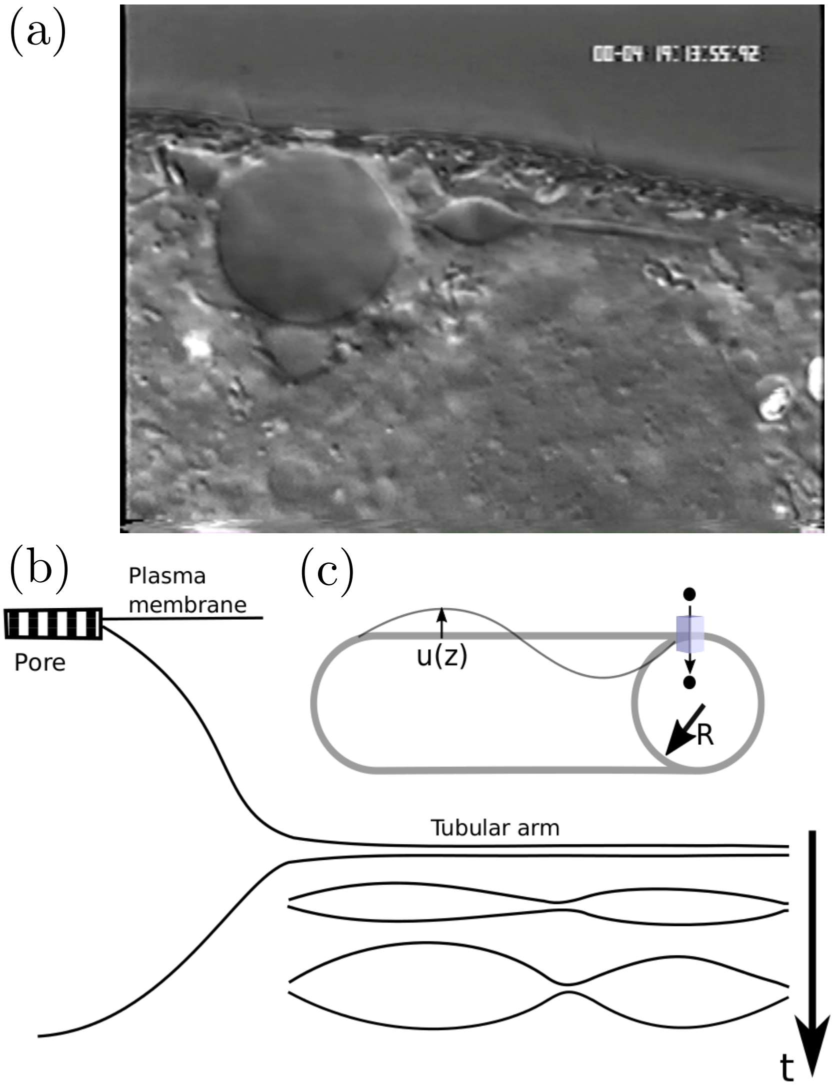

Figure 2.1: (a) Microscopy image of the contractile vacuole in *paramecium multimicronucleatum* adapted from [Tani et al., 2000]. (b) Diagram of the contractile vacuole complex. The tube is shown connected to the main body of the CV (left). As ions are pumped in, increasing the osmotic pressure, the tube undergoes a swelling instability and undulations develop with some wavelength λ. This phenomenon is observed in the contractile vacuoles of many protists, e.g. *paramecium multimicronucleatum* [Patterson, 1980; Allen, 2000]. (c) Schematic of a membrane tube with ion pumps and surface undulations. A cartoon of a representative ion pump is shown in the top right.

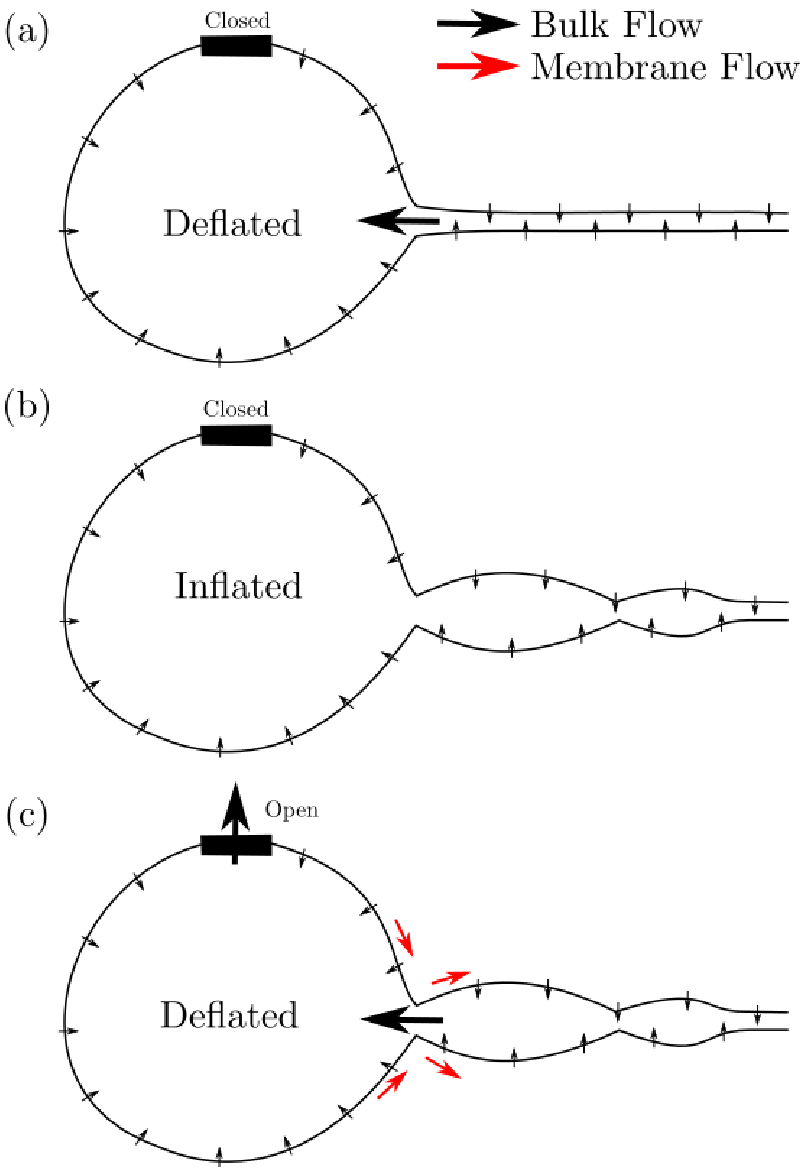

Figure 2.2: Flow dynamics of the contractile vacuole complex (CVC) (a) Initial stage of CVC inflation where water (bulk fluid) is transported into the tubes and main vesicle due to an ion pump driven osmotic pressure difference. In this state the pore connecting to the cellular exterior is closed. (b) In the inflated state of the CVC water stops flowing down the tubes into the main vesicle as it is fully inflated and at high pressure. The tubes then swell and undergo an instability. (c) The pore opens and the main vesicle deflates, expelling water. Water from the tubes is driven into the main vesicle as membrane flows back onto the tubes. Sometime during this process the pore closes, the tube deflates and we return to the initial scenario.

In the CVC, the tubular arms are surrounded by a membrane structure resembling a bicontinuous phase made up of a labyrinthine tubular network called the smooth spongiome (SS). We assume this to represent a reservoir of membrane keeping membrane tension constant and uniform during tube inflation.

A schematic of of the bulk and membrane flow dynamics associated with the expulsion cycle of the CVC is shown in Fig. 2.2. In this chapter we will deal only with the early stages of tube inflation and not the highly non-linear expulsion dynamics later in the cycle, Fig. 2.2(c).

2.2 Membrane mechanics

The CVC is comprised of a phospholipid bilayer membrane. This bilayer behaves in an elastic manner [Helfrich, 1973; Phillips et al., 2010]. At physiological temperatures these lipids are in the fluid phase [Alberts et al., 2002; Phillips et al., 2010]. For simplicity we will treat the bilayer as a purely elastic, fluid membrane in the constant tension regime, neglecting the separate dynamics of each leaflet. The membrane free energy involves the mean curvature H and surface tension σ [Helfrich, 1973; Safran, 1994; Nelson et al., 2004] and is given by

$$\mathcal{F} = \int_{\mathcal{S}} \mathrm{d}A \left(\frac{\kappa}{2} (2H)^2 + \sigma \right) - \int \Delta P \mathrm{d}V, \tag{2.1}$$

where $\mathrm{d}A$ and $\mathrm{d}V$ are the area and volume elements on $\mathcal{S}$, κ is the bending rigidity, and ΔP is the pressure difference between the fluid inside and outside the tube (see also Eq. (1.8)).

2.2.1 Differential geometry of the membrane

For the membrane tubes in which we are interested we parametrise the bilayer as an embedding in $\mathbb{R}^3$. Utilising the cylindrical symmetry of the membrane tube we write this as a surface of revolution about the z axis with radius $r(z,t)$. This means that we will only consider squeezing (peristaltic) modes in our analysis. In Cartesian coordinates this surface is parametrised by the vector $\vec{R} = (r\cos\theta, r\sin\theta, z)$, i.e. by the normal cylindrical polar coordinates where $r(z,t)$ is the radial distance of the axisymmetric membrane from the cylindrical symmetry axis and z measures the coordinate along that axis. From this we can define tangent vectors on the manifold as

$$\vec{e}_1 = \frac{\partial \vec{R}}{\partial \theta} = (-r\sin\theta, r\cos\theta, 0) \tag{2.2}$$

$$\vec{e}_2 = \frac{\partial \vec{R}}{\partial z} = (\partial_z r\cos\theta, \partial_z r\sin\theta, 1)\,. \tag{2.3}$$

This allows for the definition of a Riemannian metric as

$$g_{ij} = \vec{e}_i \cdot \vec{e}_j \quad \text{for} \quad i, j = \{1, 2\}. \tag{2.4}$$

Hence the metric and its inverse are

$$g = \begin{bmatrix} r^2 & 0 \\ 0 & 1 + (\partial_z r)^2 \end{bmatrix}, \quad g^{-1} = \begin{bmatrix} \frac{1}{r^2} & 0 \\ 0 & \frac{1}{1+(\partial_z r)^2} \end{bmatrix}. \tag{2.5}$$

To find the curvature of $\mathcal{S}$ we need to know how the normal vector, $\vec{n}$, to the surface S varies. We can write this normal vector as

$$\vec{n} = \frac{\vec{e}_1 \times \vec{e}_2}{|\vec{e}_1 \times \vec{e}_2|} = \frac{1}{\sqrt{1 + (\partial_z r)^2}} (\cos\theta, \sin\theta, -\partial_z r)\,. \tag{2.6}$$

From this we can find the second fundamental form $b_{ij} = \vec{n} \cdot \vec{e}_{i,j}$ where the comma denotes a partial derivative. Taking the determinant and trace of

$$b_i^{\,j} = \frac{1}{\sqrt{1 + (\partial_z r)^2}} \begin{bmatrix} \frac{-1}{r} & 0 \\ 0 & \frac{\partial_{zz} r}{1+(\partial_z r)^2} \end{bmatrix}, \tag{2.7}$$

we find the mean and Gaussian curvatures

$$2H = \frac{1}{\sqrt{1 + (\partial_z r)^2}} \left(\frac{\partial_{zz} r}{1 + (\partial_z r)^2} - \frac{1}{r} \right) \tag{2.8}$$

$$K = \frac{-\partial_{zz} r}{r\left(1 + (\partial_z r)^2\right)^2}. \tag{2.9}$$

Assuming radial symmetry and integrating over the volume of the tube we obtain

$$\mathcal{F} = 2\pi \int_{-\infty}^{\infty} \mathrm{d}z \left[\frac{\kappa}{2} r \frac{1}{\sqrt{1+(\partial_z r)^2}} \left(\frac{\partial_{zz} r}{1+(\partial_z r)^2} - \frac{1}{r} \right)^2 \right. \\ \left. + \sigma r \sqrt{1+(\partial_z r)^2} - \frac{1}{2} r^2 \Delta P \right]. \quad (2.10)$$

We use Eq. (2.10) as a model for the free energy of a radial arm of the CVC. Ion pumps create an osmotic pressure difference that drive a flux of water to permeate through the membrane. We calculate the dominant mode of the hydro-osmotic instability resulting from the volume increase of the tube lumen. We write the radius of the tube as $r(z,t) = R + u(z,t)$, with u assumed small, and make use of the Fourier representation $u(z,t) = \sum_q \bar{u}_q e^{iqz}$. Absorbing the $q = 0$ mode into $R = R(t)$ allows us to write $\int u \, \mathrm{d}z = 0$. The free-energy per unit length can be written at leading order as

$$\mathcal{F} = \mathcal{F}^{(0)} + \frac{\pi}{R} \sum_q \alpha(q) |\bar{u}_q|^2 \quad (2.11)$$

where

$$\alpha(q) = \frac{\kappa}{R^2} \left((qR)^4 - \frac{(qR)^2}{2} + 1 \right) + \sigma (qR)^2 - \Delta P R \quad (2.12)$$

and

$$\mathcal{F}^{(0)} = 2\pi \left(\frac{\kappa}{2R} + \sigma R - \frac{1}{2} \Delta P R^2 \right) \quad (2.13)$$

Identifying the static pressure difference ΔP with the Laplace pressure $P_L = -\kappa/(2R^3) + \sigma/R$, the point at which the $q = 0$ mode goes unstable can be identified: the membrane tube is unstable for tube radii $R > \sqrt{3} R_{\mathrm{eq}}$ where $R_{eq} = \sqrt{\frac{\kappa}{2\sigma}}$ is the equilibrium radius of a tube with $\Delta P = 0$. This criterion for the *onset* of the instability is the same as the Rayleigh instability on a membrane tube [Gurin et al., 1996], however the instability is now driven by pressure not surface tension. This is a crucial difference. It leads to a qualitatively different evolution of the instability, as we now show. In what follows we are interested in the dynamics of the growth of unstable modes after the cylinder has reached radius $\sqrt{3} R_{\mathrm{eq}}$. Our initial condition is a tube under zero net pressure, although the choice of initial condition is not crucial.

2.3 Dynamics of active ion pumps

We assume that the number of proton pumps moving ions from the cytosol into the tubular arm depends only on the initial surface area, i.e. it is fixed as the tube volume (and surface) varies. We denote the number of ions per unit length in the tube as n and write an equation for the growth of n as

$$\frac{\mathrm{d}n}{\mathrm{d}t} = \begin{cases} 0, & t \in (-\infty, 0) \\ 2\pi\beta R_{eq}, & t \in [0, \infty) \end{cases} \tag{2.14}$$

where β is a constant equal to the pumping rate of a single pump multiplied by the initial area density of pumps. This assumes that the ion pumps are diffusing sufficiently fast so as to be homogeneously distributed, this assumption is chosen so as to simplify the calculations. The ion pumps are assumed to switch on at $t = 0$ and that the tube was in thermal equilibrium prior to that time.

The density of ions, ρ_I, can be obtained by solving Eq. (2.14) and dividing by volume per unit length, $v(t)$,

$$\rho_I = \frac{n(t)}{v(t)} = \frac{n_0}{v(t)} + \frac{2\pi\beta R_{eq} t}{v(t)}. \tag{2.15}$$

The growth of the tube radius is driven by a difference between osmotic and Laplace pressure [Chabanon et al., 2017]. This means the rate equation for the increase in volume can be written in terms of the membrane permeability to water. Assuming that the water permeability (number of water permeable pores) is constant during tube inflation, we write the volume permeability per unit tube length $\mu' = 2\pi R_{eq}\mu$, where μ is the (initial) permeability of the membrane. Thus

$$\frac{\mathrm{d}v}{\mathrm{d}t} = \mu' \left(k_B T \left(\rho_I - \rho_I \left(t = 0 \right) \right) - \Delta P \right) \tag{2.16}$$

where the osmotic pressure is approximated by an ideal gas law. If we expand this equation to lowest order in the shape undulations it can be transformed into an equation for $R(t)$ on the time interval $t \in [0, \infty)$. This allows us to solve the dynamics hierarchically in the shape undulations where the flow and permeation generated by higher order terms will be discussed for in the next section. We identify ΔP with the Laplace pressure of a uniform tube. This leads to

$$\frac{\mathrm{d}\tilde{R}}{\mathrm{d}\tilde{t}} = \frac{\tau_{\mathrm{pump}}}{\tau_\mu} \frac{1}{\tilde{R}} \left(\frac{\tilde{t}}{\tilde{R}^2} + \left(1 + \frac{\tilde{\sigma}}{\tilde{R}} \right) \left(\frac{1}{\tilde{R}^2} - 1 \right) \right) \tag{2.17}$$

where $\tilde{\sigma} = \frac{\sigma}{k_B T R_{eq} \rho_I(t=0)}$, $\tau_{\text{pump}} = \frac{R_{eq}\rho_I(t=0)}{2\beta}$, $\tilde{t} = \frac{t}{\tau_{\text{pump}}}$, $\tilde{R} = \frac{R}{R_{eq}}$ and $\tau_\mu = \frac{R_{eq}}{\mu' k_B T \rho_I(t=0)}$. τ_{pump} and τ_μ represent the time-scales of pumping and permeation of water respectively. The experimental time-scale for radial arm inflation is consistent with a value of $\tau_{\text{pump}} \sim 10^{-1} - 1$s. These dynamics assume our ensemble conserves surface tension, not volume (as in the usual Rayleigh instability). This proves to be a crucial difference.

Values of $R_{eq} = 25$nm, $\sigma = 10^{-4}$N m^{-1} and hence κ are estimated using experimentally measured values from [Zimmerberg and Kozlov, 2006; Koster et al., 2003]. We take a typical ionic concentration in the cytosol of a protist for $\rho_I(t = 0) = 3.0 \times 10^8 \mu\text{m}^{-3}$ (around 10 mMol) [Stock et al., 2002; Phillips et al., 2010; Jackson, 2006]. Making an order of magnitude estimate of β from the literature on the CVC [Stock et al., 2002; Allen and Fok, 1988; Tani et al., 2000] leads to estimates of $\beta \sim 10^6$-$10^9 \mu\text{m}^{-2}\text{s}^{-1}$. Temperature is taken as $T = 310$K. The permeability of polyunstaurated lipid membranes is thought to be around $\mu = 10^{-4} \mu\text{m Pa}^{-1}\text{s}^{-1}$ [Olbrich et al., 2000]. This permeability could be much larger in the presence of water channels but we find that our results are rather insensitive to increasing the value of μ because, for physiological parameter values, our model remains in the rapid permeation regime, i.e. $\tau_\mu/\tau_{\text{pump}} \ll 1$. This permits a multiple time-scales expansion [Murray, 1992] of Eq. (2.17). With $\tilde{\sigma} \sim 10^{-3} \ll 1$ we find the approximate asymptotic solution

$$\tilde{R}(t) = \left(\frac{t}{\tau_{\text{pump}}} + 1\right)^{1/2} + \mathcal{O}\left(\frac{\tau_\mu}{\tau_{\text{pump}}}\right). \tag{2.18}$$

This solution agrees well with numerical solutions to Eq. (2.17), see Appendix A for more details.

2.3.1 Case of an osmotic shock

We can consider a tube with a fast-acting tension reservoir (something similar to the smooth spongiome), undergoing osmotic shock. It is interesting to understand the dominant wavelength selection in such a case as the system may be easier to implement *in vitro* than systems involving unidirectional ion pumps. If the radial expansion of the membrane is driven by a hypo-osmotic shock, the radial dynamics are governed by the following growth equation

$$\frac{\mathrm{d}\tilde{R}}{\mathrm{d}\tilde{t}} = \frac{1}{\tilde{R}}\left(\frac{1}{\tilde{R}^2}\frac{\Delta\rho}{\rho_0} + \left(1 + \frac{\tilde{\sigma}}{\tilde{R}}\right)\left(\frac{1}{\tilde{R}^2} - 1\right)\right) \tag{2.19}$$

where $\tilde{t} = \frac{t}{\tau_\mu}$, $\tilde{\sigma} = \frac{\sigma}{k_B T R_{eq} \rho_0}$, $\tilde{R} = \frac{R}{R_{eq}}$, $\tau_\mu = \frac{R_{eq}}{\mu k_B T \rho_0}$ and $\Delta\rho = \rho_0 - \rho_{\text{shock}}$ is the change in ionic density of the outside medium due to osmotic shock. Note that the normalisation chosen here is different from the one used for ion pumps.

2.4 Dynamical instability in the axisymmetric shape perturbation

We now proceed to deriving the dynamical equations for the Fourier modes. The equations governing the solvent flow are just the standard inertia free fluid equations for velocity field $\vec{v}$. These are the continuity and Stokes equations for incompressible flow

$$\vec{\nabla} \cdot \vec{v} = 0; \quad \vec{\nabla} P = \eta \nabla^2 \vec{v} \tag{2.20}$$

where P is the hydrodynamic pressure and $\eta = 10^{-3}\text{Pa} \cdot \text{s}$ the viscosity. The linearised boundary conditions are: $v_r|_{r=R} = \dot{u} + v_p$, where v_p is the permeation velocity (proportional to the hydrodynamic pressure jump across the membrane: $v_p = \mu \Delta P|_{r=R}$), and $v_z|_{r=R} = 0$. The second condition is justified by invoking the membrane reservoir as a mechanism for area exchange. This exchange is assumed to happen on time-scales set by the membrane viscosity and area expansion modulus of the membrane, which gives a time-scale for tension relaxation of $\tau_\sigma \sim 10^{-7}\text{s}$ [Keren et al., 2008; Shi et al., 2018]. We will be considering the dynamics in the long wavelength limit and as such neglect the hydrodynamics of the membrane as, at large length-scales compared to the tube radius, bulk dissipation dominates [Seifert and Langer, 1994].

If we write the velocity field in terms of a stream function ψ as

$$\vec{v} = \frac{1}{r} \left(\partial_z \psi \vec{e}_r - \partial_r \psi \vec{e}_z \right) \tag{2.21}$$

the continuity equation is automatically satisfied, and the Stokes equations can be solved to give

$$\psi = \begin{cases} \sum_q A_1 q r I_1(qr) + B_1 (qr)^2 I_0(qr) & r < R \\ \sum_q A_2 q r K_1(qr) + B_2 (qr)^2 K_0(qr) & r > R \end{cases} \tag{2.22}$$

in the interior of the tube, where $A_{1,2}$ and $B_{1,2}$ are found from the boundary conditions. $I_\nu(x)$ and $K_\nu(x)$ are modified Bessel functions of the first and second kind respectively.

From here we use the equation $v_p = \mu(\Delta P)|_{r=R}$, where $\Delta P|_{r=R}$ is the hydrodynamic pressure jump across the tube membrane, and use the solution of the interior and exterior hydrodynamic pressure from the Stokes equations to find a value of v_p. In Fourier space this gives

$$\bar{v}_p = \dot{\bar{u}}_q \left(\frac{1}{2q\eta\chi(q)\mu} - 1 \right)^{-1} \tag{2.23}$$

where

$$\chi(q) = \frac{I_0 \left(I_0 - 1\right)}{qRI_0^2 - 2I_0 I_1 - qRI_1^2} - \frac{K_0^2}{qRK_0^2 + 2K_0 K_1 - qRK_1^2} \tag{2.24}$$

with $I_\nu = I_\nu(qR)$ and $K_\nu = K_\nu(qR)$.

The force balance equation at the membrane reads

$$\left(P - 2\eta\partial_r v_r\right)|_{r=R} = f \tag{2.25}$$

where f is the force required to displace the membrane to u and can be found from the free energy. Substituting the velocity and pressure fields into this gives the dynamic equation for the modes $\bar{u}_q$

$$\dot{\bar{u}}_q = -\frac{\alpha_L\left(q\right)}{2\eta R}\frac{1}{X\left(q\right)}\left(1 - 2q\mu\chi(q)\right)\bar{u}_q \tag{2.26}$$

$$X(q) = \frac{I_0\left(qRI_0 - I_1\right)}{qR\left(I_1^2 - I_0^2\right) + 2I_1 I_0} + \frac{K_0\left(qRK_0 - K_1\right)}{qR\left(K_1^2 - K_0^2\right) + 2K_1 K_0} \tag{2.27}$$

with the shorthand $I_\nu = I_\nu(qR)$ and $K_\nu = K_\nu(qR)$ [Gurin et al., 1996]. The elastic response function $\alpha_L(q)$ is obtained by replacing the pressure ΔP by the Laplace presure $\Delta P_L = \sigma/R - \kappa/(2R^3)$, which gives

$$\alpha_L(q) = \frac{\kappa}{R^2}\left((qR)^4 - \frac{1}{2}(qR)^2 + \frac{3}{2}\right) + \sigma\left((qR)^2 - 1\right). \tag{2.28}$$

Eq. (2.26) can be used to describe the dynamical instability of a membrane tube subjected to different driving mechanisms; an increase of membrane tension (Rayleigh instability), an osmotic shock, or the slow active pumping mechanism we are primarily interested in. In the limit $qR \ll 1$ this gives

$$\dot{\bar{u}}_q = -\alpha_L(q)\left(\frac{q^2 R(t)}{8\eta} + \frac{2\mu R(t)}{R_{\text{eq}}^3}\right)\bar{u}_q \tag{2.29}$$

where $\bar{u}_q$ is the Fourier representation of u in the z direction. The response function α_L is obtained by replacing the static pressure difference by the Laplace pressure

ΔP_L in Eq. (2.12). Note that the term involving μ, capturing mode growth due to permeation, is only relevant for wavelengths $\lambda > 100R_{\mathrm{eq}}$, hence we will discard it in our analysis for simplicity (but retain it in the numerics for completeness). The growth rate for a given mode is now time dependent, hence the mode amplitude cannot be obtained from the maximum of the growth rate, but depends on the growth history and must be obtained by solving the full, time-dependent problem. We identify the instability as being fully developed when our linearised theory breaks down. We define the dominant mode of the instability, called $\hat{q}$, as the first mode with an amplitude reaching $\sqrt{\langle|\bar{u}_{\hat{q}}|^2\rangle} = R_{\mathrm{eq}}$ (a choice that does not influence our results, see Appendix A). We define the time when this occurs as $t = t_{\mathrm{final}}$.

We define the instantaneous growth rate $G(\tilde{q}) = \frac{\dot{\bar{u}}_q}{\bar{u}_q}$ from Eq. (2.26). This growth rate shows a peak as a function of q. The location of the peak depends on how the instability is driven. Starting with a stable tube under zero pressure with radius R_0 and membrane tension σ_0, the instability can be driven by an increase of tension $\sigma > \sigma^* = 3\sigma_0$ (see Eq. (1.27)) at constant volume (Rayleigh instability), or by an increase in volume (or radius) $R > R^* = \sqrt{3}R_0$ at constant tension (Osmotic instability). In the former case, and in the limit $\sigma \gg \sigma^*$, the growth rate reaches a universal shape with a peak at $R_0 q^* \simeq 0.6$. The most unstable wavelength is thus entirely set by the initial tube geometry (its radius R_0). In the latter, the peak of the growth rate depends on the time-dependent radius and does not reach any sort of universal behaviour. In fact the location of the peak is a non-monotonic function of the radius, first increasing, then decreasing with increasing radius. Its largest possible value is $R_0 q^* \simeq 0.2$ and occurs for $R \simeq 2.35R_0$, see Fig. 2.3.

The growth rate relation is quantitatively different from a Rayleigh instability due to the driving mechanism. The functional dependence of the growth rate relation depends on the polynomial $\alpha_L(q)$ describing the membrane mechanics in q space, Eq. (2.28). The Rayleigh instability is driven by a surface tension $\sigma > 3\kappa/(2R_0^2)$ at constant volume ($R(t) = R_0$), so that the magnitude of the q^4 term in Eq. (2.28) doesn't change. In the case of osmotic pressure however, the instability is driven by a change in volume caused by the osmotic pressure, i.e. $R > \sqrt{3\kappa/(2\sigma)}$. This increases the prefactor to the q^4 term which means that the higher q modes are stabilised compared to the Rayleigh case. This means that the dominant wavelength is skewed towards smaller q, Fig. 2.4.

As the fastest growing mode changes in time, it is the cumulative growth that is important. This means we must integrate the growth of each $\tilde{q}$ mode over time, accounting for fluctuations.

The fluctuations of modes with wavenumber q about the radius $R(t)$ follow

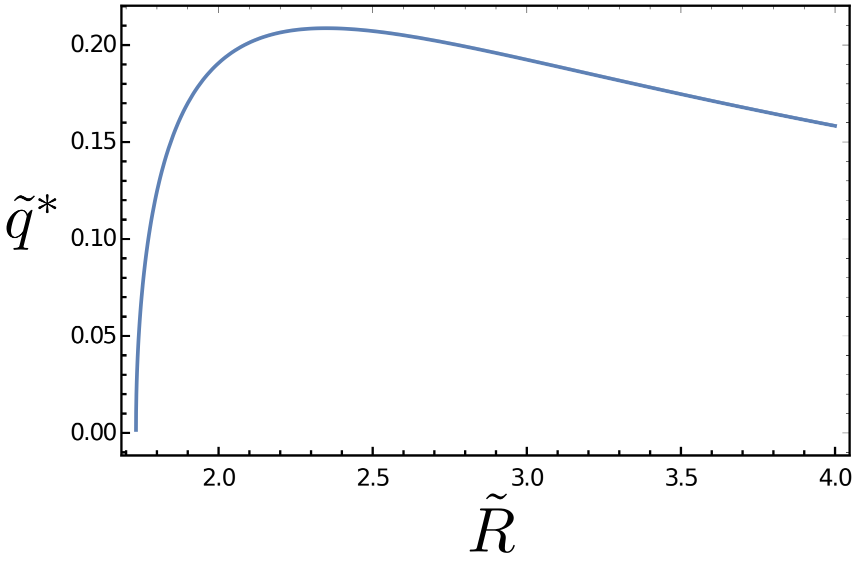

Figure 2.3: Location of the peak of the growth rate ($\tilde{q}^* \equiv R_{eq} q^*$) for a tube under constant tension, as a function of the tube radius. The initial tube radius R_{eq} corresponds to the equilibrium radius of a tube under zero pressure.

the dynamics of the Langevin equation based on Eq. (2.29)

$$\dot{\bar{u}}_q = -\frac{\alpha_L(q)}{\eta(q)}\bar{u}_q + \zeta_q \tag{2.30}$$

where $\eta(q) = 8\eta/(Rq^2)$ and ζ_q, the thermal noise, has the following statistical properties

$$\langle \zeta_q \rangle = 0 \tag{2.31}$$

$$\langle \zeta_q(t_1)\zeta_{q'}(t_2)\rangle = \delta_{qq'}\delta\left(t_1 - t_2\right)\frac{k_B T R}{\pi\eta(q)}. \tag{2.32}$$

Here the thermal noise is found using the equipartition theorem, and thus only gives the fluctuations of the $m = 0$ mode. We have considered only thermal noise here as the main purpose is to provide a background from which the instability is seeded (and our results seem to be insensitive as to the exact functional form of the noise). One might want to consider various forms of active noise which break the fluctuation dissipation theorem as such forces are likely to dominate the fluctuation spectra [Manneville et al., 2001; Ramaswamy et al., 2000; Gov, 2004]. Possible sources of active noise could include: sharp noise “kicks” from the ion pumps, fluctuations from the surrounding cytoskeleton and noise from the concentration fluctuations of ions. We will consider a simple minimal model of these types of active fluctuations

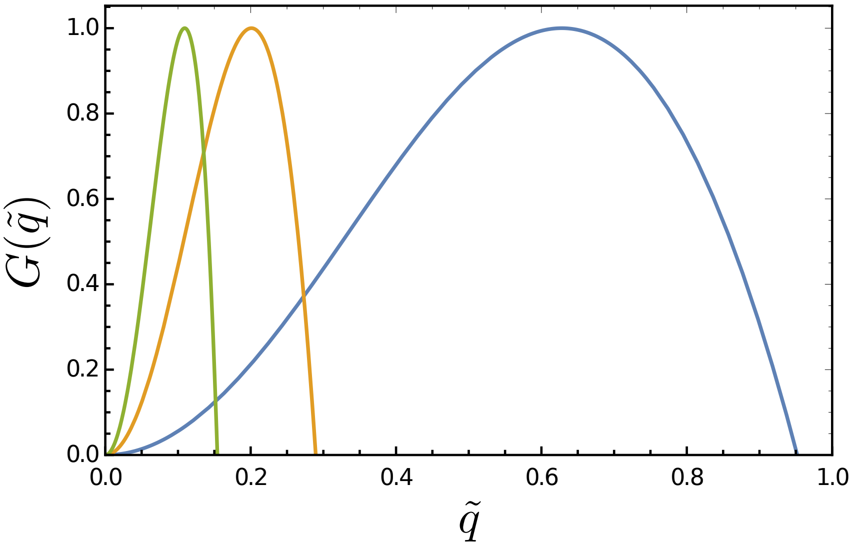

Figure 2.4: Normalized growth rate relation for a membrane tube undergoing a Rayleigh instability ($R_0 \sim 10^{-2}\mu$m, $\mu = 0$, $\kappa = 10k_BT$, $\sigma = 89\sigma_0$, where $\sigma_0 = \kappa/(2R_0^2)$) or responding to an osmotic shock under constant membrane tension ($R(t=0) = R_{eq} = 10^{-2}\mu$m, $\mu = 10^{-4}\mu$m Pa^{-1}s^{-1}, $\kappa = 10k_BT$, $\tilde{R}(t) = 2.35$). These parameters are chosen such that they illustrate the growth rate relations in the high tension limit for the Rayleigh instability (blue curve), or correspond to the maximal peak wavelength in the case of osmotic shock (orange curve). The dispersion relation for the Rayleigh instability is obtained from Eq. (2.26), with constant radius and the limit $\mu \to 0$. For comparison the typical growth rate for physiological parameters in the case of slow pumping (with $\tilde{R} = \sqrt{3} + 0.05$) is also shown (green curve).

in Chapter 4.

Solving this Langevin equation for $\langle|\bar{u}_q|^2\rangle$, using an initial condition of an equilibrium tube and the approximate form of $\tilde{R}(t) = \sqrt{1+\tilde{t}}$ (Eq. (2.18)) we find an integral equation for the mode growth by using the standard methods of Itô calculus [Särkkä and Solin, 2019]

$$\frac{\langle|\bar{u}_q|^2\rangle}{R_{\mathrm{eq}}^2} = \frac{k_BT}{2\kappa\pi(1+\tilde{q}^4)}e^{\left(F(0)-F(\tilde{t})\right)} + e^{-F(\tilde{t})}\int_0^{\tilde{t}} \frac{k_BT\tilde{q}^2(\tilde{t}'+1)}{\kappa\pi}\frac{\tau_{\mathrm{pump}}}{\tau_\eta}e^{F(\tilde{t}')}\mathrm{d}\tilde{t}' \quad (2.33)$$

where t' is a time variable integrating over the noise kernel (in units of τ_{pump}), $\tau_\eta = 8R_{\mathrm{eq}}^3\eta/\kappa$, $\tilde{q} = qR_{eq}$ and

$$F(t) = \frac{2\tau_{\mathrm{pump}}\tilde{q}^2\tilde{R}(t)}{15\tau_\eta}\left(40 - 5\tilde{t} + \tilde{q}^2\tilde{R}(t)^2\left(3\tilde{t} - 2 + 6\tilde{q}^2\tilde{R}(t)^2\right)\right). \quad (2.34)$$

Integrating this numerically, together with Eq. (2.18), we can find the dynamics of the modes. The distribution of mode amplitude against q is shown in Fig. 2.5. Although the smallest q modes go unstable first, they have very slow growth and so the mode that dominates the instability arises from the balance between going unstable early (favouring low q) and growing fast (favouring higher values of q).

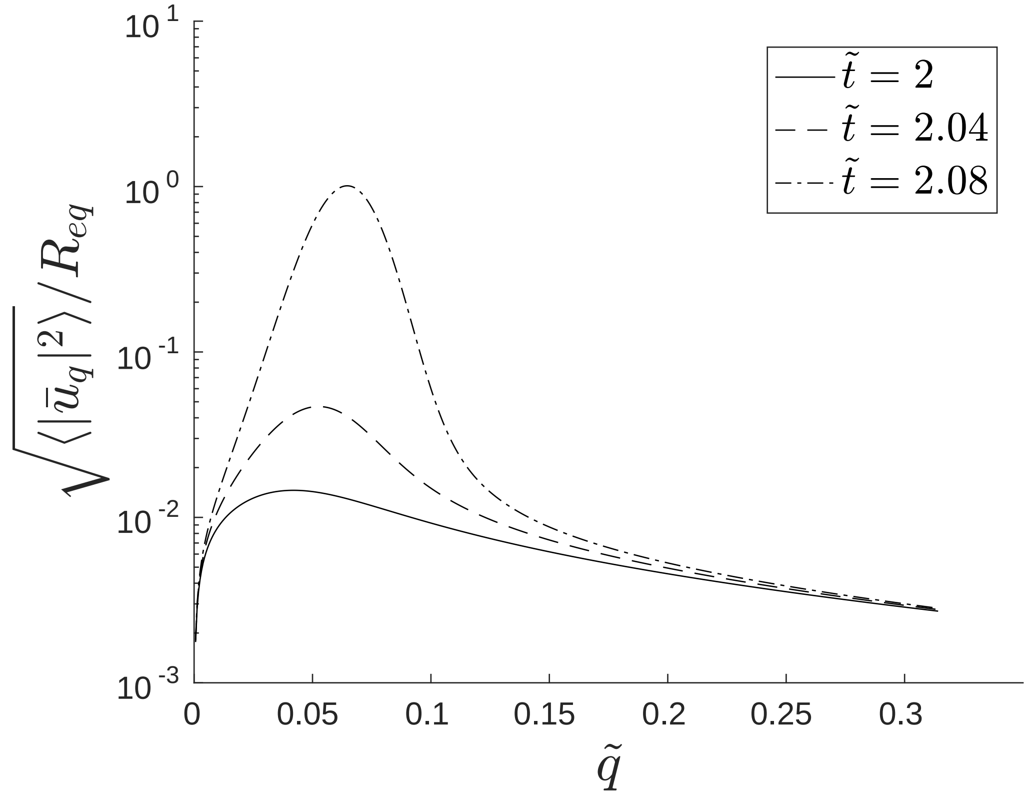

Figure 2.5: Plot of the distibution of mode amplitude $\sqrt{\langle \bar{u}_q^2 \rangle}$ against scaled wavenumber $\tilde{q} = qR_{\text{eq}}$ for $\tilde{t} = 2.0$ (solid), 2.04 (dashed) and 2.08 (dash-dotted, the time when the first mode reaches $\sqrt{\langle \bar{u}_q^2 \rangle} = R_{eq}$), $\tau_\eta/\tau_{\text{pump}} \sim 10^{-6}$. $R_{eq} = 25\text{nm}$, $\sigma = 10^{-4}\text{N m}^{-1}$ and $\rho_I(t = 0) = 3.0 \times 10^8 \mu\text{m}^{-3}$

We can compute numerically the natural wavelength associated with the dominant mode, $\hat{q}$, the first to reach $\sqrt{\langle|\bar{u}_q|^2\rangle} = R_{\text{eq}}$, see Fig. 2.6. This gives a dominant wavelength $\lambda \sim 100\ R_{eq} \sim 2\mu\text{m}$ for parameters consistent with the CVC, much larger than that found in the Rayleigh instability, but consistent with observations of the CVC [Allen, 2000]. Understanding why this is the case is not straightforward by inspection of the growth equation Eq. (2.33), but is more easily done by considering the time-dependent growth rate Eq. (2.29). Indeed, at the time

$t = t_{\mathrm{final}}$, the dominant mode $\hat{q}$ whose amplitude reaches $\sqrt{\langle|\bar{u}_{\hat{q}}|^2\rangle} = R_{\mathrm{eq}}$ is very close in value to the fastest growing mode (the peak of the instantaneous growth rate) at that particular time, written q^*, which can be derived analytically as a function of the tube radius from Eq. (2.29). As a result of the quasi-static driving of the instability by the ion pumps, the final radius is always only marginally above the critical radius $\sqrt{3}R_{\mathrm{eq}}$.

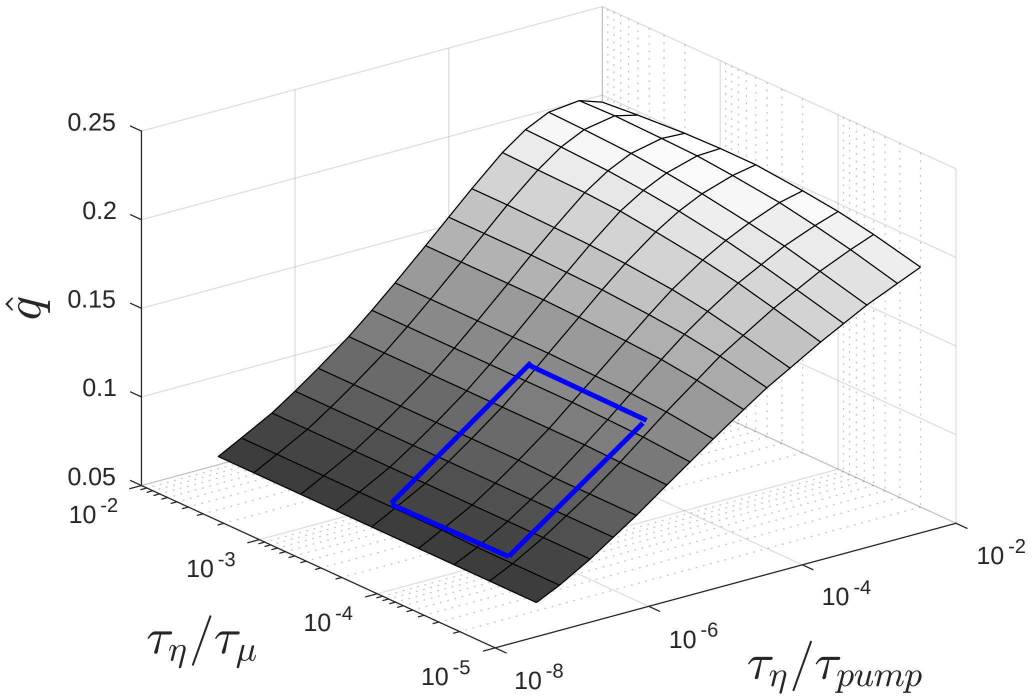

Figure 2.6: Plot of dominant wavenumber $\hat{q} = q^* R_{eq}$ of the instability against ratio of viscous to pumping timescales $\tau_\eta/\tau_{\mathrm{pump}}$ and ratio of viscous to permeable timescales, τ_η/τ_μ. All other parameters are the same as in Fig. 2.5. The blue rectangle indicates typical physiological parameters.

The fastest growing mode can be expressed in terms of $\delta\tilde{R}(t_{\mathrm{final}}) = \frac{\delta R}{R_{eq}} = \tilde{R}(t_{\mathrm{final}}) - \sqrt{3}$, Fig. 2.7. It is important to note that whilst the growth rate relation does give a good approximation to the dominant wavelength, there is a difference due to the history encoded in the full dynamical description.

The peak of the growth rate relation can be found analytically $(\frac{\mathrm{d}G}{\mathrm{d}\tilde{q}}|_{\tilde{q}^*} = 0)$, and in the small $\tilde{q}$ limit is

$$
\begin{aligned}
(\tilde{q}^*)^2 = & -\frac{1}{6} - \frac{16\eta\mu}{3R_{\mathrm{eq}}} + \frac{1}{6\tilde{R}^2} \\
& + \frac{\sqrt{-17 + 4\tilde{R}^2(1 + 8\frac{\eta\mu}{R_{\mathrm{eq}}}) + \tilde{R}^4(1 + 32\frac{\eta\mu}{R_{\mathrm{eq}}}(-1 + 32\frac{\eta\mu}{R_{\mathrm{eq}}}))}}{6\tilde{R}^2}
\end{aligned}
\tag{2.35}
$$

to leading order in $\delta\tilde{R}(t_{\mathrm{final}})$, in the $\mu \to 0$ limit, this can be expressed as $\tilde{q}^* = \frac{\left(\delta\tilde{R}(t_{\mathrm{final}})\right)^{1/2}}{\sqrt{2}(3)^{1/4}}$.

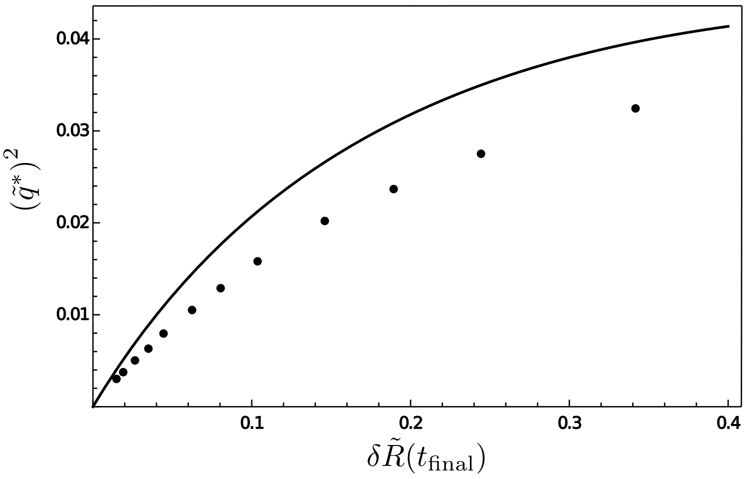

Figure 2.7: Dominant wave-number squared, $(\tilde{q}^*)^2$, plotted against final radius minus critical radius $\delta\tilde{R}(t_{\mathrm{final}}) = \tilde{R}(t_{\mathrm{final}}) - \sqrt{3}$, the solid line corresponds to the peak of the growth rate as a function of wavenumber and points represent the peak found by numerically solving the full dynamics.

This is the main factor contributing to the long wavelength/small q instability. While a qualitatively similar regime exists for tension driven instabilities, it is only valid very close to the instability threshold and its observation would require a very precise tuning of the tension. Far from threshold, the Rayleigh or pearling instability shows a universal relationship $\tilde{q}^* \sim 0.6R_{eq}$ [Bar-Ziv et al., 1997; Powers and Goldstein, 1997; Bar-Ziv and Moses, 1994; Boedec et al., 2014].

A related limit is that of an osmotic shock (which we detail in Appendix A). The difference between the Rayleigh and osmotic shock instabilities is due to the growth rate having a different response when driven by a volume change compared to surface tension. The constant volume (Rayleigh) instability might be of limited relevance for the morphological changes of cellular membrane tubes, as cellular membranes typically contain a host of membrane channels, including water channels, which allow fairly rapid water transport across the membrane. The osmotic instability that we analyse here recognises the presence of active pumps in the organelle membrane, which can drive osmotic changes in the organelle lumen [Allen, 2000]. There is some correspondence between the fast pumping limit in Fig. 2.6 ($\tau_\eta/\tau_{\text{pump}}$ large) and the osmotic shock situation. The instantaneous growth rates have the same dependence on the tube radius, but have a different time dependences as the dynamics of tube inflation is different in both cases. The osmotic shock limit is most likely not physiologically accessible to ion pumps. Crucially, one can see in Fig. 2.6 that the instability length scale is set by *dynamical* parameters, most importantly the ratio of the viscosity and pumping time-scales. Varying $\tau_\eta/\tau_{\text{pump}}$ has the effect of changing the time-scale over which the modes go unstable. It is fortuitous that the dominant wavelength does not depend strongly on the pumping rate, the parameter we can estimate least accurately (see Appendix A). This suggests a robustness to the wavelength selection that may have important implications for the CVC's biological function. In the physiologically accessible range of parameters for pumping and permeation, this length scale is much larger than the asymptotic limit for either the Rayleigh instability or the osmotic shock instability.

2.5 Discussion

We have developed a model for a water-permeable membrane containing uni-directional ion pumps. Hydro-osmotic instabilities realised in cells may be expected to usually lie in this class. Deriving dynamical equations for a membrane tube, we identify an instability driven by this osmotic imbalance. This has a natural wavelength that is set by dynamical parameters, specifically the ratio of the pumping time-scale to viscous time-scale, and is significantly longer than a Rayleigh or pearling instability. Interestingly it is of the same order as seen in the CVC radial arm suggesting that this is a possible mechanism behind the radial arm morphology. It is also interesting to note that the size of the bulge formed by the instability is of a similar order of magnitude to the size of the main CVC vesicle. We speculate that this instability may provide a mechanism for biogenesis of the CV from a featureless active tube. Throughout this analysis we have neglected the spontaneous curvature term in the Helfrich-Canham energy, Eq. 1.8. This would have the effect of renormalizing the surface tension of the tube, and can lead to a traditional pearling-like instability [Jelerčič and Gov, 2015]. For small values of spontaneous curvature which are not sufficient to induce pearling there is likely only some minor quantitative differences when compared with our analysis, however a detailed analysis for spontaneous curvature values close to the pearling threshold might yield some interesting results due to the interplay between length-scales. It might also be of interest to consider the case where the ion pumps couple to curvature and are allowed to diffuse allowing for effect similar to the active curvature instability seen in Ref. [Ramaswamy et al., 2000]. In the future we intend to further address the question of the CVC's *organellogenesis* which would likely require the implementation of a more realistic area-tension relation [Boedec et al., 2014].

Chapter 3

Shear-driven Instabilities on Membrane Tubes

Motivated by the mechanics of dynamin-mediated membrane tube scission we use covariant hydrodynamics to analyse the stability of fluid membrane tubes subjected to shear flow in azimuthal direction. We find a novel helical instability driven by the membrane shear flow which has its onset at shear rates that may be physiologically accessible under the action of dynamin and could also be probed using *in-vitro* experiments on membrane nanotubes, e.g. using magnetic tweezers. We discuss how such an instability may play a role in the mechanism for dynamin-mediated membrane tube scission.

3.1 Introduction

The covariant hydrodynamics of fluid membranes has been a subject of much interest in the soft matter and biological physics community in recent years, both for the general theoretical features of such systems [Cai and Lubensky, 1994, 1995; Fournier, 2015] and their application to biologically relevant processes [Sens, 2004; Arroyo and DeSimone, 2009; Brochard-Wyart et al., 2006; Morris and Turner, 2015; Morris, 2017]. Such systems couple membrane hydrodynamics with bending elasticity and have been shown to display complex visco-elastic behaviour in geometries with high curvature [Rahimi et al., 2013].

Membrane tubes are highly curved and are found in many contexts in cell biology, including the endoplasmic reticulum and the necks of budding vesicles [Kaksonen and Roux, 2018]. Such tubes can be pulled from a membrane under the action of a localized force (such as from molecular motors) [Derényi et al., 2002; Yamada et al., 2014; Cuvelier et al., 2005]. They are stable due to a balance between the forces from bending energy, involving the bending rigidity κ, and from the surface tension σ and have equilibrium radius $r_0 = \sqrt{\frac{\kappa}{2\sigma}}$ [Zhong-Can and Helfrich, 1989].

One of the simplest ways to drive flows on the surface of these tubes is to impose a velocity in the azimuthal direction. The analysis of shape changes induced by such flows is the subject of this chapter. Two possible mechanisms for realizing such flows via *in-vitro* and *in-vivo* experiments are shown in Fig. 3.1.

The fission of membrane tubes plays an important role in many cellular processes, ranging from endocytosis to mitochondria fission [McClure and Robinson, 1996; Frank et al., 2001]. The key component of the biological machinery required to induce membrane fission is a family of proteins called dynamin which hydrolyse GTP into GDP [Antonny et al., 2016; Roux et al., 2006]. dynamin is a protein complex that oligomerizes to form polymers which wrap helically around membrane tubes [Antonny et al., 2016; Roux et al., 2010; Shlomovitz et al., 2011]. Although there is clear evidence that dynamin undergoes a conformational change when it hydrolyses GTP, there is not yet a consensus on the exact method of fission [Roux, 2014; Kozlov, 1999, 2001; McDargh et al., 2016; McDargh and Deserno, 2018], although recent coarse-grained simulations have shed some light on the possible role of constriction and de-polymerisation [Pannuzzo et al., 2018]. It has been shown experimentally that, upon hydrolysis of GTP, dynamin (counter)rotates rapidly whilst constricting [Roux et al., 2006]. The rotation frequency can be of order 10Hz [Roux et al., 2006], giving a mechanism for the generation of flows in the azimuthal direction.

Another possible way of driving such flows is by pulling a small tube from a Giant Unilamellar Vesicle (GUV) or cell with magnetic tweezers and using magnetic field oscillations to spin an attached bead [Crick and Hughes, 1950; Hosu et al., 2007; Monticelli et al., 2016].

3.2 Covariant fluid dynamics of membranes

The membrane behaves as a viscous fluid with 2D viscosity η_m. The ratio of this viscosity over the viscosity of the bulk aqueous fluid, η, gives a length scale, $L_{SD} = \frac{\eta_m}{\eta}$, called the Saffman-Delbrück length [Saffman and Delbruck, 1975; Saffman, 1976; Henle and Levine, 2010]. This is the distance over which bulk hydrodynamics screens membrane flows in planar geometry. In the case of a membrane tube, the screening length is modified due to geometric effects and becomes $\sqrt{L_{\mathrm{SD}} r_0}$ [Henle and Levine, 2010]. We will consider dynamics on a scale less than this, such that the dominant dissipation mechanism involves the membrane flows. This means that we can neglect

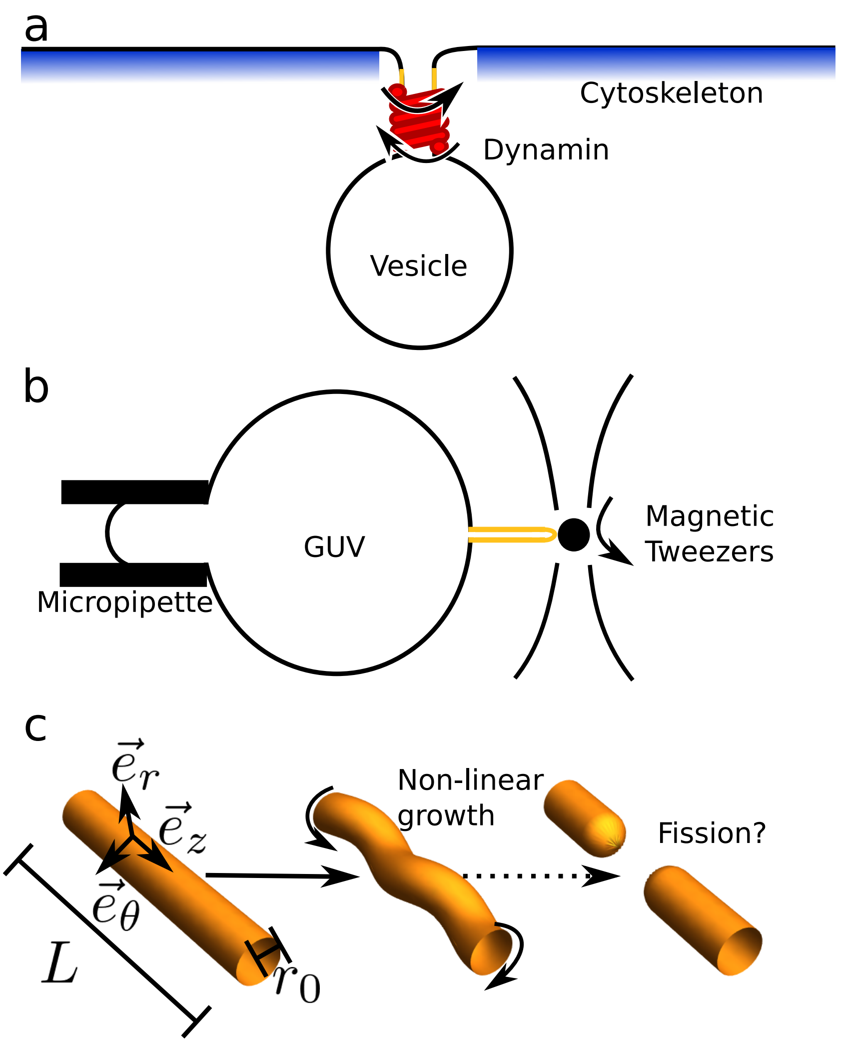

Figure 3.1: Possible realizations of shear driven instabilities on membrane tubes (shown in orange throughout). a) dynamin on the neck of a budding vesicle. Under hydrolysis of GTP the protein constricts and (counter)rotates, prior to fission of the tube. This rotation drives a significant shear flow on the neck of the vesicle. b) A GUV with membrane tube pulled by magnetic tweezers; the magnetic bead can be spun in order to drive flows in the azimuthal direction on the tube. c) Sketch of the growth of the helical instability described in this letter, the final stage is a possible pathway to tube fission due to non-linear effects. The basis vectors on the membrane $\vec{e}_i$ where $i = r, \theta, z$, length of tube, L, and equilibrium radius, r_0, are labelled. Middle panel shows shear direction.

bulk flows on sufficiently short length-scales (sufficiently short tubes), so long as we match to physically appropriate conditions at the tube ends. Such approaches have been used to great effect in understanding membrane dynamics on scales shorter than the screening length [Morris and Turner, 2015; Morris, 2017; Bahmani et al., 2016]. For further details see Appendix B.

We need to construct force balance and mass conservation equations on a moving membrane which we will denote by a 2D Riemannian manifold $\mathcal{S}$. As $\mathcal{S}$ will be embedded in $\mathbb{R}^3$ we denote vector fields living in $\mathbb{R}^3$ with an arrow above them, for example $\vec{x}$, and vector fields living in the tangent bundle of $\mathcal{S}$ by bold typeface, e.g. $\boldsymbol{x}$.

The position of $\mathcal{S}$ will be denoted by $\vec{X}(x_1, x_2)$, which depends locally on two coordinates of $\mathbb{R}^3$. This allows for the definition of a basis on $\mathcal{S}$, $\vec{e}_i = \partial_i \vec{X}$. The surface has velocity, $\vec{V} = \boldsymbol{v} + w\vec{n}$ where $\boldsymbol{v} = v^i \vec{e}_i$. $\mathcal{S}$ is equipped with a metric $\mathrm{d}s^2 = g_{ij}\mathrm{d}x^i\mathrm{d}x^j$, where $g_{ij} = \vec{e}_i \cdot \vec{e}_j$, this and its inverse act to raise and lower indices respectively (the action by the metric of raising and lower of indices will sometimes be denoted by the $\sharp$ and $\flat$ signs respectively, see Appendix B). The triad $(\vec{e}_1, \vec{e}_2, \vec{n} = \frac{\vec{e}_1 \times \vec{e}_2}{|\vec{e}_1 \times \vec{e}_2|})$ forms a local frame on $\mathcal{S}$. We also denote the second fundamental form on $\mathcal{S}$ as $\mathrm{d}B = b_{ij}\mathrm{d}x^i\mathrm{d}x^j$ where $b_{ij} = \vec{n} \cdot (\partial_j \vec{e}_i)$. The connections along the tangent and normal bundles are defined in the following way

$$\partial_i \vec{e}_j = C^k{}_{ij}\vec{e}_k; \quad \partial_i \vec{n} = -b_i{}^j \vec{e}_j \tag{3.1}$$

where $C^i{}_{jk} = \frac{1}{2} g^{im}\left(\partial_j g_{mk} + \partial_k g_{jm} - \partial_m g_{jk}\right)$ are Christoffel symbols [Frankel, 2011]. We will also define the mean curvature, H, and Gaussian curvature, K, in the following manner

$$2H = b_i{}^i; \quad K = \det\left(b_i{}^j\right). \tag{3.2}$$

We assume the membrane behaves like a zero-Reynolds number fluid in the tangential direction [Happel and Brenner, 1983] and has bending energy given by the usual Helfrich energy [Helfrich, 1973].

Formally, the rate-of-deformation tensor for a manifold is defined as the Lie-Derivative of the metric along the velocity field ($\vec{V} = \boldsymbol{v} + w\vec{n}$), which can be shown to be equal to [Marsden and Hughes, 1994; Arroyo and DeSimone, 2009]

$$d = \mathcal{L}_{\vec{V}}\left(g\right) = \frac{1}{2}\left(\boldsymbol{\nabla}\boldsymbol{v}^\flat + \left(\boldsymbol{\nabla}\boldsymbol{v}^\flat\right)^T\right) - bw \tag{3.3}$$

where $\boldsymbol{\nabla}$ is the covariant derivative and $\flat$ denotes the action of the metric to "lower" the index. The first two terms are covariant versions of the standard rate-of-deformation tensor, whereas the third term describes the coupling between curvature, b, and the velocity normal to the membrane, w. See Appendix B for a brief heuristic derivation of this using local constructions.

We can find the continuity equation (incompressibility condition) for the membrane by taking the trace of the rate-of-deformation tensor, d. This gives

$$\boldsymbol{\nabla} \cdot \boldsymbol{v} = 2Hw, \tag{3.4}$$

which is simply the Euclidean continuity equation modified to account for the normal motion of the membrane.

The membrane also has associated curvature energies given by the Helfrich energy [Helfrich, 1973]

$$E_{\mathrm{Hel}} = \int_{\mathcal{S}} \mathrm{d}A_{\mathcal{S}} 2\kappa H^2 \tag{3.5}$$

the time derivative of which is given by [Rahimi et al., 2013]

$$\partial_t E_{\mathrm{Hel}} = \dot{E}[w] = \int_{\mathcal{S}} w \left(\kappa \left[-2\Delta_{\mathrm{LB}} H + 4H \left(H^2 - K\right)\right]\right) \mathrm{d}A_{\mathcal{S}} \tag{3.6}$$

and depends only on the normal component of the flow field, not the tangential components. Here κ is the bending rigidity of the membrane and $\Delta_{\mathrm{LB}} = - \star \boldsymbol{d} \star \boldsymbol{d}$ is the Laplace-Beltrami operator (where $\star$ is the Hodge star and $\boldsymbol{d}$ is the exterior derivative, for definitions of these see Appendix B).

Defining the Rayleigh dissipation functional for the membrane in the following way

$$W_{\mathcal{S}} = \int_{\mathcal{S}} \eta_m d : d \mathrm{d}A_{\mathcal{S}} \tag{3.7}$$

describes the fluid behaviour of the membrane by accounting for the energy dissipation in the fluid due to the viscosity. From this a complete dissipation functional for the system can be defined as

$$G = W_{\mathcal{S}} + \dot{E} + \int_{\mathcal{S}} \sigma \left(\boldsymbol{\nabla} \cdot \boldsymbol{v} - 2Hw\right) \mathrm{d}A_{\mathcal{S}} \tag{3.8}$$

imposing incompressibility of membrane with Lagrange multiplier, σ, which corresponds to surface tension. Performing functional variation with respect to the components of the surface velocity yields the force balance equations for the membrane, see Ref. [Arroyo and DeSimone, 2009] for details.

Force balance normal to the membrane means the normal elastic and viscous forces must sum to zero, leading to the following

$$\kappa \left[2\Delta_{\mathrm{LB}} H - 4H \left(H^2 - K\right)\right] + 2\sigma H + 2\eta_m \left[b^i{}_j \nabla_i v^j - 2\left(2H^2 - K\right) w\right] = 0. \tag{3.9}$$

This is a modified form of the shape equation first derived by Zhong-Can & Helfrich

[Zhong-Can and Helfrich, 1989], but with the addition of viscous normal forces given by fluid flow on the membrane. The term coupling the second fundamental form and gradients in tangential velocity can be thought of as the normal force induced by fluid flowing over an intrinsically curved manifold. This term is of fundamental importance in the present study as it drives a shape instability. The other viscous term $\sim \left(2H^2 - K\right) w$ is the dissipative force associated with the normal velocity, inducing flows in the tangential direction on a curved surface.

Force balance in the tangential direction gives

$$\eta_m \left[\Delta_{\mathrm{LB}} v^i - 2Kv^i + 2\left(b^{ij} - 2Hg^{ij}\right)\nabla_j w\right] - \nabla^i \sigma = 0 \tag{3.10}$$

which is the modified form of the 2D Stokes equations. The new terms, coupling Gaussian curvature with tangential velocity, and curvature components with the gradients in normal velocity, come from the modified form of the rate-of-deformation tensor which accounts for the curved and changing geometry of the membrane. The term $\sim Kv^i$ describes the convergence/divergence of streamlines on a curved surface. The term $\sim \left(b^{ij} - 2Hg^{ij}\right)\nabla_j w$ describes the forces induced tangentially by the dynamics of the membrane.

3.3 The shear-driven instability of membrane tubes

We consider a ground-state membrane tube ($w = 0$) of length L in cylindrical coordinates (r, θ, z) with radius $r_0 = \sqrt{\frac{\kappa}{2\sigma_0}}$ and impose a velocity $v = v_0 \vec{e}_\theta$ at $z = 0$ (which can be interpreted as the edge of an active dynamin ring, for example). Making use of the azimuthal symmetry the continuity and Stokes equations reduce to an ODE that admits the solution

$$\boldsymbol{v}^{(0)} = \left(v_0 - \Omega z\right)\vec{e}_\theta \tag{3.11}$$

where the exact value of Ω depends on the boundary condition at $z = L$.

We consider a problem of a membrane tube attached to a flat membrane at $z = L$ where $L \ll \sqrt{L_{\mathrm{SD}} r_0}$. We treat this flat membrane as an effective "impedance" acting at the end of the tube, as such we do not balance the shape equations at $z = L$.

We may want to consider a tube attached to a sheet of membrane that has some friction associated to some underlying molecular interactions. For example, consider that the tube has been pulled from the plasma membrane which is attached to the acto-myosin network [Kaksonen and Roux, 2018]. We model this using D'arcy's equation on the sheet

$$\frac{1}{r}\partial_r\left(r\partial_r v\right)-\frac{v}{r^2}-\frac{\lambda}{\eta_m}v=0 \tag{3.12}$$

where λ is a friction coefficient associated with the adhesions and v is the velocity in the θ direction on the sheet (in standard planar polar coordinates). The solution to this equation is of the form $v = AK_1\left(\sqrt{\frac{\lambda}{\eta_m}}r\right)$, where $K_i(x)$ is a modified Bessel equation of the second kind of order i. We solve both geometries for some velocity v_L and then balance torques to find the ground-state velocity of the tube.

This leads a velocity profile on the tube (where the flow just follows the standard Stokes equations) of the form Eq. (3.11) where $\Omega = \frac{v_0\sqrt{\frac{\lambda}{\eta_m}}\frac{K_2}{K_1}}{1+L\sqrt{\frac{\lambda}{\eta_m}}\frac{K_2}{K_1}}$ where $K_i = K_i\left(\sqrt{\frac{\lambda}{\eta_m}}r_0\right)$.

In the limit $\lambda \to 0$ we recover the solution with no friction, where $\Omega = \frac{2v_0}{2L+r_0}$. In both of this and the $\lambda \to \infty$ limit the shear rate is of a similar order of magnitude, scaling like $\Omega \sim v_0/L$.

We can now make a perturbation about this ground state in $r(z,\theta,t) = r_0 + u(\theta,z,t)$, $\boldsymbol{v} = \boldsymbol{v}^{(0)} + \delta v^\theta(\theta,z,t)\vec{e}_\theta + \delta v^z(\theta,z,t)\vec{e}_z$, $\sigma = \sigma_0 + \delta\sigma(\theta,z,t)$ and $w = \partial_t u$. Note that all components of differential forms are given in the basis $\mathrm{d}\theta$, $\mathrm{d}z$ hence the different dimensions in components. We will also make use of the discrete Fourier transform, $f(\theta,z,t) = \sum_{q,m}\bar{f}_{q,m}(t)e^{iqz+im\theta}$, where $\bar{f}_{q,m}$ is the discrete Fourier Transform of $f(\theta,z)$ with $m \in \mathbb{Z}$. We will use this to write Eqs. (3.4), (3.9), (3.10) in Fourier space up to linear order in the perturbations.

To linear order the metric and its inverse on the membrane are

$$[g_{ij}] = \begin{bmatrix} r_0^2 + 2r_0 u & 0 \\ 0 & 1 \end{bmatrix}; \qquad g^{-1} = [g^{ij}] = \begin{bmatrix} \frac{1}{r_0^2} - \frac{2u}{r_0^3} & 0 \\ 0 & 1 \end{bmatrix} \tag{3.13}$$

The second fundamental form (and its mixed index version) are given by the following at linear order

$$[b_{ij}] = \begin{bmatrix} \partial_\theta^2 u - r_0 - u & \partial_{z\theta}u \\ \partial_{z\theta}u & \partial_z^2 u \end{bmatrix}; \quad [b_i{}^j] = \begin{bmatrix} \frac{\partial_\theta^2 u}{r_0^2} - \frac{1}{r_0} - \frac{u}{r_0^2} & \frac{\partial_{z\theta}u}{r_0^2} \\ \partial_{z\theta}u & \partial_z^2 u \end{bmatrix}; \tag{3.14}$$

which gives mean and Gaussian curvature

$$\begin{aligned} 2H = b_i{}^i = b_{ij}g^{ji} &= \frac{\partial_\theta^2 u}{r_0^2} - \frac{1}{r_0} + \frac{u}{r_0^2} + \partial_z^2 u \\ K = \det\left(b_i^j\right) = \det\left(b_{ik}g^{kj}\right) &= -\frac{\partial_z^2 u}{r_0} \end{aligned} . \tag{3.15}$$

The Christoffel symbols are the following

$$C^\theta{}_{ij} = \begin{bmatrix} \frac{\partial_\theta u}{r_0} & \frac{\partial_z u}{r_0} \\ \frac{\partial_z u}{r_0} & 0 \end{bmatrix}; \qquad C^z{}_{ij} = \begin{bmatrix} -r_0\partial_z u & 0 \\ 0 & 0 \end{bmatrix} \tag{3.16}$$

which can be used to find the covariant derivative of the velocity field on the membrane $\boldsymbol{v} = (v + \delta v^\theta)\vec{e}_\theta + \delta v^z \vec{e}_z$

$$\boldsymbol{\nabla v} = \begin{bmatrix} \frac{1}{r_0}\partial_\theta \delta v^\theta & \partial_\theta \delta v^z \\ -\frac{\Omega}{r_0} + \frac{1}{r_0}\partial_z \delta v^\theta & \partial_z \delta v^z \end{bmatrix}. \tag{3.17}$$

We will make use of this to calculate the viscous part of the normal membrane response in the shape equation

$$b^\sharp : \boldsymbol{\nabla v} = -\frac{1}{r_0^2}\partial_\theta \delta v^\theta - \frac{\Omega}{r_0}\partial_{z\theta} u. \tag{3.18}$$

We also note here the Hodge duals of the fundamental forms as this provides a natural way to compute Laplacians on manifolds (see Appendix B for general expressions of Hodge stars)

$$\begin{aligned} &\star\,\mathrm{vol}^2 = 1; && \star 1 = \mathrm{vol}^2 \\ &\star\,\mathrm{d}\theta = \left(\frac{1}{r_0} - \frac{u}{r_0^2}\right)\mathrm{d}z && \star\,\mathrm{d}z = -(r_0 + u)\mathrm{d}\theta \end{aligned} \tag{3.19}$$

where vol^2 is the volume 2-form on the surface. From this we find the Laplacian of the mean curvature $-\star \boldsymbol{d} \star \boldsymbol{d}H$ in order to derive the bending rigidity dominated response. After some lengthy algebra and taking the Fourier representation $u = \sum_{q,m} \bar{u}_{q,m} e^{iqz+im\theta}$ with similar transforms for $\sigma = \sigma_0 + \delta\sigma$ and the surface velocity components, we can write the shape equation as a linear response theory. This gives the linear response of the normal force balance is the following

$$\mathcal{F}^u_{q,m}\bar{u}_{q,m} + \mathcal{F}^\sigma_{q,m}\bar{\delta\sigma}_{q,m} + \mathcal{F}^\theta_{q,m}\bar{\delta v^\theta}_{q,m} + \mathcal{F}^z_{q,m}\bar{\delta v^z}_{q,m} + \mathcal{G}_{q,m}\bar{\delta w}_{q,m} = 0 \tag{3.20}$$

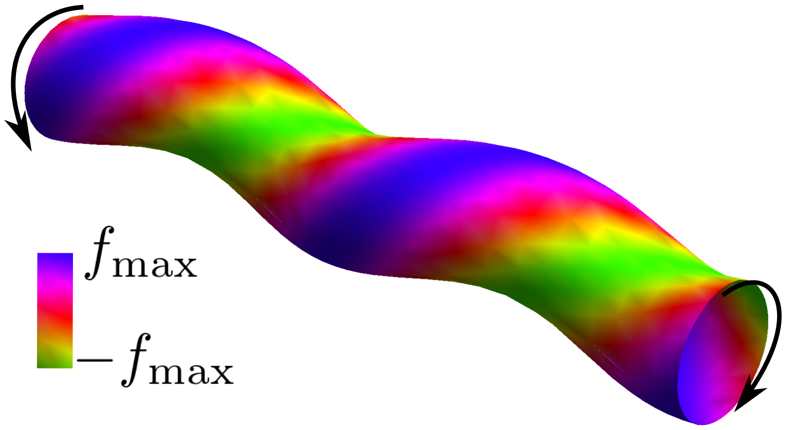

Figure 3.2: Surface plot showing the normal component of the viscous force per unit area on the $m = 1$, $\tilde{q} = 1$ mode according to Eq. (3.20). This shows the helical nature of this growth rate. $f_{\max}$ is the maximum force per unit area which scales with the size of the undulation. Arrows indicate the direction of shear flow.

where $\mathcal{F}^u_{q,m} = \frac{4\sigma_0^2}{\kappa}\left[\tilde{q}^4 + m^4 + 2\tilde{q}^2 m^2 - 2m^2 + 1\right] - \frac{2\eta_m m\tilde{q}\Omega}{r_0^2}$, $\mathcal{F}^\sigma_{q,m} = \frac{1}{r_0}$, $\mathcal{F}^\theta_{q,m} = \frac{2im\eta_m}{r_0^2}$, $\mathcal{F}^z_{q,m} = 0$ and $\mathcal{G}_{q,m} = \frac{2\eta_m}{r_0^2}$ where $\tilde{q} = qr_0$ is the dimensionless form of the wavenumber q, scaled by the tube radius.

Note the sign of the final term in the $\mathcal{F}^u_{q,m}$ coefficient suggests that the shear flow could lead to an instability in the $m \neq 0$ modes. The force distribution on the tube is shown in Fig. 3.2. Note that the ($m \to -m$, $\tilde{q} \to -\tilde{q}$) symmetry of the force defines a “handedness” which changes upon reversing the direction of the shear rate.

In order to find the 2D Stokes equations to linear order we need to calculate the Laplace-Beltrami operator of the velocity field $\boldsymbol{v} = \frac{(v_0(z) + \delta v^\theta)}{r(\theta,z)}\left(\frac{\partial}{\partial\theta}\right) + \delta v^z\left(\frac{\partial}{\partial z}\right)$. First we lower the velocity with the metric and act on it with the exterior derivative giving (to linear order)

$$\boldsymbol{d}\boldsymbol{v}^\flat = \left[-r_0\Omega + \partial_z u v_0 - u\Omega + r_0\partial_z\delta v^\theta\right]\mathrm{d}z \wedge \mathrm{d}\theta + \partial_\theta \delta v^z \mathrm{d}\theta \wedge \mathrm{d}z \tag{3.21}$$

next, taking the Hodge star of this and using the asymmetry of the wedge product and the fact that $\mathrm{vol} = \sqrt{|g|}\mathrm{d}\theta \wedge \mathrm{d}z$ we find

$$\star\,\boldsymbol{d}\boldsymbol{v}^\flat = \Omega - \frac{\partial_z u}{r_0}v_0 - \partial_z\delta v^\theta + \frac{\partial_\theta\delta v^z}{r_0}. \tag{3.22}$$

Taking the exterior derivative of this gives

$$\begin{aligned}\boldsymbol{d}\star\boldsymbol{d}\boldsymbol{v}^\flat = &\left[-\frac{\partial_{zz}uv_0}{r_0} - \partial_{zz}\delta v^\theta + \frac{\partial_{z\theta}\delta v^z}{r_0} - \frac{\partial_z u\Omega}{r_0}\right]\mathrm{d}z \\ &+\left[-\frac{\partial_{z\theta}u}{r_0}v_0 - \partial_{z\theta}\delta v^\theta + \frac{\partial_{\theta\theta}\delta v^z}{r_0}\right]\mathrm{d}\theta\end{aligned} \tag{3.23}$$

taking the Hodge star of this and applying the inverse metric leads to

$$\begin{aligned}\left(-\star\boldsymbol{d}\star\boldsymbol{d}\boldsymbol{v}^\flat\right)^\sharp = &\frac{1}{r_0^2}\left[-\partial_{zz}uv_0 - r_0\partial_{zz}\delta v^\theta + \partial_{z\theta}\delta v^z - \partial_z u\Omega\right]\left(\frac{\partial}{\partial\theta}\right) \\ &+\left[\frac{\partial_{z\theta}uv_0}{r_0^2} + \frac{1}{r_0}\partial_{z\theta}\delta v^\theta - \frac{1}{r_0^2}\partial_{\theta\theta}\delta v^z\right]\left(\frac{\partial}{\partial z}\right).\end{aligned} \tag{3.24}$$

The contribution to the Stokes equations from the Gaussian curvature is given by

$$-2K\boldsymbol{v} = \frac{2\partial_z^2 u}{r_0^2}v_0\left(\frac{\partial}{\partial\theta}\right) \tag{3.25}$$

and from the gradient in the normal velocity we have

$$2(b-2Hg)\cdot\boldsymbol{\nabla}w = 2\left[\begin{pmatrix}-\frac{1}{r_0^3} & 0\\ 0 & 0\end{pmatrix} + \frac{1}{r_0}\begin{pmatrix}\frac{1}{r_0^2} & 0\\ 0 & 1\end{pmatrix}\right]\begin{pmatrix}\frac{\partial_\theta w}{r_0}\\ \partial_z w\end{pmatrix} = \frac{2}{r_0}\partial_z w\left(\frac{\partial}{\partial z}\right). \tag{3.26}$$

Taking Fourier transforms of these we can find the 2D Stokes equations in Fourier space

$$\begin{aligned}&\begin{pmatrix}\eta_m\left[-\frac{m\tilde{q}}{r_0^2}\bar{\delta v}^z_{q,m} - \frac{i\tilde{q}\Omega}{r_0^2}\bar{u}_{q,m} + \frac{\tilde{q}^2}{r_0^2}\bar{\delta v}^\theta_{q,m} - \frac{1}{r_0^3}\bar{v}_0\circledast\left[\tilde{q}^2\bar{u}_{q,m}\right]\right] - \frac{im}{r_0}\bar{\delta\sigma}_{q,m}\\ \eta_m\left[\frac{m^2}{r_0^2}\bar{\delta v}^z_{q,m} - \frac{1}{r_0^3}\bar{v}_0\circledast\left[m\tilde{q}\bar{u}_{q,m}\right] - \frac{m\tilde{q}}{r_0^2}\bar{\delta v}^\theta_{q,m} + \frac{2i\tilde{q}}{r_0^2}\bar{\delta w}_{q,m}\right] - \frac{i\tilde{q}}{r_0}\bar{\delta\sigma}_{q,m}\end{pmatrix}\\ &\qquad = \begin{pmatrix}0\\0\end{pmatrix}\end{aligned} \tag{3.27}$$

where $\circledast$ denotes convolution between the two Fourier transforms in q space. This comes from using the convolution theorem $\mathbb{F}(f\cdot g) = \mathbb{F}(f)\circledast\mathbb{F}(g)$. The continuity equation reads

$$im\bar{\delta v}^\theta_{q,m} + i\tilde{q}\bar{\delta v}^z_{q,m} + \bar{\delta w}_{q,m} = 0. \tag{3.28}$$

From this point it is just a matter of algebra to find the response functions $\bar{\delta v}^\theta_{q,m}$, $\bar{\delta v}^z_{q,m}$ and $\bar{\delta\sigma}_{q,m}$ in terms of $\bar{u}_{q,m}$ and $\bar{\delta w}_{q,m}$.

$$\bar{\delta v}^{\theta}_{q,m} = \frac{im\left(m^2+3\tilde{q}^2\right)\bar{\delta w}_{q,m} + i\tilde{\Omega}\tilde{q}^3\bar{u}_{q,m} + \frac{\tilde{q}^2}{r_0}\bar{v_0}\circledast\left(\tilde{q}^2\bar{u}_{q,m}\right) - \frac{m\tilde{q}}{r_0}\bar{v_0}\circledast\left(m\tilde{q}\bar{u}_{q,m}\right)}{\left(m^2+\tilde{q}^2\right)^2} \tag{3.29}$$

$$\bar{\delta v}^{z}_{q,m} = \frac{i\tilde{q}\left(\left(\tilde{q}^2-m^2\right)\bar{\delta w}_{q,m} - m\tilde{q}\Omega\bar{u}_{q,m}\right) + \frac{m^2}{r_0}\bar{v_0}\circledast\left(m\tilde{q}\bar{u}_{q,m}\right) - \frac{m\tilde{q}}{r_0}\bar{v_0}\circledast\left(\tilde{q}^2\bar{u}_{q,m}\right)}{\left(m^2+\tilde{q}^2\right)^2} \tag{3.30}$$

$$\bar{\delta\sigma}_{q,m} = \frac{\eta_m\left[\frac{im}{r_0}\bar{v_0}\circledast\left(\tilde{q}^2\bar{u}_{q,m}\right) + \frac{i\tilde{q}}{r_0}\bar{v_0}\circledast\left(\tilde{q}m\bar{u}_{q,m}\right) + 2\tilde{q}^2\bar{\delta w}_{q,m} - m\tilde{q}\Omega\bar{u}_{q,m}\right]}{\left(m^2+\tilde{q}^2\right)r_0}. \tag{3.31}$$

We can now make use of the fact that the Fourier transform of the ground-state velocity convolved with some function is given by $\bar{v_0}\circledast(\cdot) = v_0 - i\Omega r_0\partial_{\tilde{q}}(\cdot)$. Thus we have the following identity

$$\bar{v_0}\circledast\left[f(\tilde{q})\bar{u}_{q,m}\right] = f(\tilde{q})\,\bar{v_0}\circledast\left(\bar{u}_{q,m}\right) - i\Omega r_0\bar{u}_{q,m}\partial_{\tilde{q}}f(\tilde{q}) \tag{3.32}$$

Writing $\bar{\delta w}_{q,m} = \partial_t\bar{u}_{q,m} + \mathcal{O}(u^2)$ we can find a growth rate equation for $\bar{u}_{q,m}$, where time is normalised according to $t = \tilde{t}\tau$ with $\tau = \frac{\eta_m}{\sigma_0}$,

$$\partial_{\tilde{t}}\bar{u}_{q,m} = -im\tilde{v}_0\bar{u}_{q,m} - \tilde{\Omega}m\partial_{\tilde{q}}\bar{u}_{q,m} + F(q,m)\bar{u}_{q,m} \tag{3.33}$$

where

$$F(q,m) = \frac{\left[m\tilde{q}\left(\left(m^2+\tilde{q}^2\right)^2 - 2\tilde{q}^2\right)\tilde{\Omega} - \left(m^2+\tilde{q}^2\right)^2\left(1+m^4+\tilde{q}^4+2m^2\left(\tilde{q}^2-1\right)\right)\right]}{2\tilde{q}^4}, \tag{3.34}$$

$\tilde{\Omega} = \frac{\eta_m\Omega}{\sigma_0}$ is the dimensionless shear rate and $\tilde{v}_0 = v_0\eta_m/(r_0\sigma_0)$.

The modes become unstable when the real part of the growth rate changes sign to $\Re\{F(m,q)\} > 0$. We note that $\Re\{F(0,q)\} < 0$ for all $\tilde{q}$, meaning that the $m = 0$ peristaltic mode is always linearly stable. The general stability condition is given by

$$\tilde{\Omega}m\tilde{q} > \frac{\left(m^2+\tilde{q}^2\right)^2\left(1+m^4+\tilde{q}^4+2m^2\left(\tilde{q}^2-1\right)\right)}{\left(\left(m^2+\tilde{q}^2\right)^2 - 2\tilde{q}^2\right)}. \tag{3.35}$$

The $|m| = 1$ mode is the first to be driven unstable. The stability diagram for the $|m| = 1$ mode is plotted in Fig. 3.4 with the black line in both the main figure and the inset. This means that, beyond a certain rotation speed, a helical mode will grow, with pitch length initially set by the length of the tube. The divergence of the growth rate for small $\tilde{q}$ is removed by the bulk hydrodynamics, however this is at a length scale much longer than the tube length. This helical instability is a new type of membrane instability, distinct from the usual peristaltic (Pearling) instabilities found in membrane tubes [Nelson et al., 1995].

This analysis neglects the advection in $\tilde{q}$ given by Eq. (3.33). This corresponds to the $m \neq 0$ modes being advected with the ground-state flow and adding more turns to the helices, thus increasing $\tilde{q}$. As this advection will eventually stabilise the mode, what really matters is the maximum size the fluctuation reaches before it is damped. To calculate this we solve Eq. (3.33) with the initial condition $\bar{u}_{q,1} = u_0 \delta(q - q_0)$, which can then be used to calculate the amplification of a given mode, $\frac{\bar{u}_{q,1}}{u_0}$. The solution to Eq. (3.33) is given by the method of characteristics as

$$\bar{u}_{q,m}(t) = u_0 \delta(\tilde{q} - \tilde{q}_0 - m\tilde{\Omega}\tilde{t}) e^{f(q,m)} \tag{3.36}$$

where

$$\begin{aligned} f(q,m) = \frac{1}{60}\Bigg[& - 20m^2(2 + 3\tilde{q}^2)\tilde{t}^3\tilde{\Omega}^2 + 30m^3\tilde{q}\tilde{t}^4\tilde{\Omega}^3 - 6m^4\tilde{t}^5\tilde{\Omega}^4 \\ & - 30\tilde{t}(5 + 4\tilde{q}^2 + \tilde{q}^4 - \tilde{q}\tilde{\Omega}) + 15m\tilde{t}\left(- 4\frac{iv_0\eta_m}{r_0\sigma_0} + t(8\tilde{q} + 4\tilde{q}^3 - \tilde{\Omega})\tilde{\Omega} \right) \\ & - \frac{60}{m\tilde{q}\tilde{\Omega} - m^2\tilde{t}\tilde{\Omega}^2} + \frac{15}{m}\left(\frac{4}{\tilde{q}\tilde{\Omega}} - \tilde{q}^{-2} + \frac{1}{(\tilde{q} - m\tilde{t}\tilde{\Omega})^2} \right)\Bigg]. \end{aligned} \tag{3.37}$$

and includes the advection of the undulation by the ground-state flow, thus shortening the wavelength of the undulation, i.e. $\tilde{q} = \tilde{q}(\tilde{t}) = \tilde{q}_0 + m\tilde{\Omega}\tilde{t}$. Because of this advection any $\tilde{q}$ mode which is initially unstable will be advected to stability and the mode will eventually decay. If our system was purely deterministic this would kill the instability in the long time limit, however as the bending rigidity of the membrane has comparable energy to the thermal energy ($\kappa \sim 10k_BT$ where k_B is Boltzmann's constant and T is the temperature) the $\tilde{q}$ spectrum is constantly fed by thermal fluctuations. This means that, to understand the full dynamics of the system we should solve Eq. (3.33) with the addition of a stochastic term describing thermal noise.

3.3.1 Solution to the fluctuation spectrum with thermal noise

Adding a thermal noise term to Eq. (3.33) we get a Stochastic Partial Differential Equation (SPDE) in $(\tilde{t}, \tilde{q})$ given by

$$\partial_{\tilde{t}} \bar{u}_{q,m} = -\tilde{\Omega} m \partial_{\tilde{q}} \bar{u}_{q,m} + F'(q,m) \bar{u}_{q,m} + \partial_{\tilde{t}} \zeta_{t,q,m} \tag{3.38}$$

where

$$\langle \partial_{\tilde{t}} \zeta_{t,q,m} \partial_{\tilde{t}'} \zeta_{t',q',m'} \rangle = \frac{2k_B T}{\kappa} \frac{\left(m^2 + \tilde{q}^2\right)^2}{2\tilde{q}^4} \delta_{q,q'} \delta_{m,m'} \delta\left(\tilde{t} - \tilde{t}'\right) \tag{3.39}$$

is chosen such that we recover the equipartition result of equilibrium statistical mechanics when $\tilde{\Omega} = \tilde{v}_0 = 0$. We define $F'(q,m) = F(q,m) - im\tilde{v}_0$. Eq. (3.38), with initial data $\bar{u}_{q,m}(0) = u_0(q,m)$, is the stochastic version of a Cauchy problem [Chow, 2014].

In order to solve this SPDE we make use of the method of Stochastic Characteristics [Chow, 2014]. In Itô form the thermal noise is written as

$$\zeta_{t,q,m} = \sqrt{B(\tilde{q},m)} \mathrm{d}W_{t,q,m} \tag{3.40}$$

where $\langle \mathrm{d}W_{t,q,m} \mathrm{d}W_{t',q',m'} \rangle = \delta_{m,m'} \delta_{q,q'} \mathrm{d}t$ and $B(\tilde{q},m) = \left(m^2 + \tilde{q}^2\right)^2 / \tilde{q}^4$.

Eq. (3.38) is equivalent to the Itô integral

$$\bar{u}_{q,m}(\tilde{t}) = u_0(\tilde{q},m) - m\tilde{\Omega} \int_0^{\tilde{t}} \partial_{\tilde{q}} \bar{u}_{q,m}(s) \mathrm{d}s + \int_0^{\tilde{t}} \left[F'(q,m) \bar{u}_{q,m}(s) \mathrm{d}s + \zeta_{s,q,m}\right]. \tag{3.41}$$

In order to solve this we introduce the following characteristics

$$\begin{aligned} \phi_t(q) &= \tilde{q} + m\tilde{\Omega} \int_0^{\tilde{t}} \mathrm{d}s = \tilde{q} + m\tilde{\Omega}\tilde{t} \\ \eta_t(q,r) &= r + \int_0^{\tilde{t}} \eta_s\left(q,r\right) F'\left(\phi_s(q),m\right) \mathrm{d}s + \int_0^{\tilde{t}} \sqrt{B(\phi_s(q),m)} \mathrm{d}W_{t,m,q} \end{aligned} \tag{3.42}$$

for certain regularity conditions on the noise these stochastic integral equations have a unique solution that defines a stochastic flow of diffeomorphism. This leads to the solution to the stochastic Cauchy problem, posed by Eq. (3.38) and its initial data, which is given by

$$\begin{aligned} \bar{u}_{q,m} =& u_0\left(\phi_t^{-1}(q), m\right) \exp\left[\int_0^{\tilde{t}} F'(\phi_s(y),m) \mathrm{d}s\right] |_{y=\phi_t^{-1}(q)} \\ &+ \int_0^{\tilde{t}} \exp\left[\int_\tau^{\tilde{t}} F'(\phi_s(y),m) \mathrm{d}s\right] \sqrt{B(\phi_\tau(y),m)} \mathrm{d}W_\tau |_{y=\phi_t^{-1}(q)}. \end{aligned} \tag{3.43}$$

Evaluating the integrals in the exponentials we find

$$\begin{aligned}
f'(q,m,t) &= \int F'(\phi_t(y),m)\mathrm{d}t \\
&= \Bigg[-15m^5\Omega(mt\Omega+q) - 40m^2(mt\Omega+q)^6 \\
&+ 60m\left(m^2-1\right)\Omega(mt\Omega+q)^3\log(mt\Omega+q) - 30\left(6m^4-2m^2+1\right)(mt\Omega+q)^4 \\
&+ 10m^4\left(m^2-1\right)^2 + 60\left(2m^6-2m^4+m^2\right)(mt\Omega+q)^2 - 6(mt\Omega+q)^8 \\
&+ 15m\Omega(mt\Omega+q)^5\Bigg]\Bigg(60m\Omega(mt\Omega+q)^3\Bigg)^{-1} - im\tilde{v}_0 t \\
&= f(q,m,t) - im\tilde{v}_0 t.
\end{aligned} \tag{3.44}$$

We want to consider the steady state of the fluctuations at a time when any dependence on this initial data has decayed so, by taking the complex conjugate of Eq. (3.43) squared and averaging we find

$$\langle|\bar{u}_{q,m}|^2(\tilde{t})\rangle = e^{2f(\tilde{q}-m\tilde{\Omega}\tilde{t},m,\tilde{t})}\int_0^{\tilde{t}} B\left(\tilde{q}+m\tilde{\Omega}\left(\tau'-\tilde{t}\right),m\right)e^{-2f(\tilde{q}-m\tilde{\Omega}\tilde{t},m,\tau')}\mathrm{d}\tau' \tag{3.45}$$

where we have input the characteristic curves and their inputs explicitly and neglected the term describing the dynamics of the initial data as we are only interested in the steady state.

If we consider the case of the $m = 1$ mode then the equilibrium fluctuations are known to be critical in the $\tilde{q} \to 0$ limit [Fournier and Galatola, 2007]. Because of this we introduce a cut of wavenumber $\tilde{q}_0$ that corresponds to the length-scale of the longest fluctuation on the finite tube. This implies that the noise kernel of our system has only localized support on the interval $\tau' - \tilde{t} \in [\frac{\tilde{q}_0-\tilde{q}}{\Omega}, 0]$, so we can change variables to integrate over this interval. Thus, the $m = 1$ steady state fluctuations are given by

$$\langle|\bar{u}_{q,1}|^2(0)\rangle = e^{2f(\tilde{q},1,0)}\int_{\frac{\tilde{q}_0-\tilde{q}}{\Omega}}^{0} B\left(\tilde{q}+\tilde{\Omega}\tau',1\right)e^{-2f(\tilde{q},1,\tau')}\mathrm{d}\tau'. \tag{3.46}$$

We plot the steady states of $\langle|\bar{u}_{q,1}|^2\rangle$ and the z component of their spatial gradients, $\tilde{q}^2\langle|\bar{u}_{q,1}|^2\rangle$, in Fig. 3.3 for $\tilde{\Omega} = 1$ and $\tilde{q}_0 = 0.2$. We also plot the equivalent

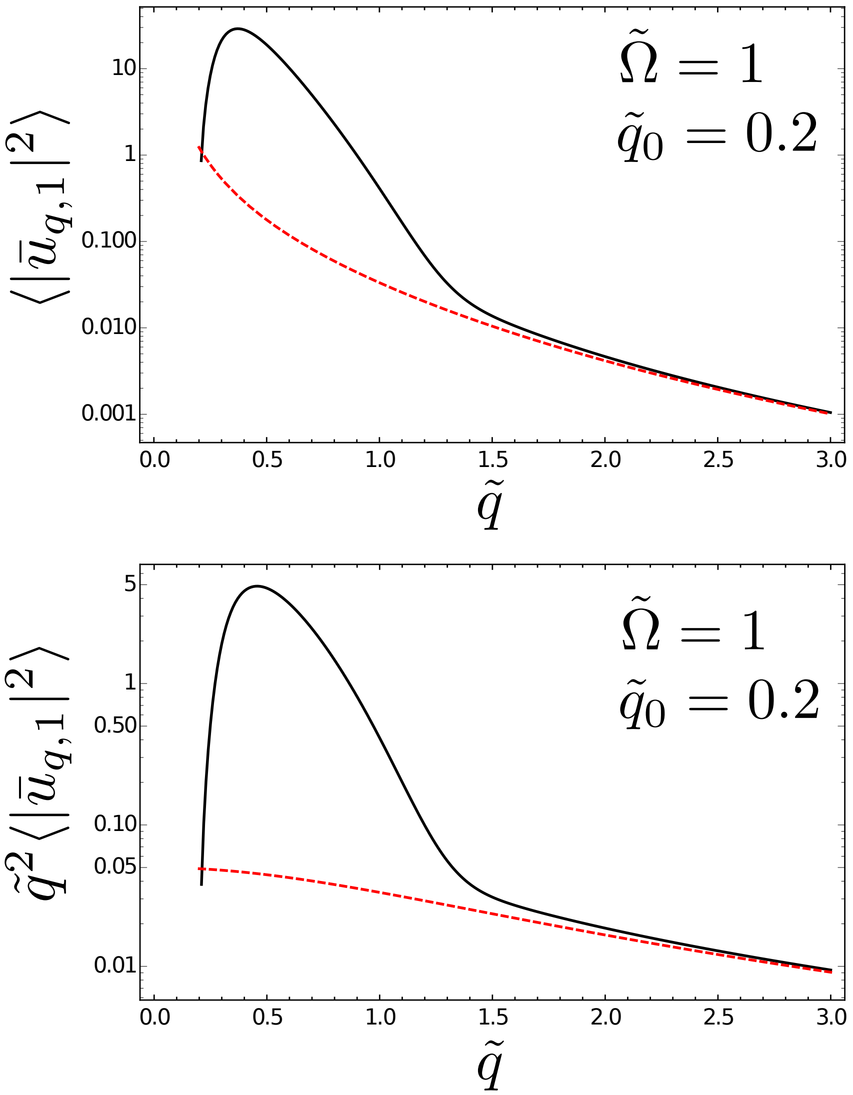

Figure 3.3: The steady state fluctuations for a sheared tube (Eq. (3.46)) and their Fourier "gradients" in the z direction ($|\mathbb{F}\left(\vec{e}_z \cdot \nabla u\right)|^2 = \tilde{q}^2\langle|\bar{u}_{q,1}|^2\rangle$) with shear rate, $\tilde{\Omega} = 1$, and long wavelength cut-off, $\tilde{q}_0 = 0.2$. We choose the bending rigidity to be $\kappa = 10k_BT$. The dashed red line shows the equivalent thermal fluctuations.

thermal fluctuations given by Eq. (1.30) with $m = 1$

$$\langle |\bar{u}_{q,1}|^2 \rangle = \frac{k_B T}{\kappa \tilde{q}^2 \left(\tilde{q}^2 + 2\right)}. \tag{3.47}$$

which we plot as a red dashed line.

In fact it is the gradient terms which break the linearisation conditions due to the advection and amplification increasing the gradients. To find a criterion for "Non-linear deformation" (and hence very large fluctuations), we can find where the gradients become of $\sim \mathcal{O}(1)$ by solving $(1 + \tilde{q}_{\max}^2)\langle |\bar{u}_{q,1}|^2 \rangle|_{\tilde{q} \to \tilde{q}_{\max}} = 1$ for $\tilde{\Omega}$ given $\tilde{q}_0$, where $\tilde{q}_{\max}$ is the $\tilde{q}$ value for the peak of the steady state fluctuations, Eq. (3.46). This gives us a line on the $(\tilde{q}_0, \tilde{\Omega})$ plane that gives a conservative estimate of when non-linear effects become important. A stability diagram for the $m = 1$ mode in $(\tilde{q}, \tilde{\Omega})$-space is plotted in Fig. 3.4 along with the criterion for non-linear deformation (blue dot-dashed).

3.4 Discussion

In the small $\tilde{q}$ limit, the threshold shear (Eq. (3.35)) is $\tilde{\Omega} \approx 2\tilde{q}$, see Appendix B. The shear rate is $\Omega \sim \frac{2\pi r_0 \nu}{L}$, where ν is the spinning frequency. Assuming that the cut-off wavenumber of the tube is associated with a fundamental mode $\tilde{q}_0 = \frac{2\pi r_0}{L}$, gives the critical spinning frequency for the onset of instability as

$$\nu_{\mathrm{crit}} \simeq \frac{2\sigma_0}{\eta_m} \tag{3.48}$$

The functional form of the critical frequency can be explained using a scaling analysis of Eq. (3.9). For $q \sim 1/L$, the first order correction to the curvature scales like $H \sim \frac{u}{L^2}$ so that the elastic force-per-unit-area scales like $f_{\mathrm{el}} \sim \frac{u\sigma_0}{L^2}$, while the off-diagonal components of the second fundamental form scale like $b \sim \frac{u}{r_0 L}$ and hence the viscous force-per-unit-area scale like $f_{\mathrm{vis}} \sim \frac{\eta_m \Omega u}{r_0 L} \sim \frac{u \eta_m \nu}{L^2}$. Balancing these forces gives a critical frequency $\nu_{\mathrm{crit}} \sim \frac{\sigma_0}{\eta_m}$.

Typical membranes in the fluid (liquid disordered) phase have viscosities $\eta_m \sim 10^{-8} - 10^{-7}\,\mathrm{Pa\,m\,s}$ [Hormel et al., 2014] (higher in the liquid ordered phase). However, much higher values have been associated with tubes pulled from living cells, $\eta_m \sim 10^{-7} - 10^{-5}\,\mathrm{Pa\,m\,s}$ [Brochard-Wyart et al., 2006]. Effective viscosities may be higher still if the neck is crowded with proteins. If we assume the surface tension takes a physiologically typical value of $\sigma_0 \sim 10^{-5}\,\mathrm{N\,m^{-1}}$ [Roux, 2014; Antonny et al., 2016], this gives a critical frequency of $\nu_{\mathrm{crit}} \sim 1 - 100\mathrm{Hz}$ in the small

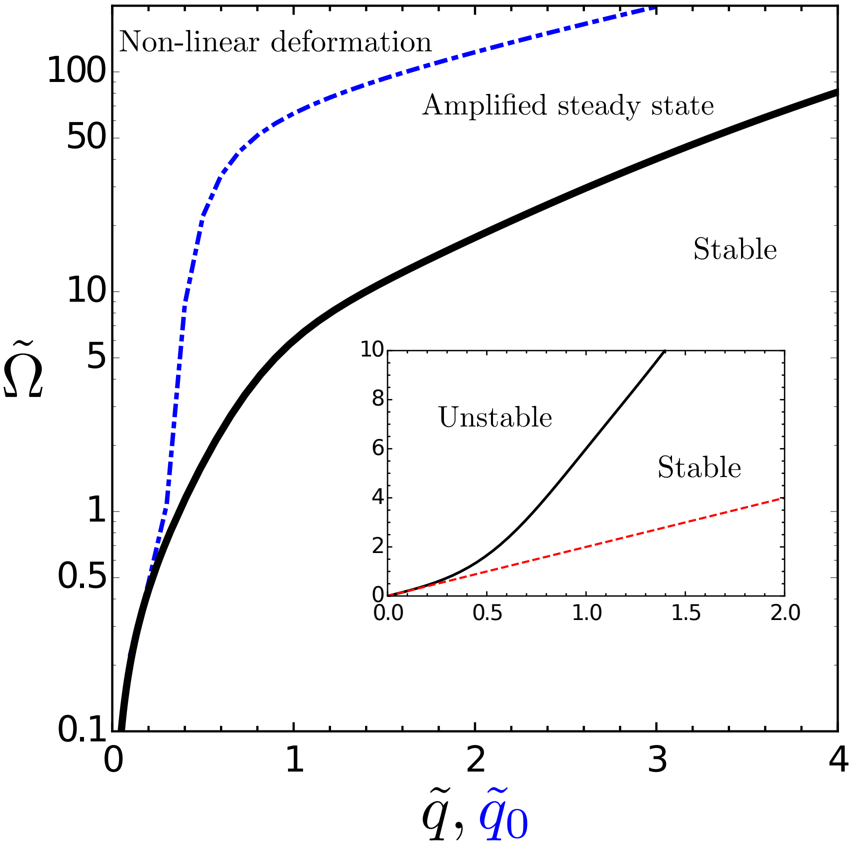

Figure 3.4: Figure showing the zero of $F(q, m = 1)$ as a function of $\tilde{q}$ and $\tilde{\Omega}$ (Eq. (3.35)). The region above the black line is unstable. The blue dot-dashed line shows the value of $\tilde{\Omega}$ for which the steady state becomes non-linear as a function of $\tilde{q}_0$, which we denote the region above this line as "Non-linear deformation". The inset shows the same plot on a linear scale, with the red dashed line showing the low $\tilde{q}$ expansion of the stability criterion.

$\tilde{q}$ limit. It is more likely that dynamin will be found on short tubes with $\tilde{q}_0 \sim 1$ so, reading off from Fig. 3.4 we find $\tilde{\Omega} \sim 5$ for the stability criterion and $\tilde{\Omega} \sim 50$ for the non-linearity criterion which corresponds to frequencies of $5 - 500$Hz and $50 - 5000$Hz. dynamin has been measured to have rotational frequencies $\nu \sim 10$Hz [Roux et al., 2006], suggesting the instability could be accessible to dynamin for the higher values of viscosity found in cells [Brochard-Wyart et al., 2006]. The criterion for non-linearity is rather conservative as it is based on the variance of the fluctuations (one third of the fluctuations will be breaking the linearity condition at this point). It is also likely to significantly underestimate the size of fluctuations, which, in the case of dynamin, are likely to be dominated by active processes rather than thermal noise (see Chapter 4), and is further damped by the hard cut-off at $\tilde{q}_0$.

A natural way for the instability/fluctuations to progress in the non-linear regime is fission of the tube, which is of particular significance given that the exact mechanism for dynamin mediated fission is unknown. This effect may be amplified due to friction with the cytoskeleton [Brochard-Wyart et al., 2006; Simunovic et al., 2017] impeding the supply of membrane to the growing fluctuations. As the instability/fluctuations grow the surface tension will increase, either narrowing the tube or causing Pearling [Nelson et al., 1995]. An increase in tension has been shown to accelerate spontaneous tube fission [Morlot et al., 2012] and friction impeding membrane flow has been shown experimentally to scission tubes [Simunovic et al., 2017]. The increase in fluctuations is also likely to promote the formation of hemi-fused states, which can be an important intermediate for fission [Pannuzzo et al., 2018]. This picture of fission, promoted by membrane hydrodynamics just outside the active dynamin site, is consistent with the experimental observation that the location of fission is near the edge of the active dynamin site rather than directly under it [Morlot et al., 2012]. The time-scale over which the instability grows is of the order of $\tau =\sim 10^{-2} - 1$ s, which is sufficiently fast to be consistent with the dynamin-induced fission process [Dar et al., 2015].

Although we have provided evidence that a membrane instability can be driven by the rotation of dynamin, our study is based on the simplified geometry of a cylindrical tube, rather than the neck of a budding vesicle, a location where dynamin might typically act *in-vivo*. While our approach becomes analytically intractable for such complex membrane geometries we can gain some intuition into how the driving force per unit area of the instability changes with the geometry of the neck region. We do this by considering the term in the normal force balance equation that is responsible for driving the instability. Given the helical symmetry of the instability we infer that this driving force-per-unit-area goes like the mixed derivative in the shape, $f_{\text{driving}} \sim \eta_m b^i{}_j \nabla_i v^j$. The term which acts like the shear rate on the tube now depends on z and we must calculate it numerically, see Appendix B. In the case of a catenoid neck this leads to an amplification of the driving force by (only) a factor of 2 near the active site ($z = 0$), for details see Appendix B. Whilst a relatively small effect, this is qualitatively consistent with the experimental observation that dynamin fission of a tube *in-vitro* often occurs near the GUV neck [Morlot et al., 2012] and that fission on the necks of a budding vesicles *in-vivo* occurs faster than it does on long tubes [Morlot et al., 2010; Roux, 2014]. It is worth noting that if we were to consider a model for dynamin which included constriction then we would need to be decide whether to use a constant velocity or constant torque boundary condition, as the two are no longer equivalent. The same would also apply when considering the full non-linear dynamics.

A second possibility for the non-linear growth is a stable non-equilibrium shape driven by the membrane flow. In this case it is worth noting an analogy between the membrane tube instability that we discuss here and elastic rods under torsion that deform nonlinearly into plectonemes [Audoly and Pomeau, 2010]. We suggest that it may also be possible (under some conditions) for the unstable membrane tube to develop *fluid* plectonemes, similar to those actually seen in experiments on long tubes covered in dynamin [Roux et al., 2006; Morlot et al., 2010].

A possible experiment to better understand the non-linear evolution of the fluctuations and determine whether these hydrodynamic effects alone are sufficient to induce fission would involve a short tube pulled from a GUV or cell by magnetic tweezers that then spin its end, Fig. 3.1b. This would also enable experimentalists to test our predictions more quantitatively. The instability should also arise in a longer tube, however the quantitative nature of our predictions would likely require modifications due to screening of membrane flow by the ambient fluid. In this case we expect that the unstable wavelength would then be set by the screening length $\sqrt{L_{\text{SD}} r_0}$ rather than the tube length [Henle and Levine, 2010; Ferziger and Peric, 2002] and that our results would continue to hold at the scaling level.

In summary, we have developed a hydrodynamic theory that predicts an instability on fluid membrane tubes that is driven purely by a shear in the membrane flow. Such flows are shown to first drive a helical instability, which is quite distinct from any previously identified instabilities of fluid membrane tubes. This instability, although eventually advected to stability by the flow is shown to be able to produce a significant increase in the fluctuation spectra of a membrane tube. We predict that this instability is physiologically accessible to dynamin but has not previously been considered in models of its function [Lenz et al., 2008; Morlot et al., 2010]. This instability may provide a mechanism for dynamin-mediated tube fission, e.g. due to increasing tension in the amplified steady state or in the subsequent non-linear deformation regime.

Chapter 4

Dynamics of Passive and Active Membrane Tubes

Utilising the Onsager formulation, we derive dynamical equations for the small deformation limit relaxation of a fluid membrane tube allowing for a contrast of ambient viscosity and variations in surface tension due to the deformations. Computing the relaxation rates, we recover results previously found in the case of purely axisymmetric perturbations along with new results for higher order angular (m) modes. We explain the long and short wavelength limits of these modes making use of various asymptotic arguments. Adding stochastic terms to our dynamical equations which describe passive thermal forces and "active" forces, we compute expressions for the mean-square fluctuations and effective temperature associated with the addition of active fluctuations. Finally we discuss how one might measure these fluctuations in experiment and infer the properties of the active forces.

4.1 Introduction

Membrane tubes, formed by bilayers of phospholipid molecules, are structures ubiquitous in cells. They are vital to the function of many organelles including the peripheral Endoplasmic Reticulum (ER) [Nixon-Abell et al., 2016] and membrane nanotubes, which have been implicated as an important pathway in inter-cellular signalling [Abounit and Zurzolo, 2012]. Membrane tubes can be formed from a flat membrane by the action of a local force normal to the membrane (such as molecular motors, actin or curved proteins coating the membrane) [Derényi et al., 2002; Cuvelier et al., 2005; Yamada et al., 2014].

From a statistical mechanics perspective there has been significant work on the thermal fluctuations of membrane tubes [Fournier and Galatola, 2007; Komura and Lipowsky, 1992]. A striking prediction from these theories is that the bending modes of the tube are critical in the long wavelength limit and it would be expected that an-harmonic terms in the free energy will dominate the excess area and length fluctuations [Fournier and Galatola, 2007]. This has become relevant recently as it was shown that optical tweezers techniques can be used to infer the power spectral density of such fluctuations on tubes pulled from Giant Uni-Lamelar Vesicles (GUVs) [Valentino et al., 2016]. A related topic of interest is the statistical mechanics of tubular networks [Tlusty and Safran, 2000; Tlusty et al., 2000] and on the length fluctuations of tubes held by a fixed force [Barbetta and Fournier, 2009].

Work on the dynamics of membrane tubes has focused on the simplified axisymmetric case, in particular the dynamics of the pearling instability of membrane tubes [Bar-Ziv and Moses, 1994; Boedec et al., 2014; Nelson et al., 1995; Gurin et al., 1996], and the dynamics of tether pulling from a GUV or cell [Evans and Yeung, 1994; Nassoy et al., 2008; Brochard-Wyart et al., 2006]. A further area of study is that of particle mobility laterally within the membrane [Henle and Levine, 2010; Rahimi et al., 2013]. These examples provide insight into how the curved geometry of the membrane tube can lead to interesting physics, in the form of visco-elastic couplings [Rahimi et al., 2013] and non-Newtonian rheological behaviour [Brochard-Wyart et al., 2006; Evans and Yeung, 1994].

In this chapter we will focus on the dynamics of membrane tubes, deriving equations of motion from an Onsager framework (in the manner of [Fournier, 2015; Sachin Krishnan et al., 2016, 2018]) and analysing the relaxation behaviour in Fourier space. We then consider the case where stochastic forces act on the membrane and derive the statistical behaviour of the shape undulations, in particular focusing on the case where active noise dominates. Here the term active refers to a noise term which breaks the fluctuation dissipation theorem. Such active membrane systems have been theoretically studied extensively in the case of flat membranes [Prost and Bruinsma, 1996; Ramaswamy et al., 2000; Gov, 2004] and spherical vesicles [Sachin Krishnan et al., 2018; Turlier et al., 2016]. These descriptions have also proved useful when compared to experiments with active proteins in GUVs [Manneville et al., 2001] and in the analysis of red blood cell flicker [Turlier et al., 2016; Gov and Safran, 2005].

We derive the fluctuation spectra for active tubes and calculate the effective temperature of such fluctuations. We then discuss possible ways to quantify the parameters in our active fluctuations model from experiment. Finally we discuss some open problems in the study of membrane tubes and the study of active membranes more generally.

4.2 Membrane tube dynamics

4.2.1 Geometry

We take the membrane to be a manifold, $\mathcal{S} \subset \mathbb{R}^3$. Vectors in the ambient space will be denoted $\vec{x} \in \mathbb{R}^3$ and vectors in the tangent bundle to the manifold as $\boldsymbol{x} \in \mathcal{T}(\mathcal{S})$.

We parametrise the manifold, $\mathcal{S}$, with the vector

$$\vec{r} = (r(\theta, z, t)\cos\theta, r(\theta, z, t)\sin\theta, z) \tag{4.1}$$

where $r(\theta, z, t) = r_0[1 + u(\theta, z, t)]$, see Fig. 4.1(a). We will consider the small deformation limit where $u \ll 1$. Tangent vectors can be induced on the surface by taking derivatives with respect to θ and z, giving $\vec{e}_\theta = \partial_\theta \vec{r}$ and $\vec{e}_z = \partial_z \vec{r}$, respectively. A complete triad can be defined by $\{\vec{e}_\theta, \vec{e}_z, \vec{n}\}$ where $\vec{n} = (\vec{e}_\theta \times \vec{e}_z)/|\vec{e}_\theta \times \vec{e}_z|$ is the normal vector to the surface. The metric and second fundamental (bilinear) forms are then defined as $g = g_{ij}\mathrm{d}X^i\mathrm{d}X^j = \vec{e}_i \cdot \vec{e}_j \mathrm{d}X^i\mathrm{d}X^j$ and $b = b_{ij}\mathrm{d}X^i\mathrm{d}X^j$ where $b_{ij} = \vec{n} \cdot \partial_j \vec{e}_i$. This can be used to define the mean curvature, $H = {b_i}^i/2$, and Gaussian curvature, $K = \det {b_i}^j$.

The membrane is assumed to behave as a fluid in the tangential direction so we define a vector field, $\boldsymbol{v} \in \Gamma(\mathcal{T}(\mathcal{S}))$, as the flow velocity of lipids in the membrane, where $\Gamma(\mathcal{T}(\mathcal{S}))$ denotes a section of the tangent bundle. We assume $\boldsymbol{v}$ is of the same order as u and perturb around a ground-state with no flow.

4.2.2 Free energy

The free energy of an incompressible fluid membrane can be written using the Helfrich-Canham-Willmore energy [Helfrich, 1973; Canham, 1970] (Eq. (1.8))

$$\mathcal{F}_{\mathrm{el}} = \int \mathrm{d}A\left[\sigma + \frac{\kappa}{2}(2H)^2\right], \tag{4.2}$$

where σ is surface tension, κ the bending rigidity and the area element is given by $\mathrm{d}A = \sqrt{|g|}\mathrm{d}\theta\mathrm{d}z$. We have integrated out the contribution from the Gaussian curvature and saddle splay modulus by assuming no changes in topology and a tube of infinite length. We also neglect spontaneous curvature for simplicity ($C_0 = 0$).

The area element and the mean curvature squared are given, up to second order by,

$$\mathrm{d}A \approx r_0 \left[1 + u + \frac{1}{2}\left(r_0^2 \partial_z^2 u + \partial_\theta^2 u\right)\right] \mathrm{d}\theta \mathrm{d}z, \tag{4.3}$$

$$H^2 \approx \frac{1}{r_0^2}\left[\frac{1}{2} - r_0^2 \partial_z^2 u + \partial_\theta^2 u + u + \frac{1}{2}\Big\{2u(r_0^2\partial_z^2 u + 3\partial_\theta^2 u) - r_0^2(\partial_z u)^2 \right.$$
$$\left. + (r_0^2\partial_z^2 u + \partial_\theta u)^2 + (\partial_\theta u)^2 + 3u^2\Big\}\right]. \tag{4.4}$$

If we take the full free energy $\mathcal{F} = \mathcal{F}_{\mathrm{el}} - \int \mathrm{d}V\,\Delta P$, where $\Delta P = P^- - P^+$ is the the hydrostatic pressure jump across the membrane, then the ground-state $r = r_0$ must satisfy the modified Laplace equation

$$\frac{\sigma}{r_0} - \frac{\kappa}{2r_0^3} - \Delta P = 0, \tag{4.5}$$

in order to minimise the free energy.

For the Onsager formulation of membrane dynamics, we need to know the rate of change of the free energy. This is given by

$$\dot{\mathcal{F}} = \int \mathrm{d}\theta \mathrm{d}z \left[\frac{\kappa}{r_0^2}\Big(\frac{3}{2}u + r_0^2\partial_z^2 u + r_0^4\partial_z^4 u + \frac{5}{2}\partial_\theta^2 u + 2r_0^2\partial_\theta^2\partial_z^2 u + \partial_\theta^4 u\Big)\right.$$
$$\left. - \sigma(u + r_0^2\partial_z^2 u + \partial_\theta^2 u)\right] r_0 \dot{u}, \tag{4.6}$$

where dot indicates time derivative and we have made use of Eq. (4.5) (or equivalently the constraint that total volume is preserved $\int \mathrm{d}\theta \mathrm{d}z\, u = -(1/2)\int \mathrm{d}\theta \mathrm{d}z\, u^2$). Note that $\dot{\mathcal{F}}$ is a functional only of the normal velocity $v_n = r_0\dot{u} + \mathcal{O}(u^2)$ and not the tangential components of membrane velocity, $\boldsymbol{v}$.

4.2.3 Dissipation and constraints

We will consider only the dissipation due to the ambient fluid as this is the dominant dissipative mechanism at large length-scales [Seifert and Langer, 1994]. We define the velocity in the ambient fluid as $\vec{V} = V^\alpha \vec{e}_\alpha$ where we use Greek indices to denote summation over coordinates in $\mathbb{R}^3$. The dissipation functional for the bulk fluid is given by [Landau and Lifshitz, 1959]

$$\mathcal{P}^\pm = \int_{\mathcal{V}^\pm} \mathrm{d}V^\pm\, \eta^\pm D^\pm_{\alpha\beta} D^{\alpha\beta\pm}, \tag{4.7}$$

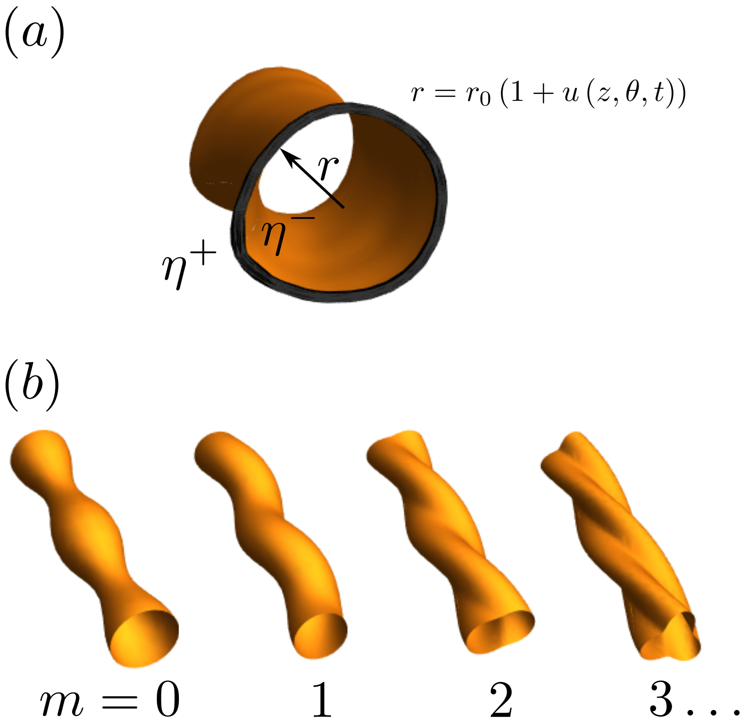

Figure 4.1: (a) Cross section of a membrane tube with some undulation $r_0 u(\theta, z, t)$ about the radius r_0. Here $\eta^{\pm}$ label the viscosity of the exterior and interior ambient fluid respectively. (b) Surface plots of the Fourier decompositions, $u = \sum_{q,m} u_{qm} e^{iqz+im\theta}$ for $q = 1$.

where $\eta^{\pm}$ is the viscosity of the exterior and interior regions respectively (and similarly for the other ± superscripts), as shown in Fig. 4.1(a), and $D^{\pm}_{\alpha\beta} = (\nabla_\alpha V^{\pm}_{\beta} + \nabla_\beta V^{\pm}_{\alpha})/2$ is the rate-of-deformation tensor.

At the scale of cell membranes (10 nm–100 μm) viscous dissipation dominates the energy dissipation in the fluid, hence we neglect the contribution from inertia and assume zero Reynolds number [Happel and Brenner, 1983].

Our system has several constraints which, in the Onsager formulation, will be imposed using Lagrange multipliers [Doi, 2013]. Firstly, the membrane and ambient fluid are incompressible so must satisfy the following conditions

$$\nabla_\alpha V^{\alpha\pm} = 0, \tag{4.8}$$

for the bulk fluid (where ± correspond to the exterior and interior velocities respectively) and

$$\nabla_i v^i - 2 v_n H = 0, \tag{4.9}$$

for the membrane, where $v_n = r_0 \dot{u} + \mathcal{O}(u^2)$ is the normal velocity of the surface. Further constrains come in the form of no slip and no permeation boundary conditions on the bulk fluid at the membrane

$$(V^{\alpha\pm}|_{r_0})^i = v^i, \qquad V^{r\pm}|_{r_0} = r_0 \dot{u}. \tag{4.10}$$

4.2.4 Rayleighian and equations of motion

To derive the full equations of motion using the Onsager formulation, we must first write down the Rayleighian or Rayleigh dissipation functional [Doi, 2011; Goldstein, 2002; Landau and Lifshitz, 1959; Fournier, 2015; Sachin Krishnan et al., 2016]. The full Rayleighian for the system is found by taking the sum of the rate-of-change of free energy for the system, Eq. (4.6), and the energy dissipations (half the work done on the system), Eq. (4.7), and adding in the constraints on the system using Lagrange multipliers. This formulation is equivalent to Onsager's kinetic equation with reciprocal coefficients, but recast as a variational formalism, with the advantage that finding the correct pairs of fluxes and forces is now trivial as they are obtained by the variational principle automatically [Onsager, 1931a,b; Doi, 2011]. Thus our

Rayleighian reads

$$
\begin{aligned}
\mathcal{R} =& \mathcal{P}^{+} + \mathcal{P}^{-} + \dot{\mathcal{F}} + \int_{\partial\mathcal{V}} \mathrm{d}A\, \zeta(\nabla_i v^i + \dot{u}) - \int_{\mathcal{V}^{+}} \mathrm{d}V^{+}\, P^{+} \nabla_\alpha V^{\alpha +} \\
& - \int_{\mathcal{V}^{-}} \mathrm{d}V^{-}\, P^{-} \nabla_\alpha V^{\alpha -} + \int_{\partial\mathcal{V}} \mathrm{d}A \Big[\mu_i^{+} \left[(V^{\alpha +}|_{r_0})^i - v^i \right] + \mu_i^{-} \left[(V^{\alpha -}|_{r_0})^i - v^i \right] \\
& + \lambda^{+} \left(V^{r+}|_{r_0} - r_0 \dot{u} \right) + \lambda^{-} \left(V^{r-}|_{r_0} - r_0 \dot{u} \right) \Big], \qquad (4.11)
\end{aligned}
$$

where ζ, $P^{\pm}$, $\mu_i^{\pm}$ and $\lambda^{\pm}$ are Lagrange multipliers imposing the constraints of constant area, constant volume, no slip and no permeation respectively. Note that we choose the signs of ζ and $P^{\pm}$ so that they correspond to pressure and surface tension variation respectively (however this is arbitrary).

We now proceed to use Onsager's principle and minimise the Rayleighian to find the equations of motion for the membrane [Doi, 2013]. Taking variations of Eq. (4.11) with respect to $V^{\alpha\pm}|_{r_0}$ yields

$$
\begin{aligned}
\mp \eta^{\pm} D_{ri}^{\pm}|_{r_0} - \mu_i^{\pm} &= 0, \qquad (4.12) \\
\mp \eta^{\pm} D_{rr}^{\pm} \pm P^{\pm} - \lambda^{\pm} &= 0, \qquad (4.13)
\end{aligned}
$$

showing that $\mu_i^{\pm}$ and $\lambda^{\pm}$ correspond to the traction forces acting on the membrane.

Extremising with respect to v^i gives

$$
\nabla_i \zeta - \mu_i^{+} - \mu_i^{-} = 0, \qquad (4.14)
$$

or eliminating the Lagrange multipliers

$$
\nabla_i \zeta + \eta^{+} D_{ri}^{+} - \eta^{-} D_{ri}^{-} = 0, \qquad (4.15)
$$

which is simply tangential force balance on the membrane.

Taking variations with respect to $r_0 \dot{u}$ and eliminating $\lambda^{\pm}$ gives normal force balance on the membrane as

$$
\begin{aligned}
& \frac{\kappa}{r_0^3} \left(\frac{3}{2} u + r_0^2 \partial_z^2 u + r_0^4 \partial_z^4 u + \frac{5}{2} \partial_\theta^2 u + 2 r_0^2 \partial_\theta^2 \partial_z^2 u + \partial_\theta^4 u \right) \\
& - \frac{\sigma}{r_0} (u + r_0^2 \partial_z^2 u + \partial_\theta^2 u) + \frac{\zeta}{r_0} - \eta^{+} D_{rr}^{+} + P^{+} + \eta^{-} D_{rr}^{-} - P^{-} = 0. \qquad (4.16)
\end{aligned}
$$

Varying with respect to ζ gives the membrane incompressibility condition, Eq. (4.9).

Varying with respect to $P^{\pm}$ and $V_\alpha^{\pm}$ gives the usual Stokes equations and incompressibility condition

$$\eta^{\pm}\nabla^2 V^{\alpha\pm} = \nabla^{\alpha} P^{\pm}, \qquad \nabla_{\alpha} V^{\alpha\pm} = 0. \tag{4.17}$$

This approach has allowed us to derive the fully coupled equations of motion for the system by just considering the relevant dissipation functionals and system constraints and deriving everything from a variational principle.

4.2.5 Fourier space decomposition

Next we solve the bulk fluid dynamics equations and thus calculate their traction forces on the membrane. To do this we make use of the known solution to the Stokes equations in cylindrical coordinates given by [Happel and Brenner, 1983]

$$\vec{V}^{\pm} = \nabla\phi^{\pm} + \nabla \times \left(\psi^{\pm}\vec{e}_z\right) + r\partial_r \nabla\xi^{\pm} + \partial_z \xi^{\pm}\vec{e}_z, \tag{4.18}$$

$$P^{\pm} = -2\eta^{\pm}\partial_z^2 \xi^{\pm}, \tag{4.19}$$

where $(\phi^{\pm}, \psi^{\pm}, \xi^{\pm})$ are scalar functions that each satisfy the Laplace equation. We decompose these functions in Fourier space in θ and z in terms of the coordinate systems harmonic basis

$$\begin{pmatrix} \phi^{\pm} \\ \psi^{\pm} \\ \xi^{\pm} \end{pmatrix} = \sum_{q,m} \begin{pmatrix} \Phi^{\pm}_{qm} \\ \Psi^{\pm}_{qm} \\ \Xi^{\pm}_{qm} \end{pmatrix} \Pi^{\pm}_{qm}(r) e^{iqz+im\theta}, \tag{4.20}$$

with

$$\Pi^{\pm}_{qm}(r) = \begin{cases} \Pi^{+}_{qm}(r) = K_m(qr), \\ \Pi^{-}_{qm}(r) = I_m(qr), \end{cases} \tag{4.21}$$

where $I_m(qr)$ and $K_m(qr)$ are modified Bessel functions of the first and second kind, respectively.

We now take the Fourier transform of our equations where we define the Fourier transform as $f(\theta, z) = \sum_{q,m} f_{qm} e^{iqz+im\theta}$, the form of surfaces given by the m mode perturbations is shown in Fig. 4.1(b).

Applying the boundary conditions on the bulk flow in Fourier space allows us to find $(\Phi^{\pm}_{qm}, \Psi^{\pm}_{qm}, \Xi^{\pm}_{qm})$ in terms of our variables $(v^{\theta}, v^{z}, \dot{u})$. The boundary conditions in Fourier space read

$$\begin{pmatrix} r_0\dot{u}_{qm} \\ v^{\theta}_{qm} \\ v^{z}_{qm} \end{pmatrix} =$$

$$\left.\begin{pmatrix} \Phi^{\pm}_{qm}\partial_r\Pi^{\pm}_{qm} + (im/r)\Psi^{\pm}_{qm}\Pi^{\pm}_{qm} + \Xi^{\pm}_{qm}\partial_r^2\Pi^{\pm}_{qm} \\ (im/r)\Phi^{\pm}_{qm}\Pi^{\pm}_{qm} - \Psi^{\pm}_{qm}\partial_r\Pi^{\pm}_{qm} + im\Xi^{\pm}_{qm}\left[\partial_r\Pi^{\pm}_{qm} - \Pi^{\pm}_{qm}/r\right] \\ iq\Phi^{\pm}_{qm}\Pi^{\pm}_{qm} + irq\Xi^{\pm}_{qm}\left[\partial_r\Pi^{\pm}_{qm} + \Pi^{\pm}_{qm}/r\right] \end{pmatrix}\right|_{r=r_0}. \tag{4.22}$$

We can make use of the continuity equation to eliminate $v^{\theta}_{qm} = r_0(qv^{z}_{qm} - i\dot{u}_{qm})/m$ and find $(\Phi^{\pm}_{qm}, \Psi^{\pm}_{qm}, \Xi^{\pm}_{qm})$ in terms of $\dot{u}_{qm}$ and v^{z}_{qm}, which are given in Appendix C.

In Fourier space, the components of the tangential force balance equation read

$$\begin{aligned} \theta: \quad & \frac{im}{r_0}\zeta_{qm} + \eta^{+}\left.\left[r\partial_r(V^{\theta+}_{qm}/r) + \frac{im}{r}V^{r+}_{qm}\right]\right|_{r=r_0} \\ & - \eta^{-}\left.\left[r\partial_r(V^{\theta-}_{qm}/r) + \frac{im}{r}V^{r-}_{qm}\right]\right|_{r=r_0} = 0, \end{aligned} \tag{4.23}$$

$$\begin{aligned} z: \quad & iq\zeta_{qm} + \eta^{+}\left(iqV^{r+}_{qm} + \partial_r V^{z+}_{qm}\right)\big|_{r=r_0} \\ & - \eta^{-}\left(iqV^{r-}_{qm} + \partial_r V^{z-}_{qm}\right)\big|_{r=r_0} = 0 \end{aligned} \tag{4.24}$$

where the bulk velocity terms can be expressed using using $(\Phi^{\pm}_{qm}, \Psi^{\pm}_{qm}, \Xi^{\pm}_{qm})$ and are thus just functions of $\dot{u}_{qm}$ and v^{z}_{qm}. Solving for v^{z}_{qm} and ζ_{qm} allows us to write $(\Phi^{\pm}_{qm}, \Psi^{\pm}_{qm}, \Xi^{\pm}_{qm})$ in terms of $\dot{u}_{qm}$ alone. We can now write the normal force balance equation in Fourier space (in dimensionless units) as

$$B\dot{u}_{qm} = -Au_{qm}, \tag{4.25}$$

where

$$A(\tilde{q}, m) = \left(\tilde{q}^2 + m^2\right)^2 - \frac{1}{2}\tilde{q}^2 - \frac{5}{2}m^2 + \frac{3}{2} - \tilde{\sigma}\left(1 - \tilde{q}^2 - m^2\right), \tag{4.26}$$

$$B(\tilde{q}, m) = \frac{\frac{\zeta_{qm}}{r_0} + \left.\left(P^{+}_{qm} - \eta\left(\chi+1\right)\partial_r V^{r+}_{qm} + \eta\left(\chi-1\right)\partial_r V^{r-}_{qm} - P^{-}_{qm}\right)\right|_{r=r_0}}{\dot{u}_{qm}\kappa/r_0^3}, \tag{4.27}$$

where $\tilde{\sigma} = \sigma r_0^2/\kappa$, $\eta = \eta^+ + \eta^-$, $\chi = (\eta^+ - \eta^-)/\eta$ and $\tilde{q} = qr_0$.

The exact form of B is in general too complex to write down except for the $m = 0$ case where it is

$$B(\tilde{q}, 0) = \frac{\eta r_0^3}{\kappa}(1 + \tilde{q}^2)\left[\frac{(\chi - 1)\, I_1^2}{2\tilde{q}I_1I_0 - \tilde{q}^2\left(I_0^2 - I_1^2\right)} + \frac{(\chi + 1)\, K_1^2}{2\tilde{q}K_1K_2 - \tilde{q}^2\left(K_1^2 - K_0^2\right)}\right], \quad (4.28)$$

where the modified Bessel functions are evaluated at $r = r_0$. For larger values of m, we will evaluate B numerically using Mathematica.

It is interesting to note that, compared with the spherical case, there are more degrees of freedom for the tube as the m and $\tilde{q}$ modes are not coupled as they are in the case of spherical harmonics [Sachin Krishnan et al., 2016].

4.3 Relaxation dynamics

Here we will consider the relaxation dynamics for all the modes, in particular examining their asymptotic behaviour. We will make use of these results later when analysing the active fluctuations of a membrane tube in Sec. 4.5. As the relaxation dynamics are identical under a sign change of $\tilde{q}$ and m we restrict ourselves to $\tilde{q}, m \geq 0$ in our analysis and discussion.

For some initial condition at $t = 0$, the solution to Eq. (4.25) is given by $u_{qm}(t) = u_{qm}(0)e^{-\lambda t}$, where $\lambda = A/B$. In this section we will analyse the form of λ to understand the stability and relaxation dynamics of the Fourier modes in membrane tube's shape. The relaxation rate for each $(\tilde{q}, m)$ mode is given by λ. This describes the rate at which an undulation in the tube's radius decays back to the ground-state. These rates are plotted as a function of wave-number in the z direction, $\tilde{q}$, in Figs. 4.2 and 4.3. Throughout we will fix the total viscosity η and vary the relative viscosity $\chi = (\eta^+ - \eta^-)/\eta$ so the plots are shown in units of associated with the time-scale of the total viscosity given by $\tau = \eta r_0^3/\kappa$.

First, we discuss $m = 0$ modes. For values of $\sigma = \kappa/(2r_0^2)$, corresponding to an equilibrium ground-state with no net pressure, the undulations are always stable so $\lambda \geq 0$. The scaling behaviour of λ in the small $\tilde{q}$ regime ($\tilde{q} \ll 1$) is computed for the $m = 0$ mode, where we find

$$B(\tilde{q}, 0) \approx \frac{\eta r_0^3}{\kappa\tilde{q}^2}\left[2(\chi - 1) + \frac{\chi + 1}{2\log(2/\tilde{q}) - 1 - 2\gamma}\right], \quad (4.29)$$

where $\gamma = 0.577\ldots$ is the Euler-Mascheroni constant. This gives the scaling behaviour $\lambda \sim \tilde{q}^2$ in the small $\tilde{q}$ regime, see Fig. 4.2(a).

As would be expected, in the large $\tilde{q}$ limit the scaling behaviour is like that of a flat membrane where $\lambda \sim \tilde{q}^3$ and all relative viscosities converge to a universal relaxation rate (a consequence of the approximate symmetry between the interior and exterior at such small length scales), see Fig. 4.2(a).

The scaling behaviour for $m = 1$ is evaluated numerically and shown in Fig. 4.2(b). For large values of $\tilde{q}$ the relaxation rate scales like that of a flat membrane (for the same reason as the $m = 0$ modes). However, at small values of $\tilde{q}$, some interesting behaviour is encountered which is strongly dependent on the relative viscosity. As $\tilde{q} \to 0$, the external dissipation due to the tube being dragged through the fluid dominates the relaxation rate (the internal motion simply corresponds to locally translating the cross section of the tube so gradients in velocity, and hence dissipation, become small). In this limit the tube behaves like an elastic rod in terms of its relaxation and tends slowly towards $\lambda \sim -\left(\gamma + \log \tilde{q}\right) \tilde{q}^2$ in the long wavelength limit. This scaling behaviour for a continuous Zimm model of an elastic rod under tension in the long wavelength limit with small deflections is discussed in Appendix C.

The case $\chi = -1$ corresponds to $\eta^+ = 0$, hence in the long wavelength limit there is essentially no friction, and the $m = 1$ mode relaxation rate diverges as $\tilde{q} \to 0$. The crossover between interior to exterior dominant dissipation means that in the $\eta^+ \ll \eta^-$ limit, the relaxation rate can be non-monotonic in $\tilde{q}$, increasing at intermediate $\tilde{q}$ before being screened by the exterior viscosity at long wavelengths, as seen in the case $\chi = -0.95$ in Fig. 4.2(b).

For higher modes of $|m| \geq 2$, the dissipation is dominated in the long wavelength regime by the gradients in velocity induced by the cross sectional deformations of the tube. Thus, as $\tilde{q}$ decreases, the relaxation rate becomes constant, see Fig. 4.3. This constant increases with m as each successive mode costs more bending energy to excite, so will relax faster. The high $\tilde{q}$ limit again behaves like a flat membrane with $\lambda \sim \tilde{q}^3$ for all m.

4.4 Pearling instability

For the $m = 0$ mode, there is an instability when the tube is placed under high surface tension [Boedec et al., 2014]. The growth rate or dispersion relation of such

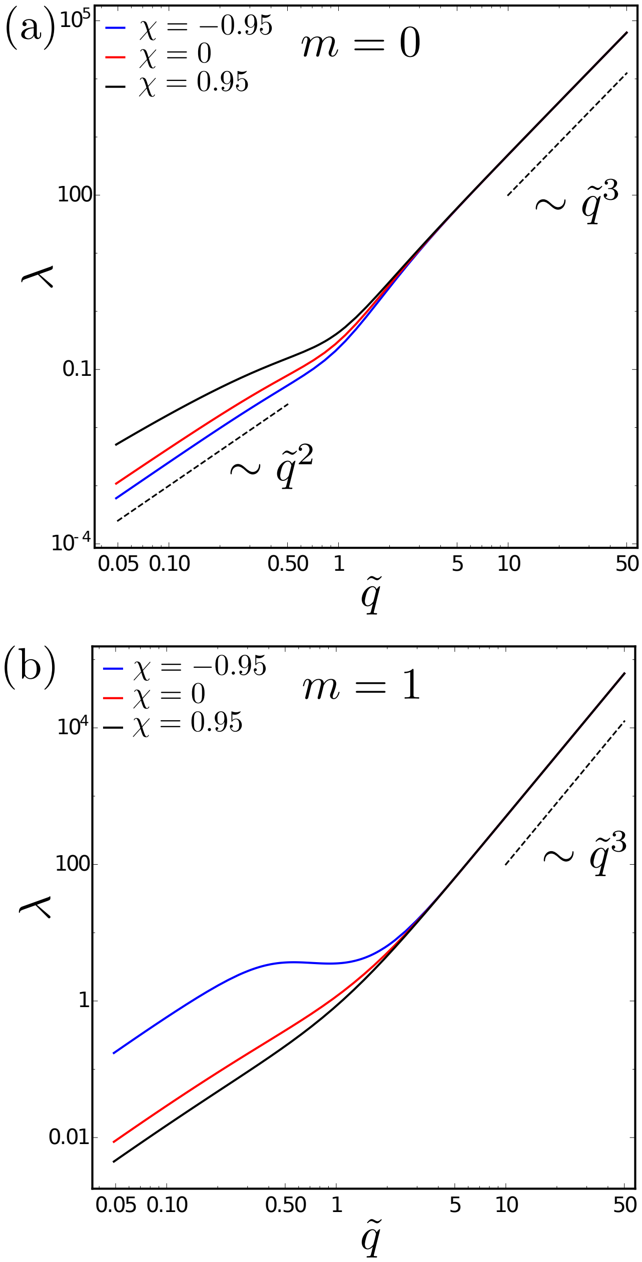

Figure 4.2: Plot of decay rate, λ, against wavenumber, $\tilde{q}$ for u_{qm} (a) $m = 0$ and (b) $m = 1$ for varying relative viscosity $\chi = (\eta^+ - \eta^-)/\eta$ (keeping η fixed as the rate λ has been non-dimensionalized by the viscous time associated with the total viscosity, $\tau = \eta r_0^3/\kappa$). Surface tension is given by $\tilde{\sigma} = 1/2$ such that the ground-state has no hydrostatic pressure jump.

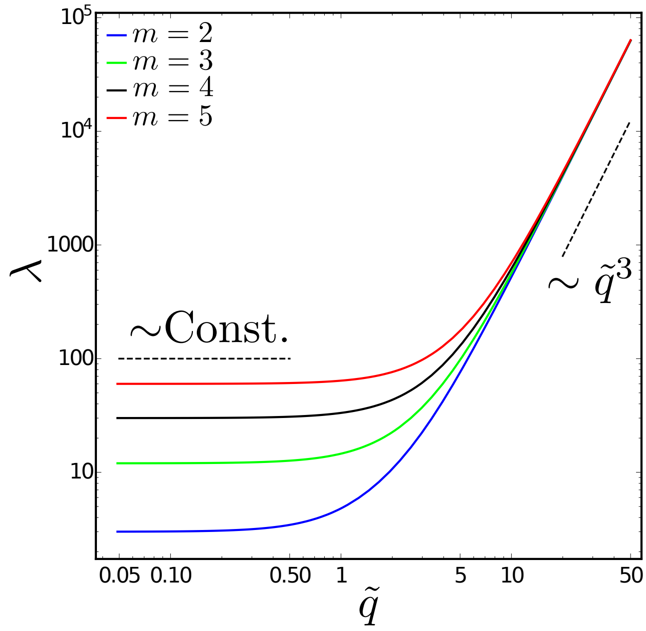

Figure 4.3: Plot of decay rate, λ, against wavenumber, $\tilde{q}$ for the modes u_{qm} ($m = 2, 3, 4, 5$) where λ has been non-dimensionalized by the viscous time, $\tau_\eta = \eta r_0^3/\kappa$). Surface tension is given by $\tilde{\sigma} = 1/2$ such that the ground-state has no hydrostatic pressure jump. Changing χ does not change the form of the relaxation rate for these modes.

an instability is given by

$$\begin{aligned} -\lambda &= -\frac{A(\tilde{q},0)}{B(\tilde{q},0)} \\ &= -\frac{\kappa\left[\tilde{q}^4 - \frac{1}{2}\tilde{q}^2 + \frac{3}{2} - \tilde{\sigma}(1-\tilde{q}^2)\right]}{\eta r_0^3(1+\tilde{q}^2)\left(\frac{(\chi-1)I_1^2}{2\tilde{q}I_1I_0 - \tilde{q}^2\left(I_0^2 - I_1^2\right)} + \frac{(\chi+1)K_1^2}{2\tilde{q}K_1K_2 - \tilde{q}^2\left(K_1^2 - K_0^2\right)}\right)}, \end{aligned} \tag{4.30}$$

where, again, the modified Bessel functions are evaluated at $r = r_0$. The threshold for the instability at $\tilde{q} = 0$ is given by $\tilde{\sigma} > 3/2$ or $\sigma > 3\kappa/(2r_0^2)$, which corresponds to the point when $A(0,0)$ changes sign [Nelson et al., 1995; Gurin et al., 1996].

This instability is analogous to the Rayleigh-Plateau instability in a column of fluid [Tomotika, 1935; Rayleigh, 1892], where forces arising from the interface surface tension, σ act to minimise the total interface area-to-volume ratio, and thus the fluid breaks up into spherical droplets. Similar forces arise in the case of membrane tubes although these are counteracted by the presence of membrane bending rigidity, κ. The exact form of this instability growth-rate was found previously in Ref. [Boedec et al., 2014], where only axisymmetric perturbations were considered,

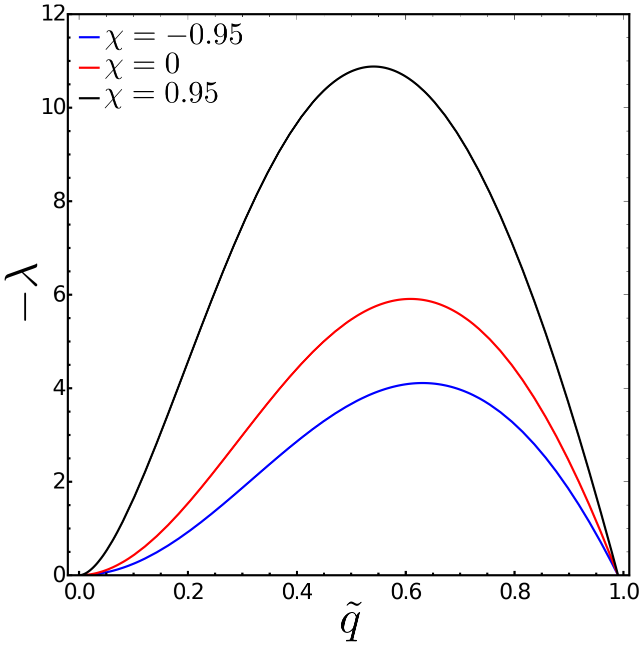

Figure 4.4: Plot of the growth rate for the pearling instability on a membrane tube, $-\lambda$, against wavenumber, $\tilde{q}$, for varying values of relative viscosity χ. The dimensionless surface tension is set to $\tilde{\sigma} = \sigma r_0^2/\kappa = 100$.

and was shown to converge with earlier works when variations in surface tension were neglected [Nelson et al., 1995; Gurin et al., 1996; Powers, 2010].

For large surface tension $\tilde{\sigma}$ and similar values of viscosity ($\chi \sim 0$), the maximum of the growth rate, $-\lambda$, rapidly converges to the wave-number $\tilde{q}^* \approx 0.6$. The growth rate, $-\lambda$, is plotted in Fig. 4.4 for different values of relative viscosity χ. Note that short wavelength perturbations, $\tilde{q} \geq 1$, are always stable as the surface tension terms in $A(\tilde{q}, 0)$ are always positive for $\tilde{q} \geq 1$.

4.5 Fluctuations of membrane tubes

We now consider the relaxation dynamics of the tube under thermal and active fluctuations, this is given by adding thermal and active forces to the force balance equation

$$B\dot{u}_{qm} = -Au_{qm} + \xi_{qm}^{\text{th}} + \xi_{qm}^{\text{ac}}, \tag{4.31}$$

where ξ^{th} and ξ^{ac} denote the passive and active forces respectively. The statistical properties of the thermal noise are given in the standard way

$$\langle \xi^{\mathrm{th}}_{qm}(t)\rangle = 0, \tag{4.32}$$

$$\langle \xi^{\mathrm{th}}_{qm}(t)\xi^{\mathrm{th}}_{q'm'}(t')\rangle = \frac{2k_{\mathrm{B}}T}{\kappa}B\delta_{qq'}\delta_{mm'}\delta(t-t'), \tag{4.33}$$

where k_B is Boltzmann's constant and T is the temperature. For the active fluctuations we write

$$\begin{aligned} &\langle \xi^{\mathrm{ac}}_{qm}(t)\rangle = 0, \\ &\langle \xi^{\mathrm{ac}}_{qm}(t)\xi^{\mathrm{ac}}_{q'm'}(t')\rangle = \frac{F(q,m)^2}{2}e^{-|t-t'|/\tau_*}\delta_{qq'}\delta_{mm'}, \end{aligned} \tag{4.34}$$

where τ_* is the correlation time of the active forces and the physics of the active processes will be captured in our choice of active force density, $F(q,m)$ [Gov, 2004]. These active fluctuations could have a variety of biological sources such cytoskeletal activity [Turlier et al., 2016] or ion pumps/transmembrane proteins [Ramaswamy et al., 2000]. We will consider only the simplest case where for direct forces acting on the membrane, $F(q,m) = F = \text{Const.}$, although in principle more realistic models could be considered and can depend in detail on the biological process being modelled [Turlier et al., 2016; Manneville et al., 2001].

4.5.1 Thermal fluctuations

First we consider the case when there are no active fluctuations, $\xi^{\mathrm{ac}}_{qm} = 0$. Solving Eq. (4.31) by Fourier transform in time (assuming any initial conditions have decayed away) yields the following covariance

$$\langle u_{qm}(t)\, u^*_{q'm'}(t')\rangle^{\mathrm{th}} = \frac{k_{\mathrm{B}}T}{\kappa A}e^{-|t-t'|A/B}\delta_{qq'}\delta_{mm'}, \tag{4.35}$$

and the equal time covariance is given by

$$\langle |u_{qm}|^2\rangle^{\mathrm{th}} = \frac{k_{\mathrm{B}}T}{\kappa\left[(\tilde{q}^2+m^2)^2 - \frac{1}{2}\tilde{q}^2 - \frac{5}{2}m^2 + \frac{3}{2} - \tilde{\sigma}(1-\tilde{q}^2-m^2)\right]}, \tag{4.36}$$

which is the standard result of the equipartition theorem [Fournier and Galatola, 2007], also given in Eq. (1.30). The equal time covariance is plotted against $\tilde{q}$ in Fig. 4.5 for $m = 0, 1, 2, 3$. Here the surface tension is chosen to be commensurate with the equilibrium tube radius with no hydrostatic pressure.

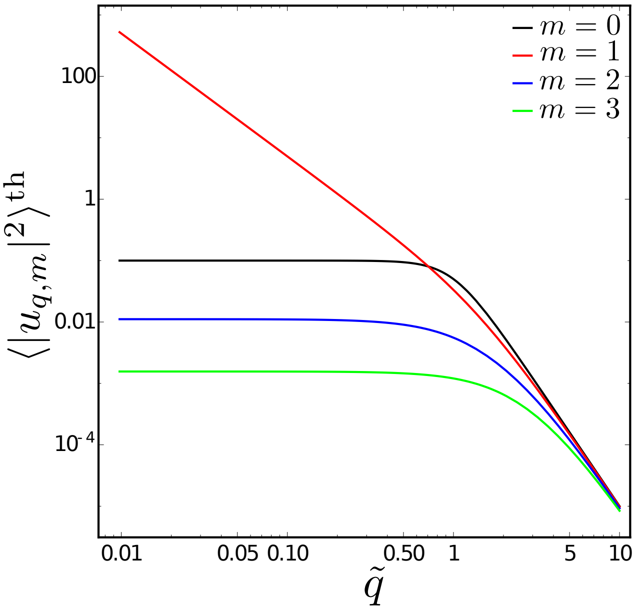

Figure 4.5: Equal time covariance for thermal fluctuations plotted against wavenumber $\tilde{q}$ for modes $m = 0, 1, 2, 3$. We choose $\sigma = \kappa/(2r_0^2)$ or $\tilde{\sigma} = 1/2$.

A striking prediction given by this theory is the divergence of the $m = \pm 1$ modes, i.e., criticality, in the long wavelength limit. This criticality is due to the $m = \pm 1$ modes being one-dimensional Goldstone modes (they only locally translate the cross-section of the tube which does not alter the energy in the long wavelength limit). The equilibrium properties of such fluctuations, such as excess area and length fluctuations, are discussed in detail in Ref. [Fournier and Galatola, 2007]. It is expected that due to the uni-dimensional character of these modes that the criticality will be preserved, even in the anharmonic regime [Fournier and Galatola, 2007].

4.5.2 Active fluctuations

Turning our attention to the case of active fluctuations, we will find the statistical properties of the shape fluctuations due to purely active noise. We assume that the active and thermal noise terms are uncorrelated, hence the total shape fluctuations can be found by simply adding the active and passive contributions.

To find the covariance we Fourier transform in time with the convention $u(t) = \int \mathrm{d}\omega/(2\pi)\, u(\omega)e^{i\omega t}$, and find the covariance

$$\langle u_{qm}(\omega)u^*_{q'm'}(-\omega')\rangle^{\mathrm{ac}} = \frac{F^2\tau_*\delta_{qq'}\delta_{mm'}\delta(\omega-\omega')}{(A^2+B^2\omega^2)(1+\tau_*^2\omega^2)}. \tag{4.37}$$

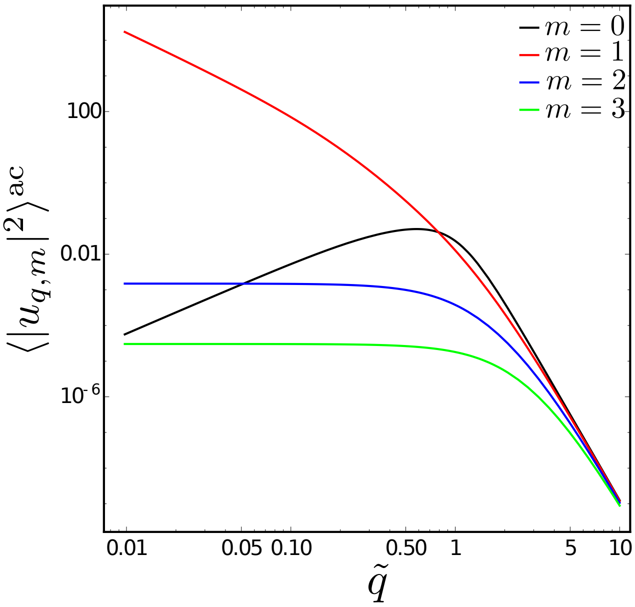

Figure 4.6: Equal time covariance for active fluctuations of the membrane tube plotted against wave-number $\tilde{q}$ for modes $m = 0, 1, 2, 3$. We choose $\sigma = \kappa/(2r_0^2)$, $\chi = 0$, $F = 0.5$ and $\tau_* = 10\tau = 10\eta r_0^3/\kappa$.

Inverting the Fourier transform for ω and ω' gives the covariance in time, which after some algebra gives

$$\langle u_{qm}(t)\, u^*_{q'm'}(t')\rangle^{\mathrm{ac}} = \frac{F^2\tau_*}{2A}\frac{A\tau e^{-|t-t'|/\tau_*} - Be^{-|t-t'|A/B}}{A^2\tau_*^2 - B^2}\delta_{qq'}\delta_{mm'}, \tag{4.38}$$

which gives the variance

$$\langle|u_{qm}|^2\rangle^{\mathrm{ac}} = \frac{F^2\tau_*}{2A(A\tau_* + B)}. \tag{4.39}$$

As this depends on the dissipation in the system (through the presence of B), it is immediately obvious that the fluctuations are non-equilibrium. If we assume that the activity correlation time is an order of magnitude more than the viscous time-scale, $\tau_* \sim 10\tau = 10\eta r_0^3/\kappa$, and that the forces exerted on the membrane are $f \sim 1$pN over an area r_0^2, then $F \sim 0.1 - 1$ [Sachin Krishnan et al., 2018]. Using these parameters along with $\chi = 0$, $F = 0.5$ we can plot the active fluctuations, Eq. (4.39), in Fig. 4.6.

The same divergence at small $\tilde{q}$ is observed in the $m = 1$ modes (with the same exponent as in the thermal case). The $m = 0$ mode shows a peak, the position of which can be shifted by changing the value of the active time-scale, τ_*, (relative

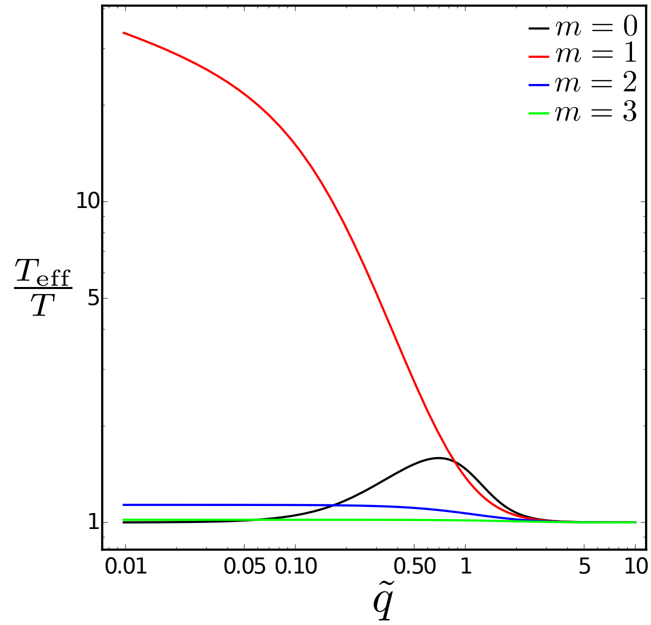

Figure 4.7: Effective temperature of the membrane tube with both thermal and active fluctuations, Eq. (4.40), plotted against wave-number $\tilde{q}$ for modes $m = 0, 1, 2, 3$. We choose $\sigma = \kappa/(2r_0^2)$, $\chi = 0$, $F = 0.5$ and $\tau_* = 10\tau = 10\eta r_0^3/\kappa$.

to the viscous time-scale, $\tau = \eta r_0^3/\kappa$). The decay in active fluctuations of the $m = 0$ mode as $\tilde{q} \to 0$ is due to the viscous damping making such non-equilibrium fluctuations unfavourable.

A simple observable to calculate is the effective temperature as a function of Fourier parameters, this is given by

$$\frac{T_{\mathrm{eff}}\left(\tilde{q}, m\right)}{T} = 1 + \frac{\langle |u_{qm}|^2\rangle^{\mathrm{ac}}}{\langle |u_{qm}|^2\rangle^{\mathrm{th}}}. \tag{4.40}$$

This is plotted in Fig. 4.7 for the same parameters of $F = 0.5$, $\tau_* = 10\tau = 10\eta r_0^3/\kappa$, $\chi = 0$ and $\tilde{\sigma} = 1/2$. This shows that for long tubes the highest effective temperature is found in the $m = 1$ modes and that these are likely to dominate the spectrum.

Measuring the temperature of fluctuations of long tubes, for example those pulled from GUVs [Valentino et al., 2016], and varying the viscosity of the exterior fluid may provide a way to quantify the magnitude and time constant of such active correlations in experiment. Fig. 4.8 shows the effective temperature of the $m = 1$ modes for varying relative viscosity χ, along with the asymptotic result predicted using a Zimm model for such modes, see Appendix C.

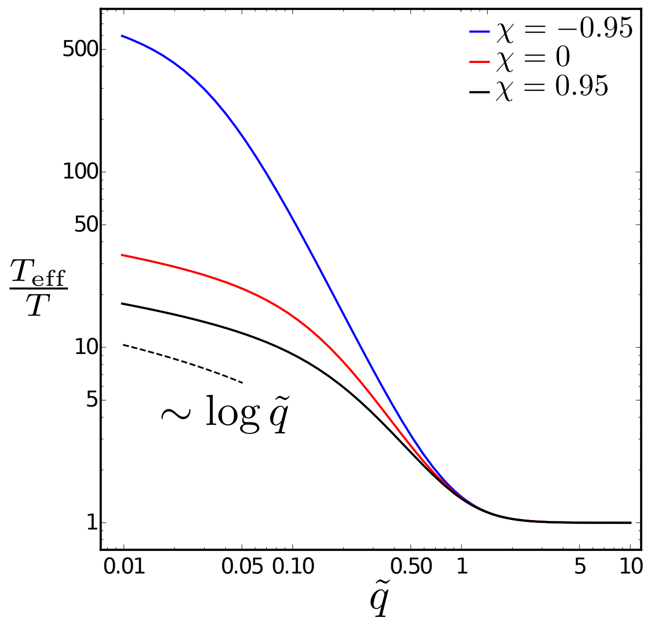

Figure 4.8: Effective temperature of the membrane tube with both thermal and active fluctuations, Eq. (4.40), plotted against wave-number $\tilde{q}$ for modes $m = 1$ for different values of relative viscosity χ. All other parameters are chosen as follows $\sigma = \kappa/(2r_0^2)$, $F = 0.5$ and $\tau_* = 10\tau = 10\eta r_0^3/\kappa$. The dotted line shows the asymptotic approximation found by using a Zimm model for a rod in a viscous fluid.

4.6 Discussion

In this chapter we have investigated the active and passive dynamics of fluid membrane tubes. Using Onsager's variational formalism we have calculated the full relaxation dynamics for the Fourier modes in the shape of the membrane tube, assuming a small deformation limit, and analysed the asymptotic limits of the relaxation rates. This work accounts for variations in surface tension, previously only considered in the axisymmetric case [Boedec et al., 2014], and also viscosity contrast between the interior and exterior ambient fluid.

The scaling behaviour of the relaxation modes is analysed and characterised in both the long and short wavelength limits. Unsurprisingly, in the short wavelength limit we recover the scaling behaviour of a flat membrane for all angular modes. More interesting behaviour is found in the long wavelength limit, particularly in the case of the bending modes ($m = \pm 1$), where we find a relaxation rate that scales like that of the normal modes of an elastic rod in a viscous fluid. We can also reproduce the pearling instability growth rate found in Ref. [Boedec et al., 2014] which is recovered when we set $m = 0$ and choose a sufficiently high value of surface tension ($\sigma > 3\kappa/(2r_0^2)$). These relaxation dynamics are significantly different from those found for flat membranes [Fournier, 2015; Seifert and Langer, 1994] or for spherical vesicles [Sachin Krishnan et al., 2016]. In the case of the spherical vesicles the system can be written purely in terms of a sum over one Fourier variable due to the coupling imposed by spherical symmetry. This does not happen in the case of the tube as $\tilde{q}$ and m are independent of one another.

We then make use of these relaxation equations to compute the fluctuation spectra for passive thermal fluctuations and a simple minimal model of active fluctuations [Sachin Krishnan et al., 2018; Gov, 2004]. The active noise clearly breaks the fluctuation dissipation theorem, due to the presence of dissipative terms in the mean-square fluctuations, see Eq. (4.39). The active noise also shows the same criticality of the bending modes ($m = 1$) in the long wavelength limit found in thermal fluctuations [Fournier and Galatola, 2007].

We compute the effective temperature of the system with both thermal and active fluctuations and show that, for long tubes, the clearest signature of this active noise is in the bending modes ($m = 1$). This should be a measurable prediction with current experimental setups, *e.g.* using a similar approach seen in Ref. [Valentino et al., 2016] and changing the external viscosity. This could be used to infer information about the size of forces and activity time-scales for different sources of activity (assuming they can be reconstituted *in-vitro*). Perhaps the most pressing open question in the field of active membranes is what functional form is best used to represent the active fluctuations. The simple model of a direct force used in this paper, though used successfully throughout the literature to describe real systems [Gov, 2004; Prost and Bruinsma, 1996; Sachin Krishnan et al., 2018], does not respect force balance at the level of an individual fluctuation. More complex models of activity have been proposed for specific situations, for example using dipole forces and allowing fluid permeation of the membrane [Manneville et al., 2001], however a general framework is lacking and the effect of different models of active noise on observable phenomena is not yet well understood.

For future work, it would be interesting to consider the effects of different formulations of activity (both in tubes and other scenarios). Furthermore, real membranes are often highly heterogeneous, consisting of multiple phases [Sackmann and Feder, 1995]. These multi-component membranes have been shown to have interesting properties, both in their statics [Leibler and Andelman, 1987; Fonda et al., 2018; Wolff et al., 2016] and dynamics [Sankararaman et al., 2002; Komura et al., 2015], which would be interesting to study in the presence of active fluctuations in the highly curved geometry of membrane tubes. It would also be interesting to consider the effect of a visco-elastic ambient fluid as this may give a better approximation to the cytoplasm in cells. Not only would this give potentially richer dynamics, due to the presence of of an additional time-scale, but it could also be useful in understanding more realistic biological processes [Komura et al., 2015; Nixon-Abell et al., 2016; Abounit and Zurzolo, 2012].

Chapter 5

Discussion & Outlook

Lipid membrane tubes are abundant inside cells and their dynamics have been implicated in many important processes. In this thesis we have considered some theoretical models of simple situations, designed to mimic important processes in biology, in an attempt to elucidate the underlying physics. Here we briefly outline some possible future directions of research and extensions to the work in the three main chapters of the thesis.

5.1 Hydro-osmotic instabilities

The main key extension to this work would be considering the effects of a finite length tube, *e.g.* a finite tube surrounded by a "cytosol" opening into a reservoir at lower osmotic pressure. This would lead to gradients in the concentration of ions inside the tube, and hence a gradient in pressure which could then drive flows. This model with small perturbations to the radius (or a sphere/tube geometry if beyond the threshold for a hydro-osmotic instability) could be used to compute a steady state of flux into the tube across the membrane and out into the exterior reservoir. It would be instructive to use such a simple model to analyse whether it can be used for osmoregulation and what constraints are set on the system.

Beyond simple tubes there is significant biological motivation to study the behaviour of such instabilities in tubular networks, both from the contractile vacuole literature [Allen, 2000] and the peripheral endoplasmic reticulum [Nixon-Abell et al., 2016]. Such an investigation would likely require numerical approaches either using *surface evolver* for the statics [Brakke, 1992] or more sophisticated finite element methods for the full dynamics [Elliott and Stinner, 2010; Barrett et al., 2016].

5.2 Shear-driven instabilities

In the case of the shear-driven instability the main result is an amplification of the fluctuations due to shear in the azimuthal flow field on the membrane tube. Again finite element simulations might provide one route to better understanding this problem. However this could prove challenging as most current methods for covariant hydrodynamics do not incorporate fluctuations, which are vital to this phenomenon.

Perhaps the most promising future direction would be to consider experiments similar to the magnetic tweezers setup proposed in Chapter 3. This would give some indication as to how important these shear effects are for real systems, particularly for parameters when the fluctuation amplification is beyond linear analysis. This experiment may prove difficult as oscillations may be introduced to the tube from the magnetic trap so shape undulations may not be purely caused by the shear rate.

The helical geometry of Dynamin could also be considered in more detail and we could also look at the effect of hydrodynamics on other similar proteins (ESCRT for example) [McDargh and Deserno, 2018; Lenz et al., 2008; De Franceschi et al., 2019]. This work would most likely have to be performed numerically or with coarse grained hydrodynamic models as the complex geometry of the ground-state would make the full covariant hydrodynamics intractable [Arroyo and DeSimone, 2009].

5.3 Dynamics of active membrane tubes

In the case of more general theories of active membranes it may be instructive, in the first instance, to consider close to flat membranes (Monge gauge). It would be worth developing a simple model of active fluctuations which does not break force balance locally. One way to do this might be to consider fluctuating quadrupoles acting normal to the membrane and to see if this makes any difference in the fluctuation spectra when compared with the simple direct force model used in Chapter 4 and much of the literature [Gov, 2004]. This would also differ from some of the more physically realistic models of active membranes by having true active fluctuations as opposed to thermal fluctuations coupling to dipole fields which cause the fluctuation dissipation theorem to break down [Manneville et al., 2001].

In terms of experimental verification for membrane tubes it appears that *in-vitro* experiments on tubes pulled from GUVs might soon have the resolution required to measure active fluctuations [Valentino et al., 2016]. In order to be able to compare the experiments meaningfully with theory it would be necessary to calculate how the fluctuation spectrum is modified by a finite length tube and how length fluctuations come into play [Barbetta and Fournier, 2009]. This would be important so as to know exactly which modes should be fitted with the power spectral density inferred from experiment (in the current experimental paper only axisymmetric modes are considered).

5.4 Conclusion

In conclusion, we have developed several theoretical models of dynamical processes in lipid membrane tubes. These models have been heavily inspired by real processes in cell biology, and our analysis has allowed us to understand some of the physics underlying these processes. There are still many outstanding questions in both theory and experiment, with the interplay between the two makes this an exciting area to work as a theorist.

Appendix A

Additional details for Chapter 2

A.1 Approximate solution for slow pumping

Fig. A.1 shows the agreement between the asymptotic solution to the radial dynamics: $\tilde{R}(t) = (1 + t/\tau_{\text{pump}})^{1/2}$ (Eq. (2.18)) and the full numerical solution of Eq. (2.17).

We can find the radius $R(q)$ at which the mode q first goes unstable by finding the zero of the $\alpha(q)$ polynomial, Eq. (2.12), defining $R(q) = \sqrt{3}R_{eq} + \delta R(q)$. For the small q limit and assuming $\frac{\delta R(q)}{R_{eq}}$ is small we find

$$\frac{\delta R(q)}{R_{eq}} \approx \sqrt{3}\,(R_{eq}q)^2\,. \tag{A.1}$$

Using Eq. (A.1) with the approximate solution for $R(t)$ gives a formula for the time the mode q *first* goes unstable

$$t_q^* \approx \tau_{\text{pump}}\left(2 + 6\tilde{q}^2\right) \tag{A.2}$$

where $\tilde{q} = qR_{\text{eq}}$.

A.2 Defining the dominant wavelength

Defining the dominant wavelength of a time dependent growth rate is in general a difficult task; as the peak of the dispersion relation is time dependent we must instead consider the full growth history of each mode. We define the dominant mode at linear order to be the first one to have $\langle|\bar{u}_q|^2\rangle = CR_{eq}^2$ where $C = 1$. It is therefore a sensible thing to check that the chosen value of the cutoff, C, has a minimal effect on our results, i.e. the dominant wavelength at linear order should be constant for

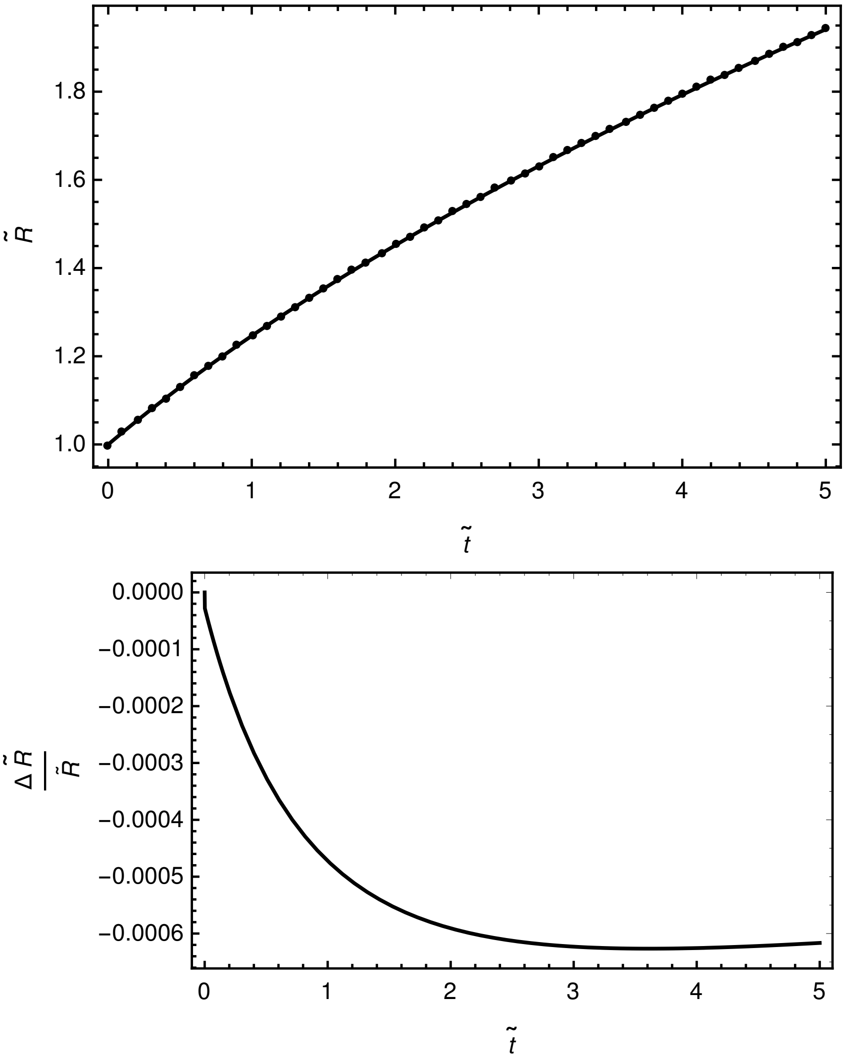

Figure A.1: **Top:** plot showing approximate solution (dots, Eq. (2.18)) and full numerical solution (solid line, Eq. (2.17)) for radius growth due to ion pump osmotic pressure. **Bottom:** plot showing the absolute error between the approximate solution and numerical solution.

$C \sim 1$. Plotting $\tilde{q}^*$ against C, Fig. A.2, shows a weak logarithmic dependence of the dominant wavenumber on C. The only pronounced effect for a cutoff around linear ($C \sim 1$) order might be to shift the values in the fast pumping limit by $< 5\%$, the values for physiological parameters remain virtually unaffected.

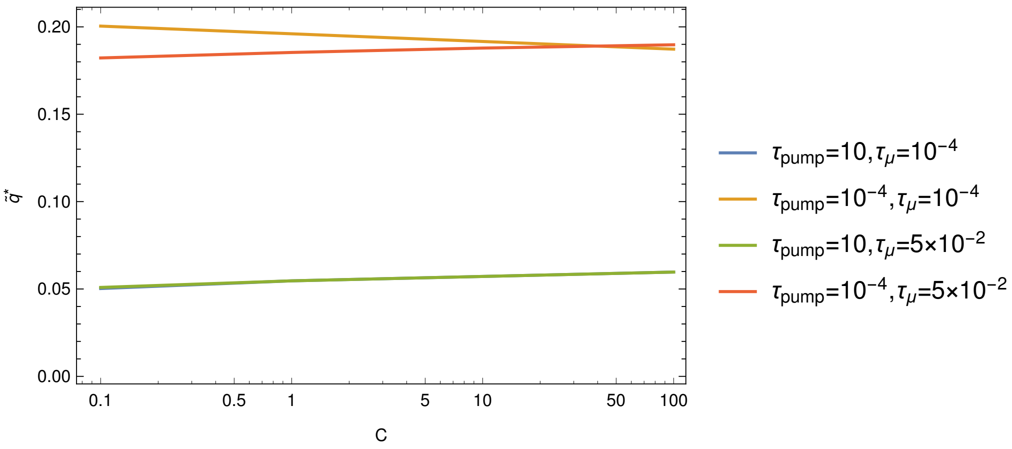

Figure A.2: Plot of dominant wavenumber, $\hat{q}$, against cut-off criterion, C. Crucially any dependence on C is very weak. The values of τ_{pump} and τ_{μ} have been chosen to correspond with the four corners of the surface plot shown in Fig. 2.6. All times are in units of seconds.

A.3 Weak dependence of dominant wavelength on the pumping rate in the physiological range

The asymptotic solution presented in the main paper is valid for parameter estimates consistent with the CVC. It is of interest to see how the wavelength of the instability varies with pumping rate in this limit. The wavelength of the instability varies with pumping rate but very weakly (slower than logarithmically). The wavelength for time-scales consistent with the CV pumping is $\lambda \sim 1\mu$m which is of the correct order of magnitude for the CV and much larger than the tube radius. The weak dependence of the wavelength on the pumping provides a robust mechanism of size regulation, Fig. A.3.

A.4 Osmotic shock

Inserting the time-dependent solution of Eq. (2.19) in the growth equation Eq. (2.26) (including thermal noise, as in Eq. (2.30)) gives access to the evolution of the amplitude of the different modes. The exact value of the dominant $\tilde{q}$ depends on the permeability μ (or the time-scale τ_{μ}) and the magnitude of the shock $\Delta\rho/\rho_0$. A 3D plot of how this varies is shown in Fig. A.4. Comparison with the behaviour that

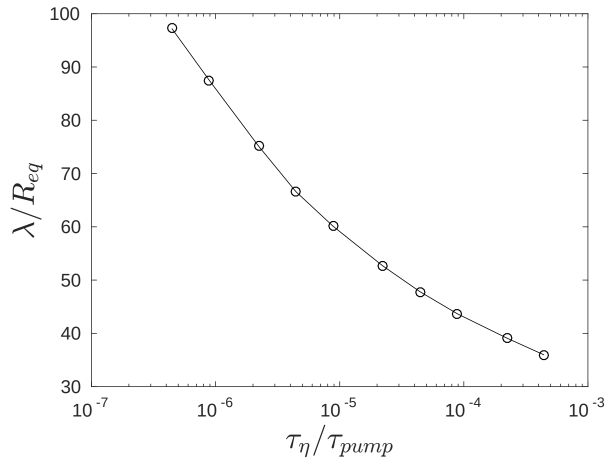

Figure A.3: Plot of dominant length, λ, of instability against ratio of viscous to pumping time-scales $\tau_\eta/\tau_{\text{pump}}$ for the asymptotic solution found in the main paper (Eq. (2.18)). Here $\tau_\eta/\tau_\mu = 10^{-4}$. This plot is essential a cross-section of Fig. 2.6 in the main paper for $\tau_\eta/\tau_\mu = 10^{-4}$, but plotting wavelength instead of wavenumber $\tilde{q}^*$.

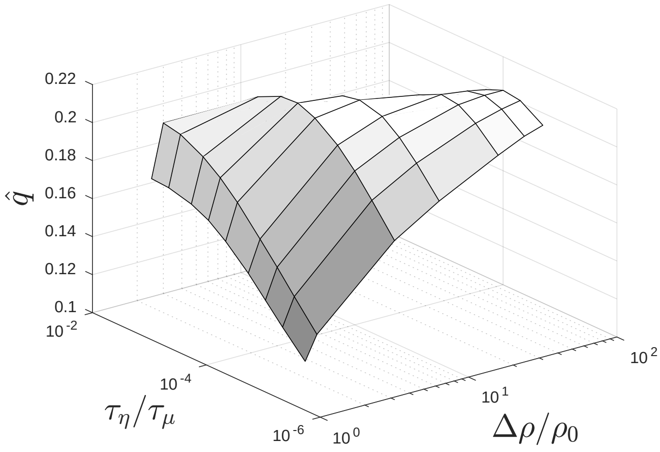

Figure A.4: Surface plot showing the dominant wave-number of an instability driven by osmotic shock when varying permeation time-scale, τ_μ, and shock magnitude $\Delta\rho/\rho_0$.

arises in the presence of ion pumps (Fig. 2.6) shows that the peak value of the dominant mode is the same in both case, and corresponds by the peak of Fig. 2.3. This peak occurs for fast pumping ($\tau_\eta/\tau_\mu > 10^{-2}$ - Fig. 2.6) or for strong osmotic shock ($\Delta\rho/\rho_0 > 10$ - Fig. A.4), showing that these two situations are somewhat similar. However the details are different due to the different dynamics of tube inflation in both cases.

The drop off in dominant wavelength of the osmotic shock instability when permeability and shock magnitude are very large is caused by the decrease of the peak of the growth rate relation at very large radii (Fig. 2.3). This happens because of a decrease in the contribution of the bending rigidity to the energy at large radii and small $\tilde{q}$. The surface tension contribution to the energy remains, hence the instability starts to be dominated by surface tension. The only contribution of the bending terms is to increasingly stabilise the larger values of $\tilde{q}$, thus pushing the peak wavelength to lower $\tilde{q}$. Interestingly the bending rigidity in this limit acts in a qualitatively similar manner to a large difference in viscosities discussed in the original fluid jet papers [Rayleigh, 1892; Tomotika, 1935].

A.5 Note on numerical implementation

All the numerics shown in Fig. 2.5 and Fig. 2.6 of the main paper are implemented using a discrete Fourier transform, as such the autocorrolation function, $\langle|\bar{u}_q|^2\rangle$ has units of $[\text{Length}]^2$, this choice of implementation is used to simplify the criterion for the fully developed instability. The longest mode in real space is chosen to be $10^4 R_{\text{eq}}$, this corresponds to a small enough spacing for the q space to approximate a continuum.

Appendix B

Additional details for Chapter 3

B.1 Differential geometry and exterior calculus

Here we present a “users guide” to the style of geometric notation used in the main paper. We do not focus on mathematical rigour here, for a more formal treatment see [Frankel, 2011].

If we define a manifold $\mathcal{M}^n$ where the derivative of a curve at point $p \in \mathcal{M}^n$ gives an element of the tangent space $\boldsymbol{X}_p \in \mathcal{T}_p(\mathcal{M}^n)$, we can express this in terms of a coordinate basis

$$\boldsymbol{X}_p = X^i \left(\frac{\partial}{\partial x^i}\right)_p = X^i \left(\vec{e}_i\right)_p \tag{B.1}$$

where Einstein summation over mixed indices is implicit.

If we choose a family of curves on $\mathcal{M}^n$ with continuous derivatives we can extend the definition of the tangent space to the tangent bundle on $\mathcal{M}^n$, $\mathcal{T}(\mathcal{M}^n) = \cup_p \mathcal{T}_p(\mathcal{M}^n)$. This extends the definition of a vector to a vector field on the the manifold, $X \in \mathcal{T}(\mathcal{M}^n)$.

The dual of $\mathcal{T}(\mathcal{M}^n)$ can be defined as the cotangent space $\mathcal{T}^*(\mathcal{M}^n)$. An element of this space, a 1-form, is defined in the following way $\boldsymbol{\omega} \in \mathcal{T}^*(\mathcal{M}^n)$

$$\boldsymbol{\omega}(X) \to \mathbb{R}. \tag{B.2}$$

In coordinate notation

$$\boldsymbol{\omega}(\boldsymbol{X}) = \omega_i X^j \mathrm{d}x^i \frac{\partial}{\partial x^j} = \omega_i X^j \delta^i_j = \omega_i X^i. \tag{B.3}$$

In general a type (p, q) tensor field, T is defined in the following way

$$T(X_1, ..., X_p, \omega_1, ..., \omega_q) \to \mathbb{R} \tag{B.4}$$

where $X_1, ..., X_p \in \mathcal{T}(\mathcal{M}^n)$ and $\omega_1, ..., \omega_q \in \mathcal{T}^*(\mathcal{M}^n)$.

We can define a type $(2,0)$ metric tensor on the manifold as

$$g(\cdot,\cdot): \quad g(X,Y) \to \mathbb{R} \tag{B.5}$$

where X,$Y \in \mathcal{T}(\mathcal{M}^n)$.

$$g(\cdot,\cdot) = \mathrm{d}s^2 = g_{ij}\mathrm{d}x^i\mathrm{d}x^j = \vec{e}_i \cdot \vec{e}_j\mathrm{d}x^i\mathrm{d}x^j \tag{B.6}$$

which allows a mapping between vectors and 1-forms.

The exterior or wedge product between two 1-forms is defined as the totally asymmetric tensor product

$$\boldsymbol{\omega}_1 \wedge \boldsymbol{\omega}_2 = \boldsymbol{\omega}_1 \otimes \boldsymbol{\omega}_2 - \boldsymbol{\omega}_2 \otimes \boldsymbol{\omega}_1. \tag{B.7}$$

A p-form, α, can be defined from p 1-forms as

$$\alpha = \boldsymbol{\omega_1} \wedge ... \wedge \boldsymbol{\omega}_p. \tag{B.8}$$

This has the following property

$$\boldsymbol{\omega}_1 \wedge ... \wedge \boldsymbol{\omega}_r \wedge ... \wedge \boldsymbol{\omega}_s \wedge ...\boldsymbol{\omega}_p = -\boldsymbol{\omega}_1 \wedge ... \wedge \boldsymbol{\omega}_s \wedge ... \wedge \boldsymbol{\omega}_r \wedge ...\boldsymbol{\omega}_p \tag{B.9}$$

for any two s, r. Or in coordinate notation

$$a_{i...r...s...j} = -\alpha_{i...s...r...j} \tag{B.10}$$

where $\alpha = \alpha_{i...j}\mathrm{d}x^i \wedge ... \wedge \mathrm{d}x^j$.

This along with the metric leads to the natural geometric definition of the volume form $\mathrm{vol}^n := \sqrt{g}\mathrm{d}x^1 \wedge ... \wedge \mathrm{d}x^n$, where $g := \det(g_{ij})$.

The exterior derivative, $\boldsymbol{d}$, of a smooth function f is just its differential $\boldsymbol{d}f = \frac{\partial f}{\partial x^i}\mathrm{d}x^i$. The exterior derivative, $\boldsymbol{d}$, of a p form is a $p+1$ form

$$\boldsymbol{d}\alpha = \boldsymbol{d}\alpha_{i...j} \wedge \mathrm{d}x^i \wedge ... \wedge \mathrm{d}x^j. \tag{B.11}$$

The Hodge star operator, $\star : \tau^*(\mathcal{M})^{(k)} \to \tau^*(\mathcal{M})^{(n-k)}$, is defined by the Hodge inner product of two differential forms α and β

$$\alpha \wedge \star\beta = (\alpha \cdot \beta)\,\mathrm{vol}^n \tag{B.12}$$

in coordinate notation we have

$$\star\,\alpha = \epsilon_{i_1\ldots i_n}\sqrt{\det g}\alpha_{j_1\ldots j_k}g^{i_1j_1}\ldots g^{i_kj_k}\mathrm{d}x^{i_{k+1}}\wedge\cdots\wedge\mathrm{d}x^{i_n} \tag{B.13}$$

where ϵ is the totally asymmetric tensor.

A diffeomorphism is a map between two manifolds that is smooth, one-to-one, onto and has a smooth inverse. The Lie derivative is a natural object to use in continuum mechanics as it describes how a vector field Y changes along the flow generated by a vector field X. If $\phi(t) = \phi_t$ is a diffeomorphism parametrised by t and describing the local flow generated by X, where t is defined such that $\lim_{t\to 0}\phi_t(X) = X$, then we define the Lie derivative of a vector field Y with respect to a vector field X as follows

$$[\mathcal{L}_X Y]_x = \lim_{t\to 0}\frac{[\phi_{-t*}Y_{\phi_t x} - Y_x]}{t} = X(Y) - Y(X) \tag{B.14}$$

as such $\mathcal{L}_X Y$ is a vector field on $\mathcal{M}^n$. Similar identities can be derived for more general tensors [Frankel, 2011].

We will define the Laplace-Beltrami operator as

$$\Delta_{\mathrm{LB}} = -\star\boldsymbol{d}\star\boldsymbol{d} \tag{B.15}$$

which for scalar ϕ and vector $\boldsymbol{v}$ is the following in index notation

$$\begin{aligned}\Delta_{\mathrm{LB}}\phi &= -\frac{1}{\sqrt{|g|}}\partial_i\left(\sqrt{|g|}g^{ij}\partial_j\phi\right)\\ \Delta_{\mathrm{LB}}v^q &= -\sqrt{|g|}\epsilon_{np}\epsilon_{kl}g^{pq}g^{nm}\partial_m\left(\sqrt{|g|}g^{kj}g^{li}\partial_j\left(v^r g_{ri}\right)\right)\end{aligned} \tag{B.16}$$

where the later formula is not usually given in the literature as it is simpler to work with exterior calculus identities (which is how we will proceed).

One final point of note is that we will use the $\flat$, $\sharp$ notation to denote raising and lowering of indices for conciseness. For example, if $\boldsymbol{v}\in\mathcal{T}\left(\mathcal{M}^n\right)$ and $\omega\in\mathcal{T}^*\left(\mathcal{M}^n\right)$, then

$$\begin{aligned}\boldsymbol{v}^\flat &= g_{ij}v^j\mathrm{d}x^i = v_i\mathrm{d}x^i\\ \omega^\sharp &= g^{ij}\omega_j\vec{e}_i = \omega^i\vec{e}_i.\end{aligned} \tag{B.17}$$

B.2 Screening of membrane flows by bulk fluid mechanics

We will consider hydrodynamics on a static membrane tube (i.e. we assume that the cylindrical geometry is stable to perturbations in shape). In the limit of small inertia the 3D velocity field, $\vec{u}$, satisfies the continuity and Stokes equations

$$\vec{\nabla} \cdot \vec{u} = 0; \quad \eta \nabla^2 \vec{u} = \vec{\nabla} P \tag{B.18}$$

where P is the pressure and η the viscosity. This is coupled to the membrane velocity at the boundary with a no-slip condition.

Stress balance at the membrane is imposed by the 2D continuity and Stokes equations and, for surfaces of zero Gaussian curvature, can be written as

$$\nabla_i v^i = 0; \quad \eta_m \Delta_{\mathrm{LB}} v_i - \nabla_i \sigma = t_i^+ + t_i^- \tag{B.19}$$

where η_m is the (2D) membrane viscosity, σ is the surface tension, $\boldsymbol{v} = v^i \boldsymbol{e}_i$ is the tangential membrane velocity and Δ_{LB} is the Laplace-Beltrami operator (formally this corresponds to $\Delta_{\mathrm{LB}} = \boldsymbol{\delta d}$ where $\boldsymbol{d}$ is the exterior derivative and $\boldsymbol{\delta}$ is the co-differential). The combined operator $\boldsymbol{\delta d}$ is the generalization of the curl-curl operator to a manifold and acts like a Laplacian [Rahimi et al., 2013; Arroyo and DeSimone, 2009]. The symbols $t_i^{\pm}$ are the traction forces from the bulk fluid acting on the membrane (± denoting interior and exterior respectively)[Arroyo and DeSimone, 2009; Fournier, 2015].

We will consider a system of a membrane tube with radius $r_0 = \sqrt{\frac{\kappa}{2\sigma_0}}$, where κ is the bending rigidity of the membrane and σ_0 is the equilibrium surface tension. This is the radius which minimizes the Helfrich Hamiltonian for a fluid membrane

$$\mathcal{F} = \int_\Gamma \mathrm{d}A_\Gamma \left(2\kappa H^2 + \sigma_0\right) \tag{B.20}$$

where Γ and $\mathrm{d}A_\Gamma$ denote the manifold describing the neutral surface of the membrane and its associated area element, and H is the mean curvature [Zhong-Can and Helfrich, 1989]. For typical membrane tubes fissioned by Dynamin $r_0 \approx 10$nm [Roux, 2014].

We use standard cylindrical coordinates (r, θ, z) and take the boundary condition for flow on the membrane to be $\boldsymbol{v}|_{z=0} = v_0 \vec{e}_\theta$, we treat this as an approximation to the flow induced by Dynamin.

We can then solve Eq. (B.18) & Eq. (B.19), making use of symmetry $\boldsymbol{v} =$

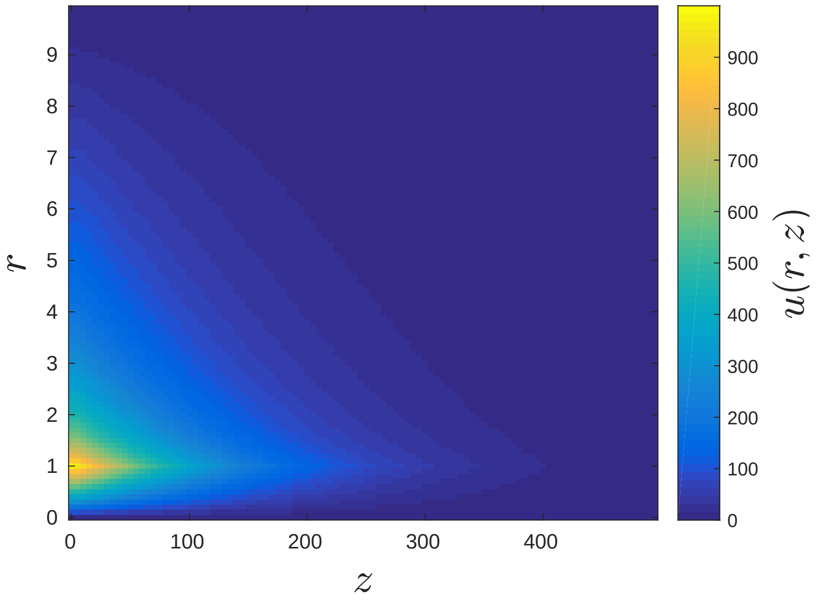

Figure B.1: Flow field for the ground-state of the spinning membrane tube with radius $r_0 = 1.0$, and Saffman-Delbrück length $\frac{L_{\mathrm{SD}}}{r_0} = \frac{\eta_m}{\eta r_0} = 10^4$. The boundary condition on the tube at $z = 0$ is $v(0) = v_0$ where $\frac{v_0}{r_0} = 10^3 \mathrm{s}^{-1}$.

$v(z)\vec{e}_\theta$, $\vec{u} = u(r, z)\vec{e}_\theta$ they reduce to

$$\begin{aligned} \frac{1}{r}\partial_r\left(r\partial_r u_\theta\right) + \partial_z^2 u_\theta - \frac{u_\theta}{r^2} &= 0 \\ \eta_M \partial_z^2 v + t_\theta^+ + t_\theta^- &= 0 \end{aligned} \tag{B.21}$$

where $t_\theta^\pm = \lim_{r\to r_0} \eta r \partial_r \left(\frac{\partial_r u^\pm}{r}\right)$. We can now solve this numerically by direct methods (taking a Neumann boundary condition for the bulk flow at $z = 0$ and $u = 0$ at large distance and $r = 0$) [Ferziger and Peric, 2002]. The flow field computed by this method can be seen in Fig. B.1.

To understand how the flow field on the membrane varies with Saffman-Delbrück length it is helpful to examine the analytic solutions to the coupled membrane bulk system in Fourier space. The flow field on the membrane in response to a point force in the θ direction, F_θ, was found analytically in Ref. [Henle and Levine, 2010], and in the limit $r_0 \ll L_{\mathrm{SD}}$ this gives

$$\boldsymbol{v} \approx v_0 \vec{e}_\theta \exp\left[-\frac{\sqrt{2}|z|}{\sqrt{L_{\mathrm{SD}} r_0}}\right]. \tag{B.22}$$

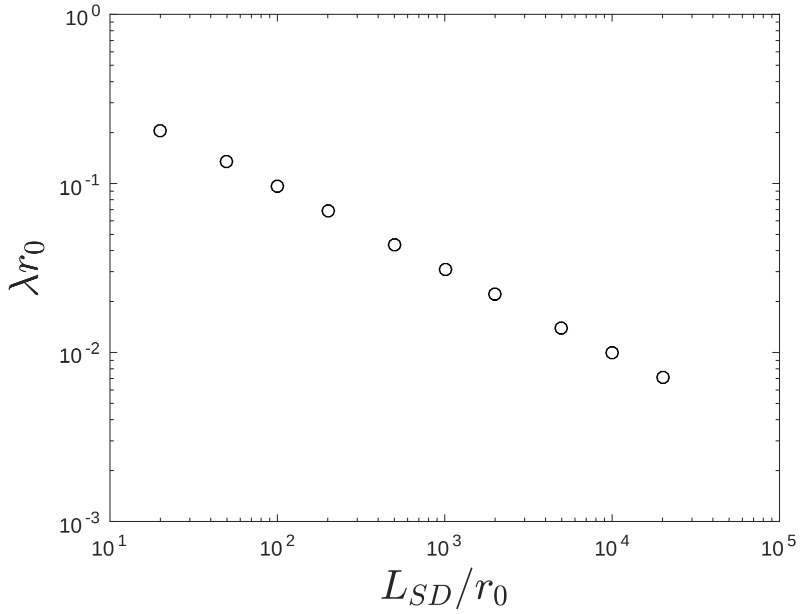

Figure B.2: Flow-field decay rate, λ (with units Length^{-1}) against Saffman-Delbrück length L_{SD} for tube spinning velocity at $z = 0$ given by $\frac{v_0}{r_0} = 10^3\mathrm{s}^{-1}$.

In the original paper our boundary condition corresponds to $v_0 = \frac{F_\theta}{4\pi\eta_m}\sqrt{\frac{L_{\mathrm{SD}}}{2r_0}}$. Note that this is θ independent as the $m = 0$ Fourier mode dominates the bulk dynamics in this limit, so each cross-section of the tube rotates with a constant velocity. This means that the flow on a tube is screened like $v \sim e^{-\lambda|z|}$ where $\lambda = \frac{\sqrt{2}}{\sqrt{L_{\mathrm{SD}} r_0}}$. This approximate analytical expression can be compared to numerical solutions where we find that it reproduces the correct power law relation between λ and L_{SD}, see Fig. B.2.

For flows with large $L_{\mathrm{SD}}/r_0 \sim 10^3 - 10^4$ this gives a screening length of order $100r_0$ so as long as we consider flows where $L \lesssim 10r_0$ then membrane dissipation should dominate.

B.3 Effects of geometry on driving force

To try and understand the effect of the instability in more complex geometry (in particular with non-zero Gaussian curvature in the ground state), we need to consider the term driving the instability as the full calculation becomes intractable very quickly. All the forces acting normal to the membrane which drive the instability are due to the term ${b^i}_j \nabla_i v^j$, in particular the driving force (per area) is set by the linear response coefficient of the mixed second derivative of the shape, $k_{\theta z}(z)$ which is now a function of z due to change in geometry (specifically the non-constant gradient in the flow field ground state). The driving force per unit area scales like

$$f_{\text{driving}} \sim 2\eta_m k_{\theta z}(z)\frac{\partial^2 u}{\partial\theta\partial z} \tag{B.23}$$

so we will consider how $k_{\theta z}(z)$ changes as we change the geometry of our ground-state.

For some general axisymmertic ground-state parametrized by the vector $\vec{X} = (r(z)\cos\theta, r(z)\sin\theta, z)$ with ground-state flow field $v0(z)\vec{e}_\theta$ we find (up to linear order in perturbations)

$$b^i{}_j\nabla_i v^j = a_{z0\theta0}\delta v_z + a_{z1\theta0}\partial_z\delta v_z + k_{\theta z}\frac{\partial^2 u}{\partial\theta\partial z} + b_{z0\theta1}\partial_\theta\delta v_\theta + k_\theta\partial_\theta u \tag{B.24}$$

where

$$\begin{aligned}
a_{z0\theta0} &= \frac{-r'(z) - 2r'(z)^3 - r'(z)^5 + r(z)^2 r'(z) r''(z)^2}{r(z)^2(1+r'(z)^2)^{5/2}}\\
a_{z1\theta0} &= \frac{r''(z)}{(1+r'(z)^2)^{3/2}}\\
k_{\theta z} &=\\
&\Big[-v0(z)r'(z) - v0(z)r'(z)^3 + r(z)v0'(z) + r(z)r'(z)^2 v'(z) + r(z)v0(z)r'(z)r''(z)\Big]\\
&\times\Big(r(z)^2(1+r'(z)^2)^{5/2}\Big)^{-1}\\
b_{z0\theta1} &= \frac{1}{r(z)^2\sqrt{1+r'(z)^2}}\\
k_\theta &= \frac{v0(z)}{r(z)^3\sqrt{1+r'(z)^2}}
\end{aligned} \tag{B.25}$$

B.3.1 Neck (Catenoid)

To consider the effect of the instability in a more realistic *in-vivo* situation, for example on the neck of a budding vesicle, we look at the ground state flows and $k_{\theta z}$ on a catenoid, $r(z) = r_0\cosh\left(\frac{z}{r_0}\right)$. The ground state surface flow is solved numerically with boundary conditions $v(0) = 1$, $v(2) = 0$ taking $r_0 = 1$ and $L = 2$ for simplicity. From this we can evaluate $k_{\theta z}$ and compare to the case of a tube. This is shown in Fig. B.3. Note the amplification of $k_{\theta z}$ by a factor of 2 near the centre of the catenoid when compared to the tube. The consequences of this for

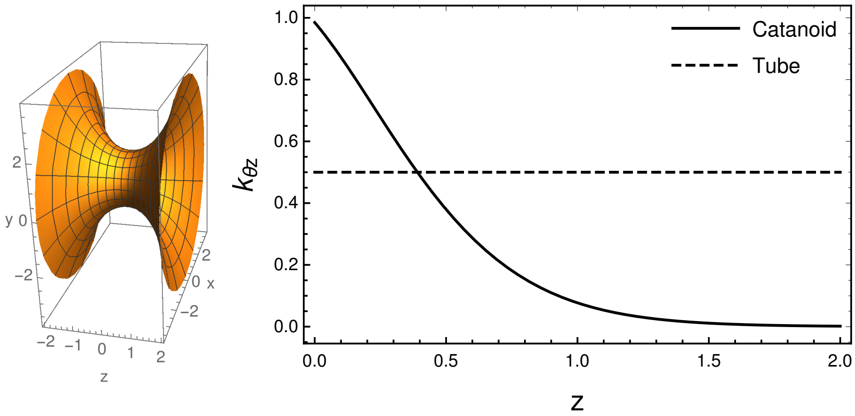

Figure B.3: Left: plot of the catenoid with radius $r_0 = 1$. Right: Plot of the force linear response coefficient for the mixed shape derivative (*i.e.* the term in the normal force that goes like $f \sim k_{\theta z}\partial_{\theta z} u$) for the helical shape perturbations on such a surface.

dynamin are discussed in the main paper.

B.4 Derivation of rate-of-deformation tensor using local constructions

If we consider a membrane which when un-deformed, $\mathcal{M}$, and is approximately flat then its line element (metric) can be written

$$\mathrm{d}s^2 = \mathrm{d}x^2 + \mathrm{d}y^2. \tag{B.26}$$

If we deform this manifold by the vector (ϕ_x, ϕ_y, ψ) to a new manifold $\mathcal{M}'$ and choose coordinates x, y such that the second fundamental form of of $\mathcal{M}'$ is given by

$$b = \begin{pmatrix} \mathrm{d}x & \mathrm{d}y \end{pmatrix} \begin{pmatrix} k_1 & 0 \\ 0 & k_2 \end{pmatrix} \begin{pmatrix} \mathrm{d}x \\ \mathrm{d}y \end{pmatrix}. \tag{B.27}$$

The new metric on the surface $\mathcal{M}'$ is given by $\mathrm{d}s'^2 = (\mathrm{d}x')^2 + (\mathrm{d}y')^2$ where, to lowest order,

$$\begin{aligned} \mathrm{d}x' &= (1 - k_1\psi)\,(1 + \partial_x\phi_x)\,\mathrm{d}x + \partial_y\phi_x\mathrm{d}y \\ \mathrm{d}y' &= (1 - k_2\psi)\,(1 + \partial_y\phi_y)\,\mathrm{d}y + \partial_x\phi_y\mathrm{d}x. \end{aligned} \tag{B.28}$$

so the new metric is given by

$$\begin{aligned} \mathrm{d}s'^2 = (1 - 2k_1\psi - 2\partial_x\phi_x)\,\mathrm{d}x^2 + 2\left(\partial_x\phi_y + \partial_y\phi_x\right)\mathrm{d}x\mathrm{d}y \\ + (1 - 2k_2\psi - 2\partial_y\phi_y)\,\mathrm{d}y^2 \end{aligned} \tag{B.29}$$

up to linear order in the variables (ϕ_x, ϕ_y, ψ) and their derivatives.

If we assume $(\phi_x, \phi_y, \psi) = \Delta t\,(v_x, v_y, w) = \Delta t\vec{V}$, where $\vec{V}$ is the membrane velocity then we can write

$$\begin{aligned} L &= \frac{1}{2}\left[\mathrm{d}s'^2 - \mathrm{d}s^2\right] \\ &= \Delta t\left[(\partial_x v_x - k_1 w)\,\mathrm{d}x^2 + (\partial_x v_y + \partial_y v_x)\,\mathrm{d}x\mathrm{d}y + (\partial_y v_y - k_2 w)\,\mathrm{d}y^2\right] \end{aligned} \tag{B.30}$$

and dividing by Δt and taking the limit $\Delta t \to 0$ gives the rate of deformation tensor

$$d = \left[\frac{1}{2}\left(\nabla_i v_j + \nabla_j v_i\right) - w b_{ij}\right]\mathrm{d}x^i \otimes \mathrm{d}x^j. \tag{B.31}$$

Appendix C

Additional details for Chapter 4

C.1 Expressions for $\Phi^{\pm}_{qm}$, $\Psi^{\pm}_{qm}$, $\Xi^{\pm}_{qm}$

Here we give expressions for the scalar Laplace function decompositions for the Stokes equations after imposing the boundary condition, Eq. (4.22) and making use of the continuity equation to eliminate v^{θ}_{qm}. This gives

$$\begin{aligned}
\Phi^{+}_{qm} = 2r_0 \Bigg[& \tilde{q}\left(4iv^{z}_{qm} - 3\tilde{q}r_0\dot{u}_{qm}\right)K^2_{m-1} - 4m\left(\tilde{q}r_0\dot{u}_{qm} - 2iv^{z}_{qm}\right)K_{m-1}K_m \\
& + 4\left(r_0\dot{u}_{qm} + iv^{z}_{qm}\right)K^2_m, -\tilde{q}^2 r_0\dot{u}_{qm}K^2_{m+1}\Bigg] \times \Bigg[7\tilde{q}^3K^3_{m-1} \\
& + 2\left(9m-8\right)\tilde{q}^2K^2_{m-1}K_m + 4\tilde{q}\left(m\left(m-8\right) - 2\tilde{q}^2\right)K_{m-1}K^2_m \\
& - 8m\left(m^2+\tilde{q}^2\right)K^3_m + \tilde{q}^3K^3_{m+1}\Bigg]^{-1},
\end{aligned} \tag{C.1}$$

$$\begin{aligned}
\Psi^{+}_{qm} = r_0 \Bigg[& -8K^2_m\left(v^{z}_{qm}\left(m^4 + 2(m+1)m\tilde{q}^2 + \tilde{q}^4\right) - i\tilde{q}r_0\dot{u}_{qm}\left(m(3m+2) + \tilde{q}^2\right)\right) \\
& + 8\tilde{q}K_{m-1}K_m\left(\left(m^3 + (m-2)\tilde{q}^2\right)v^{z}_{qm} - i(m-2)\tilde{q}r_0\dot{u}_{qm}\right) \\
& + 2\tilde{q}^2\left(3K^2_{m-1} + K^2_{m+1}\right)\left(\left(m^2+\tilde{q}^2\right)v^{z}_{qm} - i\tilde{q}r_0\dot{u}_{qm}\right)\Bigg] \\
& \times \Bigg[m\tilde{q}\Big(8\left(m^3 + m\tilde{q}^2\right)K^3_m - 7\tilde{q}^3K^3_{m-1} - \tilde{q}^3K^3_{m+1} \\
& + 2(8-9m)\tilde{q}^2K_mK^2_{m-1} + 4\tilde{q}\left(2\tilde{q}^2 - (m-8)m\right)K^2_mK_{m-1}\Big)\Bigg]^{-1},
\end{aligned} \tag{C.2}$$

$$
\begin{aligned}
\Xi^{+}_{qm} = r_0 \Big[& -8iK_m^2 \left(v^z_{qm}\left(m^2+\tilde{q}^2\right) - i(m+1)\tilde{q}r_0\dot{u}_{qm}\right) \\
& + \left(6i\tilde{q}^2K_{m-1}^2 + 2i\tilde{q}^2K_{m+1}^2\right)v^z_{qm} - 8\tilde{q}K_mK_{m-1}\left(\tilde{q}r_0^2\dot{u}_{qm} - imv^z_{qm}\right)\Big] \\
& \times \Big[\tilde{q}\Big(-8\left(m^3+m\tilde{q}^2\right)K_m^3 + 7\tilde{q}^3K_{m-1}^3 + \tilde{q}^3K_{m+1}^3 \\
& + 2(9m-8)\tilde{q}^2K_mK_{m-1}^2 + 4\tilde{q}\left((m-8)m-2\tilde{q}^2\right)K_m^2K_{m-1}\Big)\Big]^{-1},
\end{aligned}
\tag{C.3}
$$

$$
\begin{aligned}
\Phi^{-}_{qm} = r_0 \Big[& I_m^2\left(\left(m^2-1\right)r_0\dot{u}_{qm} - i\tilde{q}v^z_{qm}\right) + \tilde{q}I_{m-1}^2\left(\tilde{q}r_0\partial u_{qm} - iv^z_{qm}\right) \\
& - 2mI_mI_{m-1}\left(\tilde{q}r_0\dot{u}_{qm} - iv^z_{qm}\right)\Big] \times \Big[\tilde{q}\Big(\tilde{q}^2I_{m-1}^3 \\
& + \left(2(m-2)m-\tilde{q}^2\right)I_m^2I_{m-1} + (2-3m)\tilde{q}I_mI_{m-1}^2 + m\tilde{q}I_m^3\Big)\Big]^{-1},
\end{aligned}
\tag{C.4}
$$

$$
\begin{aligned}
\Psi^{-}_{qm} = r_0 \Big[& -2I_mI_{m-1}\left(m^3v^z_{qm} + (m-1)\tilde{q}^2v^z_{qm} - i(m-1)\tilde{q}r_0\dot{u}_{qm}\right) \\
& + \tilde{q}I_{m-1}^2\left(\left(m^2+\tilde{q}^2\right)v^z_{qm} - \tilde{q}ir_0\dot{u}_{qm})\right) \\
& + iI_m^2\left(r_0\dot{u}_{qm}\left(2m(m+1)+\tilde{q}^2\right) + i\tilde{q}v^z_{qm}\left(m(m+2)+\tilde{q}^2\right)\right)\Big] \\
& \times \Big[m\tilde{q}\Big(\tilde{q}^2I_{m-1}^3 + \left(2(m-2)m-\tilde{q}^2\right)I_m^2I_{m-1} \\
& + (2-3m)\tilde{q}I_mI_{m-1}^2 + m\tilde{q}I_m^3\Big)\Big]^{-1},
\end{aligned}
\tag{C.5}
$$

$$
\begin{aligned}
\Xi^{-}_{qm} = r_0 \Big[& I_mI_{m-1}\left(-\tilde{q}r_0^2\dot{u}_{qm} + 2imv^z_{qm}\right) + I_m^2\left((m+1)r_0\dot{u}_{qm} + i\tilde{q}v^z_{qm}\right) \\
& - i\tilde{q}v^z_{qm}I_{m-1}^2\Big] \times \Big[\tilde{q}\Big(\tilde{q}^2I_{m-1}^3 + \left(2(m-2)m-\tilde{q}^2\right)I_m^2I_{m-1} \\
& + (2-3m)\tilde{q}I_mI_{m-1}^2 + m\tilde{q}I_m^3\Big)\Big]^{-1},
\end{aligned}
\tag{C.6}
$$

where the modified Bessel functions K_ν, I_ν are evaluated at $r = r_0$.

C.2 Relaxation dynamics of linear Zimm model

Here we consider the relaxation dynamics of small planar normal perturbations to a thin elastic rod whose position is given by

$$\vec{r} = \left(x(t)\cos qz, 0, z\right), \tag{C.7}$$

and has geodesic curvature $k_g = -q^2 x \cos qz$.

We will assume $x(t)$ is small compared with the scales we are considering such that the elastic force-per-unit length on the rod is given by

$$\vec{f} = \left(-A\nabla^2 k_g + Tk_g, 0, 0\right) = \left(-Aq^4 x\cos qz - Tq^2 x\cos qz, 0, 0\right), \tag{C.8}$$

where A is the bending rigidity of the rod and T is the tension [Audoly and Pomeau, 2010].

We can now write the dynamics of this rod as a continuous Zimm model

$$\dot{\vec{r}} = -\int \mathrm{d}\vec{s}\,\Lambda\left(\vec{r}-\vec{s}\right)\vec{f}\left(\vec{s}\right), \tag{C.9}$$

where

$$\Lambda\left(\vec{r}-\vec{s}\right) = \frac{1}{8\pi\eta|\vec{r}-\vec{s}|}\left[\mathbb{I} - \frac{\left(\vec{r}-\vec{s}\right)\otimes\left(\vec{r}-\vec{s}\right)}{|\vec{r}-\vec{s}|^2}\right] \tag{C.10}$$

is the Oseen tensor [Doi and Edwards, 1986].

At linear order and in the long wavelength limit (we choose a short wavelength cut-off of the rod radius, r_0) this gives

$$\dot{x} \approx \frac{(Aq^4 + Tq^2)\mathrm{Ci}(qr_0)}{4\pi\eta}x, \tag{C.11}$$

where $\mathrm{Ci}\left(qr_0\right) = -\int_{r_0}^{\infty}\mathrm{d}x'\,\cos(qx')/x'$. This gives a relaxation rate that scales like $\lambda \sim -\left(\gamma + \log\tilde{q}\right)\tilde{q}^2$ in the small $\tilde{q}$ limit, where γ is the Euler constant. This agrees with the scaling of a membrane tubes bending mode in the long wavelength limit.

Appendix D

Résumé de thèse en français

Les tubes membranaires sont des structures omniprésentes dans les cellules, et la compréhension de leur dynamique et de leur morphologie est d'une importance cruciale pour la biophysique cellulaire. Cette thèse aborde plusieurs aspects de la dynamique des tubes membranaires dans des situations où ils sont déséquilibrés par divers processus inspirés par des phénomènes biologiques. Nous analysons le gonflement de tubes due à des pompes ioniques entraînant une différence de pression osmotique, ainsi que les instabilités qui en résultent. Ceci est inspiré par la structure d'un organelle appelé le vacuole contractile, et conduit à une nouvelle instabilité avec une longueur d'onde naturelle beaucoup plus longue que celle résultant d'une instabilité de type pearling. La stabilité des tubes membranaires présentant un écoulement de cisaillement à leur surface est également analysée. Nous avons découvert et analysé une nouvelle instabilité hélicoïdale qui conduit à l'amplifications des fluctuations du tube. Nous discutons de la pertinence de cette instabilité dans le processus de scission des tubes induite par la dynamine. Enfin, nous considérons la dynamique et les fluctuations d'un tube membranaire sur lequel agissent des forces actives.

D.1 Introduction

Nous commençons par esquisser une brève histoire de la mécanique en biologie cellulaire. Nous discutons des travaux de D'Arcy Thompson qui, pour la première fois, appliqua des idées issues des mathématiques et de la physique à l'étude des organismes en 1917. Nous passons ensuite à une vue d'ensemble des développements les plus récents, notamment la nage à faible nombre de Reynolds, les études sur les globules rouges, les cristaux liquides actifs et la dynamique des tiges et des filaments visqueux.

Ensuite, nous décrivons plus en détail l'auto-assemblage des lipides en structures en bicouches membranaires (en particulier dans la phase désordonnée des liquides) et discutons de l'importance de ces membranes comme interfaces entre différents compartiments cellulaires dans les cellules eukaryotes. Étant donné que ces structures sont généralement très minces, elles peuvent être considérées comme des structures 2D entourées par un environnement 3D. Nous introduisons quelques outils de géométrie différentielle pour décrire de telles surfaces (variétés). À partir de là, nous discutons des travaux fondamentaux de Helfrich, Evans et Canham qui ont menés à la définition d'une énergie de courbure pouvant être utilisée pour décrire les formes des bicouches lipidiques.

Nous discutons des formes simples d'énergie minimale, telles que des sphères et des tubes, avant d'énoncer l'équation de forme complète pour décrire une surface arbitraire. En nous limitant aux surfaces possédant une symétrie axiale, nous discutons des solutions qui correspondent à une membrane soumise à force ponctuelle, Fig. 1.8. Nous discutons les considération énergétiques expliquant l'instabilité classique de perlage d'un tube membranaire, qui est observée lorsque la tension superficielle dépasse un seuil critique.

Nous discutons la mécanique statistique de la membrane soumise aux fluctuations thermiques et obtenons le résultat de l'équipartition pour les ondulations quadratiques moyennes d'un tube membranaire. Enfin, nous fournissons une brève discussion de la dynamique des fluides aux échelles cellulaires, en particulier de la façon dont les termes inertiels dans les équations hydrodynamiques peuvent être négligés à cette échelle.

D.2 Instabilités hydro-osmotiques dans les tubes membranaire actifs

Dans ce chapitre, nous étudions un tube membranaire doté de pompes ioniques unidirectionnelles entraînant une différence de pression osmotique. Ceci est inspiré d'un organelle trouvé dans de nombreux protistes d'eau douce (organismes eucaryotes unicellulaires) appelé le complexe vacuole contractile, Fig. 2.1a. Cet organelle agit comme une pompe pour éliminer l'excès d'eau des cellules et constitue ainsi un mécanisme d'osmorégulation. Le vacuole contractile est dotée de pompes à protons unidirectionnelles sur toute sa surface qui consomment de l'ATP pour transporter des protons contre leur gradient de concentration, ce qui entraîne une différence de pression osmotique qui permet à la vésicule principale de se remplir d'eau. Un pore ancre cette vésicule à la membrane plasmique. Lorsque la vésicule est complètement gonflée, ce pore s'ouvre et la pression de Laplace expulse l'eau.

La vésicule principale est entourée de 5 à 10 bras en forme de tubes membranaires, eux aussi recouverts de pompes à ions, qui se gonflent sous l'effet de la différence de pression osmotique et semblent ensuite subir une instabilité montrant un gonflement hétérogène, Fig. 2.1a, b. Ces protubérances ont des tailles caractéristiques bien supérieures à celles d'une instabilité typique de pearling.

Nous étudions ce mécanisme en considérant un tube membranaire infini recouvert de pompes à ions qui transportent des ions à travers la membrane à un taux constant par unité de surface. Nous calculons la croissance du tube en raison de cette augmentation de la pression osmotique, Eq. 2.18, et considérons les perturbations linéaires sur cet état fondamental en évolution constante. Parce que le tube est initialement stable, toutes les ondulations initiales seront amorties. Nous incluons donc un terme de forçage stochastique choisi qui conduirait aux fluctuations thermiques si le tube était en équilibre. La résolution de la dynamique stochastique complète pour le déplacement quadratique moyen des ondulations conduit une instabilité avec un nombre d'onde naturel $\tilde{q} = qr_0 \sim 0.05 - 0.1$ (où r_0 est le rayon d'équilibre du tube) pour des valeurs de paramètres compatibles avec des expériences d'électrophysiologie sur le vacuole contractile. Cela correspond à une longueur d'onde d'environ 1 à 10 microns, ce qui est du même ordre de grandeur que celle des protubérances observées dans le vacuole contractile.

La raison de cette grande longueur d'onde est que le fonctionnement lent des pompes à ions conduit à une dynamique qui reste à tout moment très proche du seuil d'instabilité, de sorte que seules les longueurs d'onde élevés sont rendues instables. Cela est également dû au fait que le taux de croissance des différents modes possède un pic pour un vecteur d'onde $\tilde{q}$ qui est une fonction non monotone de rayon du tube, avec un maximum pour $\tilde{q} = 0.2$. Pour l'instabilité classique du perlage, le taux de croissance possède un pic pour un vecteur d'onde $\tilde{q} = 0.6$ entièrement déterminé par la géométrie du tube. Ce qui contribue également à expliquer la longueur d'onde plus élevée de notre instabilité, voir Fig. 2.2, 2.3. Il s'avère également que cette sélection de longueur d'onde est très robuste aux modifications de nos paramètres. La longueur d'onde exacte est définie par le rapport des temps caractéristiques de pompage ionique et de dissipation visqueuse. Cependant, une modification de plusieurs ordres de grandeur de ce paramètre ne conduit qu'à une variation un facteur de deux de la longueur d'onde.

Nous avons développé un modèle de membrane perméable à l'eau contenant des pompes à ions unidirectionnelles. Les instabilités hydro-osmotiques observées devraient appartenir à cette classe d'instabilités. En dérivant des équations dynamiques pour un tube membranaire, nous identifions une instabilité provoquée par ce déséquilibre osmotique. Cela à une longueur d'onde naturelle qui est définie par les paramètres dynamiques, en particulier le rapport entre l'échelle de temps de pompage et l'échelle de temps visqueuse, et qui est nettement plus longue que celle de l'instabilité de Rayleigh ou de pearling. Il est intéressant de noter que la longueur d'onde obtenue est du même ordre que celle observée dans les bras radiaux du complexe vacuole contractile, ce qui suggère qu'il s'agit d'un mécanisme possible pour expliquer la morphologie de ces bras. Il est également intéressant de noter que la taille latérale des excroissances formées par l'instabilité est du même ordre de grandeur que la taille de la vésicule principale du complexe vacuole contractile. Nous supposons que cette instabilité peut fournir un mécanisme pour la biogenèse du vacuole contractile à partir d'un tube actif sans particularité. Nous avons l'intention d'aborder plus avant la question de cette organellogénèse dans nos travaux futurs.

D.3 Instabilités par cisaillement sur tubes membranaires

Motivés par la mécanique de la scission des tubes membranaires induite par la dynamine, nous utilisons l'hydrodynamique covariante pour analyser la stabilité des tubes membranaires soumis à un flux de cisaillement dans la direction azimutale. L'hydrodynamique covariante des membranes de fluide a suscité un vif intérêt au sein de la communauté des spécialistes de la matière molle et de la physique biologique au cours des dernières années, tant pour les caractéristiques théoriques générales de tels systèmes que pour leur application à des processus biologiquement pertinents. Ces systèmes associent l'hydrodynamique des membranes à l'élasticité de courbure et se sont révélés présenter un comportement viscoélastique complexe dans les géométries à forte courbure.

L'un des moyens les plus simples de décrire les écoulements à la surface de ces tubes consiste à imposer une vitesse dans la direction azimutale. L'analyse des modifications de forme induites par de tels écoulements est le sujet de ce chapitre. La Fig. 3.1 illustre deux mécanismes possibles pour réaliser de tels écoulements via des expériences in vitro et in vivo. La fission des tubes membranaires joue un rôle important dans de nombreux processus cellulaires, allant de l'endocytose à la fission des mitochondries. Le composant clé de la machinerie biologique nécessaire pour induire la fission membranaire est une famille de protéines appelée Dynamin, qui hydrolyse le GTP en GDP. La dynamine est un complexe protéique qui s'oligomérise pour former des polymères qui s'enroulent en hélice autour des tubes membranaires. Il est clairement établi que Dynamin subit un changement de conformation suite à l'hydrolyse du GTP. Cependant, il n'existe pas encore de consensus sur la méthode exacte de fission, bien que des simulations numériques récentes aient montrées le rôle probable de la constriction et de la dépolymérisation. Il a été démontré expérimentalement que, lors de l'hydrolyse du GTP, la dynamine tourne rapidement tout en se rétrécissant. La fréquence de rotation peut être de l'ordre de 10Hz, donnant un mécanisme pour la génération de flux de membrane dans la direction azimutale. Un autre moyen possible de générer de tels écoulements consiste à extraire un petit tube d'une vésicule unilamellaire géante (GUV) ou d'une cellule avec des pinces magnétiques appliquant une force sur une bille magnétique fixée à la membrane et à utiliser des oscillations de champ magnétique pour faire tourner la bille.

Nous analysons la stabilité d'un tube membranaire soumis à un taux de cisaillement Ω aux perturbations de la forme, de la vitesse de surface et de la tension de surface. En résolvant les équations hydrodynamiques à la surface, nous pouvons écrire une équation dynamique pour les perturbations du rayon en fonction des modes de Fourier. Cela montre qu'il existe une instabilité hélicoïdale entraînée par le cisaillement avec une longueur de pas définie par la taille du tube. Ceci est analogue à une instabilité similaire dans une tige élastique torsadée à chaque extrémité. Cependant, en raison de la nature fluide de la surface, la forme est modifiée par l'écoulement de l'état fondamental, ce qui entraîne l'ajout de spires supplémentaires à l'hélice à chaque tour. Cette advection stabilise finalement la croissance de l'hélice et conquit à un état stationnaire hors d'équilibre. Pour comprendre les implications de ce mécanisme d'amplification, nous résolvons la l'équation différentielle stochastique dans la forme afin de tenir compte des fluctuations thermiques Eq. 3.38. Ceci nous permet de calculer les fluctuations quadratiques moyennes de l'état stationnaire, Fig. 3.3. Nous estimons la vitesse de rotation nécessaire pour obtenir des déformations non-linéaires et discutons des implications possibles de ce mécanisme d'amplification de la fluctuation sur la scission du tube par la Dynamin, Fig. 3.4.

En résumé, nous avons développé une théorie hydrodynamique qui prédit une instabilité sur des tubes membranaires fluides qui est uniquement provoquée par un cisaillement constant de la membrane. On montre que de tels écoulements provoquent d'abord une instabilité hélicoïdale, ce qui est tout à fait distinct de toute instabilité précédemment identifiée des tubes membranaires fluides. Cette instabilité conduit à un état stationnaire associé à une augmentation significative du spectre de fluctuation d'un tube membranaire. Nous prédisons que cette instabilité est physiologiquement accessible à la Dynamin, bien que ce phénomène n'ait encore jamais associé à la fonction de la Dynamin. Cette instabilité constitue mécanisme qui pourrait conduire à la scission des tubes, par ex. suite à une augmentation de tension membranaire dans l'état hors d'équilibre, où à l'évolution non-linéaire de la forme d'un tube sous cisaillement.

D.4 Dynamiques passives et actives des tubes membranaires

Le but de ce travail est d'obtenir des équations générales d'évolution d'un tube membranaire soumis à une distribution de forces fluctuantes arbitraire due à des phénomènes actifs. En utilisant la formulation Onsager, nous dérivons des équations dynamiques pour la relaxation de la déformation d'un tube membranaire fluide permettant un contraste de viscosité entre l'intérieur et l'extérieur du tube, ainsi que des variations de tension superficielle dues aux écoulements de membrane. Pour obtenir les équations complètes du mouvement en utilisant la formulation de Onsager, nous devons d'abord écrire le Rayleighian. Le Rayleighian complet pour le système est obtenu à partir de la somme du taux de changement d'énergie libre pour le système, Eq. 4.6, et des dissipations d'énergie (la moitié du travail effectué sur le système), Eq. 4.7, et en ajoutant les contraintes sur le système en utilisant des multiplicateurs de Lagrange. Cette formulation équivaut à l'équation cinétique de Onsager avec des coefficients réciproques, mais est obtenu par formalisme variationnel, avec l'avantage que la recherche des couples de flux et de forces corrects est maintenant triviale puisqu'elle dérive directement du principe variationnel. Cette approche nous a permis d'obtenir les équations de mouvement couplées pour le système en prenant simplement en considération les fonctions de dissipation pertinentes et les contraintes du système et en tirant toutes les conséquences d'un principe variationnel.

En utilisant la transformée de Fourier et la solution connue aux équations de Stokes en 3D, nous pouvons trouver une équation de relaxation pour les perturbations de forme, équation 4.25. Nous considérons la dynamique de relaxation pour tous les modes, en examinant en particulier leur comportement asymptotique. Nous montrons que le mode $m = 0$ donne le même comportement de relaxation et l'instabilité de pearling que l'on trouve dans d'autres articles qui ne prennent en compte que les perturbations à symétrie axiale, Fig. 4.2a, 4.3. Nous analysons également le comportement de mise à l'échelle pour des valeurs plus élevées de m. Le mode $m = 1$ a un comportement intéressant dans la limite des grandes longueurs d'onde, où il se comporte comme une tige élastique, Fig. 4.2b. Les valeurs les plus élevées $m = 2, 3, 4...$ ont toutes un comportement de relaxation similaire, résumé à la Fig. 4.4.

Sur la base de ces tax de relaxation, nous examinons la dynamique des fluctuations thermiques passives et des fluctuations actives. Dans ce cas, “actif” fait référence aux fluctuations ne satisfaisant pas le théorème de fluctuation-dissipation. Nous calculons les fluctuations quadratiques moyennes pour les fluctuations passives et actives et calculons la “température effective” de chaque mode m en fonction de $\tilde{q}$, Fig. 4.7. Nous discutons de la façon dont la variation de la viscosité externe pourrait permettre de mesurer la contribution des fluctuations actives dans une expérience sur un tube extrait d'un GUV. Pour les travaux futurs, il serait intéressant d'examiner les effets de différentes formulations d'activités (à la fois dans les tubes et dans d'autres scénarios). Il serait également intéressant de considérer l'effet d'un fluide ambiant visco-élastique, car cela pourrait donner une meilleure approximation du cytoplasme dans les cellules. Cela donnerait non seulement une dynamique potentiellement plus riche, en raison de la présence d'une échelle de temps supplémentaire, mais pourrait également être utile pour comprendre des processus biologiques plus réalistes.

D.5 Discussion et perspectives

Les tubes membranaires lipidiques sont abondants à l'intérieur des cellules et leur dynamique a été impliquée dans de nombreux processus importants. Dans cette thèse, nous avons examiné quelques modèles théoriques de situations simples conçus pour imiter des processus importants en biologie, l'objectif étant de les utiliser pour élucider la physique sous-jacente. Dans ce chapitre, nous décrivons brièvement certaines orientations futures possibles de la recherche et des extensions du travail dans les trois chapitres principaux de la thèse.

Bibliography

S. Abounit and C. Zurzolo. Wiring through tunneling nanotubes - from electrical signals to organelle transfer. *Journal of Cell Science*, 125(5):1089–1098, 2012.

Bruce Alberts, Alexander Johnson, Julian Lewis, Martin Raff, Keith Roberts, and Peter Walter. *Molecular Biology of the Cell*. Garland Science, 4th edition, 2002.

Richard D. Allen. The contractile vacuole and its membrane dynamics. *BioEssays*, 22(11):1035–1042, 2000.

Richard D. Allen and Agnes K. Fok. Membrane Dynamics of the Contractile Vacuole Complex of Paramecium1. *The Journal of Protozoology*, 35(1):63–71, 1988.

Uri Alon. *An Introduction to Systems Biology*. CRC Press LLC, 2019.

M. I. Angelova, S. Soléau, Ph Méléard, F. Faucon, and P. Bothorel. Preparation of giant vesicles by external AC electric fields. Kinetics and applications. *Trends in Colloid and Interface Science VI*, pages 127–131, 1992.

Bruno Antonny, Christopher Burd, Pietro De Camilli, Elizabeth Chen, Oliver Daumke, Katja Faelber, Marijn Ford, Vadim A Frolov, Adam Frost, Jenny E Hinshaw, Tom Kirchhausen, Michael M Kozlov, Martin Lenz, Harry H Low, Harvey McMahon, Christien Merrifield, Thomas D Pollard, Phillip J Robinson, Aurélien Roux, and Sandra Schmid. Membrane fission by dynamin: what we know and what we need to know. *The EMBO Journal*, 35(21):2270–2284, 2016.

Marino Arroyo and Antonio DeSimone. Relaxation dynamics of fluid membranes. *Physical Review E*, 79(3), 2009.

A. Ashkin. Acceleration and Trapping of Particles by Radiation Pressure. *Physical Review Letters*, 24(4), 1970.

B. Audoly and Y. Pomeau. *Elasticity and Geometry: From Hair Curls to the Nonlinear Response of Shells*. OUP Oxford, 2010.

Fatemeh Bahmani, Joel Christenson, and Padmini Rangamani. Analysis of lipid flow on minimal surfaces. *Continuum Mechanics and Thermodynamics*, 28(1-2): 503–513, 2016.

Roy Bar-Ziv and Elisha Moses. Instability and "Pearling" States Produced in Tubular Membranes by Competition of Curvature and Tension. *Physical Review Letters*, 73(10):1392–1395, 1994.

Roy Bar-Ziv, Tsvi Tlusty, and Elisha Moses. Critical Dynamics in the Pearling Instability of Membranes. *Physical Review Letters*, 79(6):1158–1161, 1997.

C. Barbetta and J. B. Fournier. On the fluctuations of the force exerted by a lipid nanotubule. *The European Physical Journal E*, 29(2):183–189, 2009.

John W. Barrett, Harald Garcke, and Robert Nürnberg. A stable numerical method for the dynamics of fluidic membranes. *Numerische Mathematik*, 134(4):783–822, 2016.

Patricia Bassereau and Pierre Sens. *Physics of biological membranes*. Springer Berlin Heidelberg, New York, NY, 1st edition edition, 2018.

William Bialek. Perspectives on theory at the interface of physics and biology. *Reports on Progress in Physics*, 81(1), 2018.

D. Boal. *Mechanics of the Cell*. Cambridge University Press, 2002.

G. Boedec, M. Jaeger, and M. Leonetti. Pearling instability of a cylindrical vesicle. *Journal of Fluid Mechanics*, 743:262–279, 2014.

Kenneth A. Brakke. The Surface Evolver. *Experimental Mathematics*, 1(2):141–165, 1992.

F. Brochard and J. F. Lennon. Frequency spectrum of the flicker phenomenon in erythrocytes. *J. Phys. France*, 36:1035 – 1047, 1975.

F. Brochard-Wyart, N. Borghi, D. Cuvelier, and P. Nassoy. Hydrodynamic narrowing of tubes extruded from cells. *Proceedings of the National Academy of Sciences*, 103(20):7660–7663, 2006.

Weicheng Cai and T. C. Lubensky. Covariant hydrodynamics of fluid membranes. *Physical review letters*, 73(8):1186, 1994.

Weicheng Cai and T. C. Lubensky. Hydrodynamics and dynamic fluctuations of fluid membranes. *Physical Review E*, 52(4):4251, 1995.

P.B. Canham. The minimum energy of bending as a possible explanation of the biconcave shape of the human red blood cell. *Journal of Theoretical Biology*, 26 (1):61–81, 1970.

Morgan Chabanon, James C.S. Ho, Bo Liedberg, Atul N. Parikh, and Padmini Rangamani. Pulsatile Lipid Vesicles under Osmotic Stress. *Biophysical Journal*, 112(8):1682–1691, 2017.

Yee-Hung M. Chan and Wallace F. Marshall. How cells know the size of their organelles. *Science (New York, N.Y.)*, 337(6099):1186–1189, 2012.

Pao-Liu Chow. *Stochastic Partial Differential Equations.* Chapman and Hall/CRC, 2014.

F. H. C. Crick and A. F. W. Hughes. The physical properties of cytoplasm: A study by means of the magnetic particle method Part I. Experimental. *Experimental Cell Research*, 1(1):37–80, 1950.

Damien Cuvelier, Imre Derényi, Patricia Bassereau, and Pierre Nassoy. Coalescence of Membrane Tethers: Experiments, Theory, and Applications. *Biophysical Journal*, 88(4):2714–2726, 2005.

Srishti Dar, Sukrut C. Kamerkar, and Thomas J. Pucadyil. A high-throughput platform for real-time analysis of membrane fission reactions reveals dynamin function. *Nature Cell Biology*, 17(12):1588–1596, 2015.

Nicola De Franceschi, Maryam Alqabandi, Nolwenn Miguet, Christophe Caillat, Stephanie Mangenot, Winfried Weissenhorn, and Patricia Bassereau. The ESCRT protein CHMP2b acts as a diffusion barrier on reconstituted membrane necks. *Journal of Cell Science*, 132(4), 2019.

Imre Derényi, Frank Jülicher, and Jacques Prost. Formation and Interaction of Membrane Tubes. *Physical Review Letters*, 88(23), 2002.

Roberto Docampo, Veronica Jimenez, Noelia Lander, Zhu-Hong Li, and Sayantanee Niyogi. New Insights into Roles of Acidocalcisomes and Contractile Vacuole Complex in Osmoregulation in Protists. In *International Review of Cell and Molecular Biology*, volume 305, pages 69–113. Elsevier, 2013.

M. Doi and S.F. Edwards. *The theory of polymer dynamics.* International series of monographs on physics. Clarendon Press, 1986.

Masao Doi. Onsager's variational principle in soft matter. *Journal of Physics: Condensed Matter*, 23(28):284118, 2011.

Masao Doi. *Soft Matter Physics*. OUP Oxford, 2013.

Efi Efrati, Eran Sharon, and Raz Kupferman. The metric description of elasticity in residually stressed soft materials. *Soft Matter*, 9(34):8187, 2013.

Charles M. Elliott and Björn Stinner. Modeling and computation of two phase geometric biomembranes using surface finite elements. *Journal of Computational Physics*, 229(18):6585–6612, 2010.

E. Evans and A. Yeung. Hidden dynamics in rapid changes of bilayer shape. *Chemistry and Physics of Lipids*, 73(1-2):39–56, 1994.

E. A. Evans. New Membrane Concept Applied to the Analysis of Fluid Shear- and Micropipette-Deformed Red Blood Cells. *Biophysical Journal*, 13(9):941–954, 1973a.

E.A. Evans. A New Material Concept for the Red Cell Membrane. *Biophysical Journal*, 13(9):926–940, 1973b.

Joel H. Ferziger and Milovan Peric. *Computational Methods for Fluid Dynamics*. Springer-Verlag, Berlin Heidelberg, 3 edition, 2002.

Agnes K Fok, Marilynn S Aihara, Masaki Ishida, Kathleen V Nolta, Theodore L Steck, and Richard D Allen. The pegs on the decorated tubules of the contractile vacuole complex of Paramecium are proton pumps. *Journal of cell science*, 108 (Pt 1):3163–3170, 1995.

Piermarco Fonda, Melissa Rinaldin, Daniela J. Kraft, and Luca Giomi. Interface geometry of binary mixtures on curved substrates. *Physical Review E*, 98(3): 032801, 2018.

Jean-Baptiste Fournier. On the hydrodynamics of bilayer membranes. *International Journal of Non-Linear Mechanics*, 75:67–76, 2015.

Jean-Baptiste Fournier and Paolo Galatola. Critical Fluctuations of Tense Fluid Membrane Tubules. *Physical Review Letters*, 98(1), 2007.

Stephan Frank, Brigitte Gaume, Elke S. Bergmann-Leitner, Wolfgang W. Leitner, Everett G. Robert, Frédéric Catez, Carolyn L. Smith, and Richard J. Youle. The role of dynamin-related protein 1, a mediator of mitochondrial fission, in apoptosis. *Developmental Cell*, 1(4):515–525, 2001.

Theodore Frankel. *The Geometry of Physics: An Introduction.* Cambridge University Press, 3 edition, 2011.

P. Girard, J. Prost, and P. Bassereau. Passive or Active Fluctuations in Membranes Containing Proteins. *Physical Review Letters*, 94(8), 2005.

Nigel Goldenfeld and Carl Woese. Life is Physics: Evolution as a Collective Phenomenon Far From Equilibrium. *Annual Review of Condensed Matter Physics*, 2 (1):375–399, 2011.

Herbert Goldstein. *Classical Mechanics.* Pearson Education, 2002.

Raymond E Goldstein. Are theoretical results 'Results'? *eLife*, 7, 2018.

Raymond E. Goldstein, Thomas R. Powers, and Chris H. Wiggins. Viscous Nonlinear Dynamics of Twist and Writhe. *Physical Review Letters*, 80(23):5232–5235, 1998.

Raymond E. Goldstein, Alain Goriely, Greg Huber, and Charles W. Wolgemuth. Bistable Helices. *Physical Review Letters*, 84(7):1631–1634, 2000.

David Gonzalez-Rodriguez, Sébastien Sart, Avin Babataheri, David Tareste, Abdul I. Barakat, Christophe Clanet, and Julien Husson. Elastocapillary Instability in Mitochondrial Fission. *Physical Review Letters*, 115(8), 2015.

Alain Goriely. *The Mathematics and Mechanics of Biological Growth*, volume 45 of *Interdisciplinary Applied Mathematics.* Springer New York, New York, NY, 2017.

N. Gov. Membrane Undulations Driven by Force Fluctuations of Active Proteins. *Physical Review Letters*, 93(26), 2004.

N.S. Gov and S.A. Safran. Red Blood Cell Membrane Fluctuations and Shape Controlled by ATP-Induced Cytoskeletal Defects. *Biophysical Journal*, 88(3): 1859–1874, 2005.

Peter Gross, K. Vijay Kumar, and Stephan W. Grill. How Active Mechanics and Regulatory Biochemistry Combine to Form Patterns in Development. *Annual Review of Biophysics*, 46(1):337–356, 2017.

K. L. Gurin, V. V. Lebedev, and A. R. Muratov. Dynamic instability of a membrane tube. *Journal of experimental and theoretical physics*, 83:321–326, 1996.

Pierre A. Haas and Raymond E. Goldstein. Elasticity and glocality: initiation of embryonic inversion in *Volvox*. *Journal of The Royal Society Interface*, 12(112): 20150671, 2015.

John Happel and Howard Brenner. *Low Reynolds number hydrodynamics: with special applications to particulate media*. Number v. 1 in Mechanics of fluids and transport processes. M. Nijhoff ; Distributed by Kluwer Boston, The Hague ; Boston : Hingham, MA, USA, 1st pbk. ed edition, 1983.

Rebecca Heald and Orna Cohen-Fix. Morphology and Function of Membrane-bound Organelles. *Current opinion in cell biology*, 0:79–86, 2014.

W Helfrich. Elastic Properties of Lipid Bilayers: Theory and Possible Experiments. *Zeitschrift für Naturforschung C*, 28(11-12):693–703, 1973.

Mark L. Henle and Alex J. Levine. Hydrodynamics in curved membranes: The effect of geometry on particulate mobility. *Physical Review E*, 81(1), 2010.

John Heuser, Qianlong Zhu, and Margaret Clarke. Proton pumps populate the contractile vacuoles of Dictyostelium amoebae. *The Journal of Cell Biology*, 121 (6):1311–1327, 1993.

Stephanie Höhn, Aurelia R. Honerkamp-Smith, Pierre A. Haas, Philipp Khuc Trong, and Raymond E. Goldstein. Dynamics of a *Volvox* Embryo Turning Itself Inside Out. *Physical Review Letters*, 114(17), 2015.

Tristan T. Hormel, Sarah Q. Kurihara, M. Kathleen Brennan, Matthew C. Wozniak, and Raghuveer Parthasarathy. Measuring Lipid Membrane Viscosity Using Rotational and Translational Probe Diffusion. *Physical Review Letters*, 112(18), 2014.

Basarab G Hosu, Mingzhai Sun, Françoise Marga, Michel Grandbois, and Gabor Forgacs. Eukaryotic membrane tethers revisited using magnetic tweezers. *Physical Biology*, 4(2):67–78, 2007.

Rebecca B. Hoyle. *Pattern Formation: An Introduction to Methods*. Cambridge University Press, 2006.

Meyer B. Jackson. *Molecular and Cellular Biophysics*. Cambridge University Press, 2006.

U Jelerčič and N S Gov. Pearling instability of membrane tubes driven by curved proteins and actin polymerization. *Physical Biology*, 12(6):066022, 2015.

Frank Jülicher and Udo Seifert. Shape equations for axisymmetric vesicles: a clarification. *Physical Review E*, 49(5):4728, 1994.

Frank Jülicher and Jacques Prost. Cooperative Molecular Motors. *Physical Review Letters*, 75(13), 1995.

Marko Kaksonen and Aurélien Roux. Mechanisms of clathrin-mediated endocytosis. *Nature Reviews Molecular Cell Biology*, 19(5):313–326, 2018.

Kinneret Keren, Zachary Pincus, Greg M. Allen, Erin L. Barnhart, Gerard Marriott, Alex Mogilner, and Julie A. Theriot. Mechanism of shape determination in motile cells. *Nature*, 453(7194):475–480, 2008.

K. Komsic-Buchmann, L. Wostehoff, and B. Becker. The Contractile Vacuole as a Key Regulator of Cellular Water Flow in Chlamydomonas reinhardtii. *Eukaryotic Cell*, 13(11):1421–1430, 2014.

Shigeyuki Komura and Reinhard Lipowsky. Fluctuations and stability of polymerized vesicles. *Journal de Physique II*, 2(8):1563–1575, 1992.

Shigeyuki Komura, Kento Yasuda, and Ryuichi Okamoto. Dynamics of two-component membranes surrounded by viscoelastic media. *Journal of Physics: Condensed Matter*, 27(43):432001, 2015.

Gerbrand Koster, Martijn VanDuijn, Bas Hofs, and Marileen Dogterom. Membrane tube formation from giant vesicles by dynamic association of motor proteins. *Proceedings of the National Academy of Sciences*, 100(26):15583–15588, 2003.

R Koynova and B Tenchov. Transitions between lamellar and nonlamellar phases in membrane lipids and their physiological roles. *OA Biochemistry*, 1(1), 2013.

Michael M. Kozlov. Dynamin: possible mechanism of "Pinchase" action. *Biophysical journal*, 77(1):604–616, 1999.

Michael M. Kozlov. Fission of Biological Membranes: Interplay Between Dynamin and Lipids. *Traffic*, 2(1):51–65, 2001.

Marieke Kranenburg and Berend Smit. Phase Behavior of Model Lipid Bilayers †. *The Journal of Physical Chemistry B*, 109(14):6553–6563, 2005.

K. Kruse, J. F. Joanny, F. Jülicher, J. Prost, and K. Sekimoto. Generic theory of active polar gels: a paradigm for cytoskeletal dynamics. *The European Physical Journal E*, 16(1):5–16, 2005.

Akihiro Kusumi, Chieko Nakada, Ken Ritchie, Kotono Murase, Kenichi Suzuki, Hideji Murakoshi, Rinshi S. Kasai, Junko Kondo, and Takahiro Fujiwara. Paradigm Shift of the Plasma Membrane Concept from the Two-Dimensional Continuum Fluid to the Partitioned Fluid: High-Speed Single-Molecule Tracking of Membrane Molecules. *Annual Review of Biophysics and Biomolecular Structure*, 34(1):351–378, 2005.

L. D. Landau and E. M. Lifshitz. *Statistical Physics.* Elsevier, 1951.

L. D. Landau and E. M. Lifshitz. *Fluid Mechanics.* Elsevier, 1959.

L.D. Landau, E.M. Lifshitz, A.M. Kosevich, J.B. Sykes, L.P. Pitaevskii, and W.H. Reid. *Theory of Elasticity.* Course of theoretical physics. Elsevier Science, 1986.

Thomas Lecuit and L. Mahadevan. Morphogenesis one century after *On Growth and Form*. *Development*, 144(23):4197–4198, 2017.

John M. Lee. *Riemannian manifolds: an introduction to curvature.* Number 176 in Graduate texts in mathematics. Springer, New York, 1997.

Stanislas Leibler and David Andelman. Ordered and curved meso-structures in membranes and amphiphilic films. *Journal de Physique*, 48(11), 1987.

Martin Lenz, Jacques Prost, and Jean-François Joanny. Mechanochemical action of the dynamin protein. *Physical Review E*, 78(1), 2008.

Reinhard Lipowsky and Erich Sackmann. *Structure and Dynamics of Membranes.* Elsevier Science, 1995.

J.-B. Manneville, P. Bassereau, S. Ramaswamy, and J. Prost. Active membrane fluctuations studied by micropipet aspiration. *Physical Review E*, 64(2), 2001.

Davide Marenduzzo, Cristian Micheletti, and Peter R. Cook. Entropy-Driven Genome Organization. *Biophysical Journal*, 90(10), 2006.

Fernando C. Marques and André Neves. The Willmore Conjecture. *Jahresbericht der Deutschen Mathematiker-Vereinigung*, 116(4):201–222, 2014.

J.E. Marsden and T.J.R. Hughes. *Mathematical Foundations of Elasticity.* Dover Civil and Mechanical Engineering Series. Dover, 1994.

L Mathivet, S Cribier, and P F Devaux. Shape change and physical properties of giant phospholipid vesicles prepared in the presence of an AC electric field. *Biophysical Journal*, 70(3):1112–1121, 1996.

Sonya J. McClure and Phillip J. Robinson. Dynamin, endocytosis and intracellular signalling. *Molecular Membrane Biology*, 13(4):189–215, 1996.

Zachary A. McDargh and Markus Deserno. Dynamin's helical geometry does not destabilize membranes during fission. *Traffic*, 19(5):328–335, 2018.

Zachary A. McDargh, Pablo Vázquez-Montejo, Jemal Guven, and Markus Deserno. Constriction by dynamin: Elasticity versus adhesion. *Biophysical Journal*, 111 (11):2470–2480, 2016.

Omar Mertins, Nádya P. da Silveira, Adriana R. Pohlmann, André P. Schröder, and Carlos M. Marques. Electroformation of Giant Vesicles from an Inverse Phase Precursor. *Biophysical Journal*, 96(7):2719–2726, 2009.

R. Milo and R. Phillips. *Cell Biology by the Numbers.* CRC Press, 2015.

Alexander A. Mironov and Margit Pavelka. *The Golgi Apparatus: State of the art 110 years after Camillo Golgi's discovery.* Springer, 2009.

Mohammad R. K. Mofrad and Roger D. Kamm. *Cytoskeletal Mechanics: Models and Measurements in Cell Mechanics.* Cambridge University Press, 2006.

M. Monticelli, D. V. Conca, E. Albisetti, A. Torti, P. P. Sharma, G. Kidiyoor, S. Barozzi, D. Parazzoli, P. Ciarletta, M. Lupi, D. Petti, and R. Bertacco. Magnetic domain wall tweezers: a new tool for mechanobiology studies on individual target cells. *Lab on a Chip*, 16(15):2882–2890, 2016.

Sandrine Morlot, Martin Lenz, Jacques Prost, Jean-François Joanny, and Aurélien Roux. Deformation of dynamin helices damped by membrane friction. *Biophysical Journal*, 99(11):3580–3588, 2010.

Sandrine Morlot, Valentina Galli, Marius Klein, Nicolas Chiaruttini, John Manzi, Frédéric Humbert, Luis Dinis, Martin Lenz, Giovanni Cappello, and Aurélien Roux. Membrane shape at the edge of the dynamin helix sets location and duration of the fission reaction. *Cell*, 151(3):619–629, 2012.

Richard G. Morris. Signatures of Mechanosensitive Gating. *Biophysical Journal*, 112(1), 2017.

Richard G. Morris and Madan Rao. Covariant Active Hydrodynamics of Shape-Changing Epithelial Monolayers. *arXiv:1710.09110 [cond-mat, physics:physics]*, 2017.

Richard G. Morris and Matthew S. Turner. Mobility Measurements Probe Conformational Changes in Membrane Proteins due to Tension. *Physical Review Letters*, 115(19), 2015.

Derek E. Moulton and Alain Goriely. Surface growth kinematics via local curve evolution. *Journal of Mathematical Biology*, 68(1-2):81–108, 2014.

Chris Mullins. *The Biogenesis of Cellular Organelles*. Molecular Biology Intelligence Unit. Springer US, 2005.

J. D. Murray. *Asymptotic Analysis*. Springer New York, 1992.

Yutaka Naitoh, Takashi Tominaga, Masaki Ishida, A. Fok, M. Aihara, and Richard D. Allen. How does the contractile vacuole of Paramecium multimicronucleatum expel fluid? Modelling the expulsion mechanism. *Journal of experimental biology*, 200(4):713–721, 1997.

P. Nassoy, D. Cuvelier, R. Bruinsma, and F. Brochard-Wyart. Nanofluidics in cellular tubes under oscillatory extension. *EPL (Europhysics Letters)*, 84(1):18004, 2008.

David Nelson, Tsvi Piran, and Steven Weinberg. *Statistical Mechanics Of Membranes And Surfaces: 2nd Edition*. World Scientific, 2004.

Philip Nelson, Thomas Powers, and Udo Seifert. Dynamical Theory of the Pearling Instability in Cylindrical Vesicles. *Physical Review Letters*, 74(17):3384–3387, 1995.

Tsuyoshi Nishi and Michael Forgac. The vacuolar h+-atpases — nature's most versatile proton pumps. *Nature Reviews Molecular Cell Biology*, 3(2):94–103, 2002.

J. Nixon-Abell, C. J. Obara, A. V. Weigel, D. Li, W. R. Legant, C. S. Xu, H. A. Pasolli, K. Harvey, H. F. Hess, E. Betzig, C. Blackstone, and J. Lippincott-Schwartz. Increased spatiotemporal resolution reveals highly dynamic dense tubular matrices in the peripheral ER. *Science*, 354(6311), 2016.

G.M. Odell, G. Oster, P. Alberch, and B. Burnside. The mechanical basis of morphogenesis. *Developmental Biology*, 85(2):446–462, 1981.

K. Olbrich, W. Rawicz, D. Needham, and E. Evans. Water permeability and mechanical strength of polyunsaturated lipid bilayers. *Biophysical Journal*, 79(1):321–327, 2000.

Lars Onsager. Reciprocal relations in irreversible processes. I. *Physical review*, 37 (4):405, 1931a.

Lars Onsager. Reciprocal relations in irreversible processes. II. *Physical review*, 38 (12):2265, 1931b.

Martina Pannuzzo, Zachary A McDargh, and Markus Deserno. The role of scaffold reshaping and disassembly in dynamin driven membrane fission. *eLife*, 7, 2018.

D. J. Patterson. Contractile vacuoles and associated structures: their organization and function. *Biological Reviews*, 55(1):1–46, 1980.

C.S. Peskin, G.M. Odell, and G.F. Oster. Cellular motions and thermal fluctuations: the Brownian ratchet. *Biophysical Journal*, 65(1), 1993.

Mariela D. Petkova, Gašper Tkačik, William Bialek, Eric F. Wieschaus, and Thomas Gregor. Optimal Decoding of Cellular Identities in a Genetic Network. *Cell*, 176 (4):844–855, 2019.

Rob Phillips, Jane Kondev, Julie Theriot, Nigel Orme, and Hernan G Garcia. *Physical biology of the cell*. Garland Science, 2010.

Thomas R. Powers. Dynamics of filaments and membranes in a viscous fluid. *Reviews of Modern Physics*, 82(2):1607–1631, 2010.

Thomas R. Powers and Raymond E. Goldstein. Pearling and Pinching: Propagation of Rayleigh Instabilities. *Physical Review Letters*, 78(13):2555–2558, 1997.

Thomas R. Powers, Greg Huber, and Raymond E. Goldstein. Fluid-membrane tethers: Minimal surfaces and elastic boundary layers. *Physical Review E*, 65(4), 2002.

J. Prost and R. Bruinsma. Shape fluctuations of active membranes. *EPL (Europhysics Letters)*, 33(4):321, 1996.

J. Prost, F. Jülicher, and J-F. Joanny. Active gel physics. *Nature Physics*, 11(2): 111–117, 2015.

Pramod A. Pullarkat, Paul Dommersnes, Pablo Fernández, Jean-François Joanny, and Albrecht Ott. Osmotically Driven Shape Transformations in Axons. *Physical Review Letters*, 96(4), 2006.

E M Purcell. Life at low Reynolds number. *American Journal of Physics*, 45(3):10, 1977.

F. Quemeneur, J. K. Sigurdsson, M. Renner, P. J. Atzberger, P. Bassereau, and D. Lacoste. Shape matters in protein mobility within membranes. *Proceedings of the National Academy of Sciences*, 111(14):5083–5087, 2014.

Mohammad Rahimi and Marino Arroyo. Shape dynamics, lipid hydrodynamics, and the complex viscoelasticity of bilayer membranes. *Physical Review E*, 86(1), 2012.

Mohammad Rahimi, Antonio DeSimone, and Marino Arroyo. Curved fluid membranes behave laterally as effective viscoelastic media. *Soft Matter*, 9(46):11033, 2013.

Sriram Ramaswamy, John Toner, and Jacques Prost. Nonequilibrium fluctuations, traveling waves, and instabilities in active membranes. *Physical review letters*, 84 (15):3494, 2000.

S. Alex Rautu. Curvature instability of membranes near rigid inclusions. *Physical Review E*, 97(2), 2018.

Lord Rayleigh. On the instability of a cylinder of viscous liquid under capillary force. *Philosophical Magazine Series 5*, 34(207):145–154, 1892.

Ralf P. Richter, Rémi Bérat, and Alain R. Brisson. Formation of Solid-Supported Lipid Bilayers: An Integrated View. *Langmuir*, 22(8):3497–3505, 2006.

A. Roux, G. Koster, M. Lenz, B. Sorre, J.-B. Manneville, P. Nassoy, and P. Bassereau. Membrane curvature controls dynamin polymerization. *Proceedings of the National Academy of Sciences*, 107(9):4141–4146, 2010.

Aurélien Roux. Reaching a consensus on the mechanism of dynamin? *F1000Prime Reports*, 6, 2014.

Aurélien Roux, Katherine Uyhazi, Adam Frost, and Pietro De Camilli. Gtp-dependent twisting of dynamin implicates constriction and tension in membrane fission. *Nature*, 441(7092):528–531, 2006.

T. V. Sachin Krishnan, Ryuichi Okamoto, and Shigeyuki Komura. Relaxation dynamics of a compressible bilayer vesicle containing highly viscous fluid. *Physical Review E*, 94(6), 2016.

T V Sachin Krishnan, Kento Yasuda, Ryuichi Okamoto, and Shigeyuki Komura. Thermal and active fluctuations of a compressible bilayer vesicle. *Journal of Physics: Condensed Matter*, 30(17):175101, 2018.

E. Sackmann and Toni Feder. Budding, fission and domain formation in mixed lipid vesicles induced by lateral phase separation and macromolecular condensation. *Molecular Membrane Biology*, 12(1):21–28, 1995.

P. G. Saffman. Brownian motion in thin sheets of viscous fluid. *Journal of Fluid Mechanics*, 73(04):593, 1976.

P. G. Saffman and M. Delbruck. Brownian motion in biological membranes. *Proceedings of the National Academy of Sciences*, 72(8):3111–3113, 1975.

Samuel A. Safran. *Statistical Thermodynamics of Surfaces, Interfaces, and Membranes.* Addison-Wesley Pub., 1994.

Guillaume Salbreux and Frank Jülicher. Mechanics of active surfaces. *Physical Review E*, 96(3), 2017.

Sumithra Sankararaman, Gautam I. Menon, and P. B. Sunil Kumar. Two-component fluid membranes near repulsive walls: Linearized hydrodynamics of equilibrium and nonequilibrium states. *Physical Review E*, 66(3), 2002.

S. Särkkä and A. Solin. *Applied Stochastic Differential Equations.* Institute of Mathematical Statistics Textbooks. Cambridge University Press, 2019.

Udo Seifert. Configurations of fluid membranes and vesicles. *Advances in Physics*, 46(1):13–137, 1997.

Udo Seifert and Stephen A. Langer. Hydrodynamics of membranes: the bilayer aspect and adhesion. *Biophysical Chemistry*, 49(1):13–22, 1994.

Pierre Sens. Dynamics of Nonequilibrium Membrane Bud Formation. *Physical Review Letters*, 93(10), 2004.

Zheng Shi, Zachary T. Graber, Tobias Baumgart, Howard A. Stone, and Adam E. Cohen. Cell Membranes Resist Flow. *Cell*, 175(7), 2018.

Yoko Shibata, Junjie Hu, Michael M. Kozlov, and Tom A. Rapoport. Mechanisms Shaping the Membranes of Cellular Organelles. *Annual Review of Cell and Developmental Biology*, 25(1):329–354, 2009.

R Shlomovitz, N S Gov, and A Roux. Membrane-mediated interactions and the dynamics of dynamin oligomers on membrane tubes. *New Journal of Physics*, 13 (6):065008, 2011.

James Simons. Minimal Varieties in Riemannian Manifolds. *Annals of Mathematics*, 88(1):62–105, 1968.

Kai Simons and Winchil L.C. Vaz. Model Systems, Lipid Rafts, and Cell Membranes. *Annual Review of Biophysics and Biomolecular Structure*, 33(1):269–295, 2004.

Mijo Simunovic, Jean-Baptiste Manneville, Henri-François Renard, Emma Evergren, Krishnan Raghunathan, Dhiraj Bhatia, Anne K. Kenworthy, Gregory A. Voth, Jacques Prost, Harvey T. McMahon, Ludger Johannes, Patricia Bassereau, and Andrew Callan-Jones. Friction Mediates Scission of Tubular Membranes Scaffolded by BAR Proteins. *Cell*, 170(1):172–184, 2017.

S. J. Singer and G. L. Nicolson. The Fluid Mosaic Model of the Structure of Cell Membranes. *Science*, 175(4023):720–731, 1972.

Christian Stock, Heidi K. Grønlien, Richard D. Allen, and Yutaka Naitoh. Osmoregulation in Paramecium: in situ ion gradients permit water to cascade through the cytosol to the contractile vacuole. *J Cell Sci*, 115(11):2339–2348, 2002.

T. Tani, R.D. Allen, and Y. Naitoh. Periodic tension development in the membrane of the in vitro contractile vacuole of Paramecium multimicronucleatum: modification by bisection, fusion and suction. *The Journal of Experimental Biology*, 203 (2):239–251, 2000.

D.A.W. Thompson. *On Growth and Form.* Cambridge University Press, 1917.

T. Tlusty and S. A. Safran. Microemulsion networks: the onset of bicontinuity. *Journal of Physics: Condensed Matter*, 12(8A):A253, 2000.

T. Tlusty, S. A. Safran, and R. Strey. Topology, phase instabilities, and wetting of microemulsion networks. *Physical review letters*, 84(6):1244, 2000.

Takashi Tominaga, Richard D. Allen, and Yutaka Naitoh. Electrophysiology of the in situ contractile vacuole complex of Paramecium reveals its membrane dynamics and electrogenic site during osmoregulatory activity. *Journal of Experimental Biology*, 201(3):451–460, 1998.

S_ Tomotika. On the instability of a cylindrical thread of a viscous liquid surrounded by another viscous fluid. *Proceedings of the Royal Society of London. Series A - Mathematical and Physical Sciences*, 150(870):322–337, 1935.

Alejandro Torres-Sánchez, Daniel Millán, and Marino Arroyo. Modelling fluid deformable surfaces with an emphasis on biological interfaces. *Journal of Fluid Mechanics*, 872:218–271, 2019.

Alan M. Turing. The Chemical Basis of Morphogenesis. *Philosophical Transactions of the Royal Society of London. Series B, Biological Sciences*, 237(641), 1952.

H. Turlier, D. A. Fedosov, B. Audoly, T. Auth, N. S. Gov, C. Sykes, J.-F. Joanny, G. Gompper, and T. Betz. Equilibrium physics breakdown reveals the active nature of red blood cell flickering. *Nature Physics*, 12(5):513–519, 2016.

F. Valentino, P. Sens, J. Lemière, A. Allard, T. Betz, C. Campillo, and C. Sykes. Fluctuations of a membrane nanotube revealed by high-resolution force measurements. *Soft Matter*, 12(47):9429–9435, 2016.

T. J. Willmore. Note on embedded surfaces. *An. Şti. Univ. "Al. I. Cuza" Iaşi Secţ. I a Mat.*, 11B:493–496, 1965.

T.J. Willmore. *An Introduction to Differential Geometry.* Dover Books on Mathematics Series. Dover Publications, 2012.

Jean Wolff, Shigeyuki Komura, and David Andelman. Budding transition of asymmetric two-component lipid domains. *Physical Review E*, 94(3), 2016.

Felix Wong, Lars D. Renner, Gizem Özbaykal, Jayson Paulose, Douglas B. Weibel, Sven van Teeffelen, and Ariel Amir. Mechanical strain sensing implicated in cell shape recovery in Escherichia coli. *Nature Microbiology*, 2, 2017.

Ding Xu and Jeffrey D Esko. A Golgi-on-a-chip for glycan synthesis. *Nature Chemical Biology*, 5(9):612–613, 2009.

Ayako Yamada, Alexandre Mamane, Jonathan Lee-Tin-Wah, Aurélie Di Cicco, Coline Prévost, Daniel Lévy, Jean-François Joanny, Evelyne Coudrier, and Patricia Bassereau. Catch-bond behaviour facilitates membrane tubulation by non-processive myosin 1b. *Nature Communications*, 5, 2014.

Ou-Yang Zhong-Can and Wolfgang Helfrich. Bending energy of vesicle membranes: General expressions for the first, second, and third variation of the shape energy and applications to spheres and cylinders. *Physical Review A*, 39(10):5280, 1989.

Joshua Zimmerberg and Michael M. Kozlov. How proteins produce cellular membrane curvature. *Nature Reviews Molecular Cell Biology*, 7(1):9–19, 2006.